UNIVERSITY OF CALIFORNIA, SAN DIEGO

The shape of things to come: examining the interplay of elasticity, activity and geometry in soft matter

A dissertation submitted in partial satisfaction of the
requirements for the degree
Doctor of Philosophy

in

Physics

by

Arthur A. Evans

Committee in charge:

Professor Eric Lauga, Chair
Professor Alexander Groisman, Co-Chair
Professor Michael Anderson
Professor Michael Berns
Professor Patrick Diamond
Professor Daniel Tartakovsky

2011

The dissertation of Arthur A. Evans is approved, and it is acceptable in quality and form for publication on microfilm and electronically:

_____

_____

_____

_____

_____
Co-Chair

_____
Chair

University of California, San Diego

2011

DEDICATION

To Heather, for reminding me why original thought is so important.

EPIGRAPH

Any sufficiently advanced form of science is indistinguishable from magic.

—Arthur C. Clarke's third law

Life is like polymer dynamics: there's only one way to be straight, but a lot of ways to be kinky.

—Anon.

TABLE OF CONTENTS

LIST OF FIGURES

ACKNOWLEDGEMENTS

I would like to extend my thanks to my advisor Eric Lauga for demonstrating that one can be a successful scientist without sacrificing a compassion for learning; without him my ambition and soul may have been lost forever to the depths of quantitative finance.

Thanks also to those that participated in many unwise microwave oven experiments, and the other tangential physics with which we occupied ourselves when avoiding research obligations.

Thanks to Takuji Ishikawa, Saverio Spagnolie, and Takami Yamaguchi for co-authorship on published material found herein.

Chapters 2 and 3, in full, is a reprint of the material as it appears in Physical Review E: AA Evans and E Lauga 2009, *Phys. Rev. E* **79**, 066116, 2009 and A. A. Evans and E. Lauga, *Phys. Rev. E*, **82**, 041945, 2010. The dissertation author was the primary author on both of these publications.

Chapter 4, in part, is a reprint of the material as it appears in Soft Matter: AA Evans, SE Spagnolie and E Lauga, *Soft Matter*, **6**, 1737-1747, 2010, as well as material being prepared for publication. The dissertation author was primary author on this publication.

Chapter 5, in part, is material in preparation for publication. The dissertation author was primary author on this material.

VITA

2006	B. S. in Physics *magna cum laude*, California Polytechnic State University, San Luis Obispo
2006-2011	Graduate Teaching Assistant, University of California, San Diego
2011	Ph. D. in Physics, University of California, San Diego

PUBLICATIONS

A. A. Evans and E. Lauga, *Adhesion transition of flexible sheets*, Phys. Rev. E, **79**, 066116, 2009.

A. A. Evans, S. Spagnolie and E. Lauga, *Stokesian Jellyfish: Locomotion of a Bilayer Vesicle*, Soft Matter, 2010, **6**, 1737

A. A. Evans and E. Lauga, *Propulsion of passive filaments and active flagella near boundaries*, Phys. Rev. E, **82**, 041915, 2010

A A. Evans and E. Lauga, *Active pumping by an elastic membrane*, in preparation

A. A. Evans, E. Lauga, T. Ishikawa and T. Yamaguchi, *Global order and instabilities in concentrated suspensions of spherical microorganisms*, in preparation

ABSTRACT OF THE DISSERTATION

The shape of things to come: examining the interplay of elasticity, activity and geometry in soft matter

by

Arthur A. Evans

Doctor of Philosophy in Physics

University of California, San Diego, 2011

Professor Eric Lauga, Chair
Professor Alexander Groisman, Co-Chair

This dissertation contains within an exploration of the interactions between various soft matter systems and an environmental stimulus. The natural case studies for examining soft matter using the language of thermodynamics and phase transitions are biological constituents, from slender filaments to entire collections of organisms. We first present a brief overview of soft condensed matter, couching the thesis in terms of states of matter and preparing the stage for using continuum mechanics to examine the sensitive balance between competing physical forces in determining the final state of the systems of interest. Following this we present analysis of long-range interactions in a ubiquitous soft matter system, flexible fila-

ments. Adhesion events that occur between attractive filaments can be understood in terms of phase transitions, and herein we present a methodology for describing physical regimes where such transitions take place. Following this we present analyses of slender filaments and flexible membranes interacting with viscous fluids; of primary concern is the transduction of undulatory motion of the surface into propulsive thrust, as a model of microorganism locomotion. We show that slender filaments near walls can be shown to exhibit non-intuitive force characteristics as a fundamental consequence of the flexibility and geometry of the system, for several models of passively actuated and internally active model flagella. We then present two different active models for propulsion using a flexible membrane: the first simplifies the geometry in order to elucidate the direct consequences of internal forcing on macroscopic propulsive thrust, while the second is a proof of principle model for a microscopic vesicular swimmer. Finally, we study collective locomotion of microorganisms and active colloidal dispersions by performing a robust hydrodynamics simulation of a concentrated suspension of microswimmers. We find that global polar order persists throughout the system as a function of various microscopic swimming/activity parameters, as well as the volume fraction.

Chapter 1

Introduction to active soft matter

As children, many of us are taught about the three classical phases of matter: liquid, solid and gas. Zealous pedagogues may even go so far as to introduce the exotic "fourth state" known as plasma. These are, perhaps, the most common states of matter found on our planet, but there actually exists a host of more esoteric forms that are not as easily classified. Complex fluids under external stress may behave more like solids, like the mixture of cornstarch and water known affectionately as "oobleck"; other complex fluids like toothpaste or mayonnaise behave in the opposite fashion, flowing more easily when under an applied force than without. There are even more complex materials that eschew simple demarcation of any sort, and it is this last type that is the focus of this dissertation.

The following work provides an examination of different types of "soft matter", with a particular emphasis on activity and interactions in the material. By couching the study of soft materials in the language of phase transitions and statistical mechanics, we can explore how biological constituents, whole organisms, and even collections of swimming cells all behave as novel active materials.

1.1 Sticky hairs, geckos and MEMS

Wet hair clumping together after bathing is perhaps one of the most common examples of a phenomenon known as elasto-capillary coalescence; the competition between surface tension and elastic forces determines a critical length at which a relatively straight elastic hair bends into an adhered state, leading to clumping [1, 2, 3]. At the microscopic scale, elasto-capillary interactions become a burden for those engaged in precise fabrication of devices that involve thin filaments. Microelectromechanical structures (MEMS) depends on identifying this competition between forces that leads to different types of phase behavior [4, 5]. Unlike in traditional materials, the phases here are not solid, liquid or gas, but rather "stuck" or "unstuck".

Not all sticky hairs require elasto-capillary interactions, however: geckos have a multitude of microscopic fibers lining their feet which act on surfaces via Van der Waals forces, leading to an adhesive strength that does not depend on fluid-

structure interactions [6, 7]. By studying "dry" adhesion, similar statements can be made about phase transitions between different material states, either stuck or unstuck. In viewing arrays of fibers in this fashion we gain insight into the greater workings of this particular class of soft matter system.

1.2 Elasticity and fluid dynamics

Microorganisms present a stark contrast with the relatively static organization of sticky hairs and gecko feet, while still providing a natural framework in which we can study interacting soft matter; engaged in a frenetic dance of reproduction and consumption, swimming microbes and their fluid-structure interactions highlight the shades of nuance that develop in the presence of active hydrodynamics [8, 9].

In order to generate propulsive thrust, microorganisms must generate internal forces to actuate their swimming appendages, and then use viscous dissipation to propel themselves through the fluid environment. This task is by no means simple, nor intuitive; the sensitive balance between an organism's activity, elasticity, and geometry combine to yield the startling efficacy with which these swimmers can traverse their hostile surroundings.

While studying single organism locomotion is an exercise in material properties and fluid interaction, collections of swimming microbes can be considered a material in and of itself. The perpetual interactions between these motile cells can generate patterns of whirls and whorls that are generally considered to be only the purview of turbulent hydrodynamics; the assembly of organisms can be considered a living fluid, and to understand the behavior of the whole we can use the theoretical techniques and insights provided by nonequilibrium statistical mechanics and active hydrodynamics.

1.3 Collective locomotion

Under a microscope, the living world teems with swimming cells each striving individually to feed, reproduce, and evade inevitable doom. Even amongst these unthinking micro-organisms, however, cooperation and connectivity ties the future of the individuals to the population as a whole. Lacking even the vestiges of a brain, these micro-swimmers can communicate, at best, through secretion of reactive chemicals, but even in the absence of such substances, these entities interact in complicated patterns and exhibit surprising behavior. Without a central nervous system or chemical signaling to guide the swimming cells, spontaneous self-organization is possible only through the medium that the entire population shares: the fluid that they are immersed in every moment of their small lives. Disturbances in the fluid, created by nearby boundaries or other cells, propagate long distances, thus connecting entire populations of swimmers in a web of interactions.

This connectivity is a source of great complexity, and in understanding the physical mechanism by which patterns form in space and time, we can more fully understand how collective behavior and multi-cellularity develop in biology.

Every disturbance in a fluid environment dominated by viscosity has long-range effects, and this is the primary difficulty encountered when studying the hydrodynamics of the microbial world. Each swimmer in a population is an active cell that sets up a flow field, influencing its neighbors just as it is, in turn, affected by them. These complex interactions can lead to aggregation amongst cells, orientational diffusion, and interactions with solid boundaries that create collective motion out of many individual swimmers [10]. Although some micro-organisms communicate crudely via chemical signaling, these instances of cooperativity and collective interaction are emergent phenomena based solely on hydrodynamic interactions.

Locomotion on the level of the individual cell can be achieved by a number of different means, but one of the most common methods is via flagella or cilia. These whiplike appendages oscillate due to microscopic motors powering the filament of an organism, beating back and forth to drive the cell through the viscous fluid. Some organisms have an array of these devices patterned on their surface, called

cilia, which coordinate their motion in order to propel the swimmer; lacking any kind of central nervous system or chemical signaling, this synchronization can be achieved by hydrodynamic interactions alone, and without the long-range coupling of the fluid, this would not be possible.

In addition to the already intractable many-body problem offered by the governing fluid mechanics, each individual cell is a machine, burning energy to swim through the viscous fluid that interacts so strongly with it's neighbors. Because of the highly coupled nature of the fluid, and the activity of the individual constituents, complicated patterns can be formed.

Classical studies of many-particle systems have been restricted to simplified cases like ideal gases or slight perturbations from an idealized state. Biological systems, due to their complexity and fundamentally active nature, have stymied attempts to perform similar analyses. Although some efforts have been devoted to studying the inherently non-equilibrium nature of collective locomotion [11], and inroads have been made in studying pattern formation in active systems [12, 13], there is no general theory for non-equilibrium statistical mechanics of dissipative systems.

Much of the success of modern physics relies on the ability to calculate macroscopic quantities from microscopic variables, and *vice versa*. The celebrated fluctuation-dissipation theorem gives the fundamental relationship between macroscopic diffusion and microscopic thermal noise of a system in equilibrium. Alas, for the chemically driven microscopic cells that show such rich behavior, the governing physics are certainly far from thermal equilibrium. So far, despite the best efforts of many determined thermodynamicists, a general theory eludes the scientific community. Biological physics has proven indispensable in providing a ubiquitous testing ground for non-equilibrium theories and experiments.

The emergent collective swimming modes displayed by bacterial populations and dense spermatozoa suspensions are an example of the unexpected order that arises from interactions with the fluid medium. In the inertialess environment endemic to microbial fluid dynamics, phenomena such as turbulence cannot exist in the usual sense. However, large scale order and mixing in swimming suspensions

of micro-organisms has been observed to occur in a manner that is reminiscent of turbulence. This collective behavior seems to defy intuition, but stationary patterns and time-independent order has been observed in active systems ranging from optical systems to biological suspensions. Pattern formation in driven systems is by no means a new topic, and the mathematics that governs dynamical systems has been explored extensively [14]. The physics of these phenomena, however, remains mysterious.

1.4 Outline

The organization of this dissertation generally follows a path from the relatively simple problem of dry adhesion between filaments towards increasingly complex issues, incorporating the effects of confining geometries and progressively difficult interactions amongst material constiuents. Chapter 2 describes the morphological states between interacting filaments or sheets, and couches the transition between adhered and unadhered shapes in the language of phase transitions. Chapter 3 provides an introduction to active elastohydrodynamics, emphasizing the importance of describing the balance between elasticity, activity and confinement effects in flagellate propulsion. Following the completion of this study on filaments, propulsion due to membranes is discussed in Chapter 4, and the fundamental difficulties associated with the deformation of surfaces are incorporated into the framework of active fluidics. Again, the transduction of microscopic interactions are couched in terms of phase transitions to provide the foundation to discuss propulsion in relation to a thermodynamic engine. Finally, collective motion of swimming microbes is studied in Chapter 5, and comparisons with existing models for active soft matter are made.

Chapter 2

Adhesion in flexible filaments

2.1 Introduction

As fabrication technology and nanoscale engineering increase in complexity, it becomes vital to understand small-scale interactions between material components. Surface-tension mediated forces play a large role in self-assembly, not only at the macro-scale [2], but also for micro-electromechanical and nano-electromechanical structures (MEMS and NEMS), and as such, a large amount of work has been done in studying the adhesive forces involved [4, 15, 1]. Carbon nanotubes (CNTs) have attracted significant attention since they were discovered to exhibit novel electrical and mechanical properties, and it has been found that CNTs can adhere to each other under the influence of capillary forces [5, 16, 17]. At these scales, fluid-regulated forces are not the only factors that must be examined. Dispersion (or van der Waals) forces may become more important than at larger scales, and the microscopic intermolecular forces of extended media start to have a macroscopic effect on structural stability [18, 19].

In addition to progress in nanotechnology, many biological systems also display adhesion phenomena whose origins can be traced to intermolecular forces. Geckos are known to adhere to smooth surfaces, without any liquid interface. The microscopic arrays of hairs, or setae, on the base of the gecko foot are therefore believed to be the source of such effective dry adhesion [20, 21, 22, 6, 7]. In cellular biology, cytoskeletal morphogenesis is regulated by complex biopolymer networks: Series of long, thin, elastic filaments that form a scaffolding for eukaryotic cells. Mechanical properties of macromolecules such as actin filaments or DNA can be measured by force or deflection analysis at small scales, and polymers adsorbed onto a surface or "zipped" to another molecule can be peeled apart by applying optical tweezers or other external pulling forces [23, 24, 25, 26].

Most of the research into interactions between materials at these scales involve close-range, contact, and sometimes capillary forces, and this is the limit considered by many models and experiments to date [23, 24, 25]. However, long-range forces due to fixed charge distributions, polar, or even non-polar interactions can lead to adhesion events if the right conditions are satisfied. Previous work has characterized the van der Waals attraction between thin flexible objects, both the-

oretically [27, 28] and experimentally [29]. In this chapter, we aim to develop an understanding of the physical mechanisms by which long-range interaction forces compete with elasticity in the adhesion of thin, flexible structures. We first introduce and motivate the prototypical system of interest using a macro-scale experiment showing the hysteretic adhesion of a piece of flexible tape over a plastic substrate. We then develop a model of far-field dry adhesion between two elastic, slender sheets interacting via a power-law potential, and study numerically their relative adhesion. We uncover that phase transitions from unadhered to adhered states occur as dictated by a dimensionless bending parameter representing the ratio of interaction strength to bending stiffness, as well as the form of the interaction potential between the flexible sheets. We then generalize our model in order to study the interactions between several sheets, and show that additional geometrical considerations determine the hierarchical or sequential nature of the adhesion transitions in that case.

2.2 Macro-scale experiment

An example of adhesion transition between between elastic bodies due to long-range interactions may be demonstrated using everyday materials, namely a piece of adhesive tape and a plastic substrate. As shown in Fig. 2.1, this tape can be shown to exhibit complex adhesion properties. The tape is first given a static charge distribution by applying it to a piece of plastic and then removing it swiftly. The tape is initially suspended at the distance shown in Fig. 2.1a, sticky side away from an uncharged substrate. As the suspension distance is slightly decreased (Fig. 2.1b), the tape becomes weakly attracted to the surface. At a critical distance (Fig. 2.1c), the attraction suddenly pulls the tape completely to the surface, where it lays flat along the majority of the substrate. As the tape is pulled away from the surface, the shape exhibits hysteresis (Fig. 2.1d). As the top of the tape is returned to its initial position, the shape remains stuck to the surface, even past the distance where it first adhered.

This simple macro-scale experiment allows us to introduce some qualitative

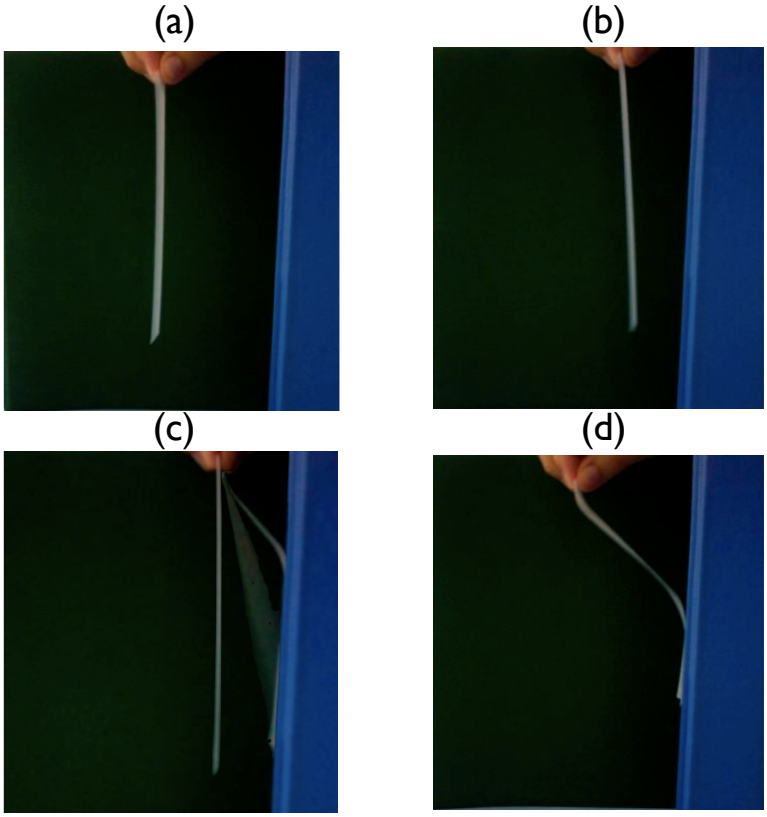

Figure 2.1: (Color online) An example of an adhesion transition between flexible sheets. A piece of adhesive tape is charged electrostatically and then moved slowly towards an uncharged surface, with the adhesive side turned away from the surface. (a): The charged tape is held far from from the surface and no noticeable bending occurs; (b): Weak bending is exhibited just before the critical transition point; (c): At a critical distance the tape moves rapidly towards the surface; (d): Moving the tape away from the wall back to its original position shows hysteretic behavior in the shape of the tape.

features of the adhesion transition, namely a competition between bending and long-range interaction, a sharp transition in shape, and hysteresis. We present below a numerical approach to quantify the behavior of similar, but more general, systems. Note that there are other characteristics of the macroscopic experiment that we will not attempt to model in this work, namely the presence of dynamic effects and force due to gravity.

2.3 Theory

2.3.1 Setup

The system that we study is displayed schematically in Fig. 4.5. Two sheets of length L, thickness $a \ll L$, and width d (not shown) are clamped at their leftmost edges, separated by a distance h, and free to interact along their lengths. We assume the deformations to be two dimensional, and describe each sheet by the vertical deformation of its centerline, denoted y_i, with $i = 1, 2$. While DNA and other semiflexible polymers can become kinked, looped, and otherwise knotted, this study will be limited to the case where the length ratio $\epsilon = h/L \ll 1$, i.e. the long-wavelength limit.

Under these assumptions the total energy of the system is given by

$$E = \frac{1}{2}B_1 \int_0^L y_1''(x_1)^2 dx_1 + \frac{1}{2}B_2 \int_0^L y_2''(x_2)^2 dx_2 + \int_0^L \int_0^L V[x_1, x_2, y_1(x_1), y_2(x_2)] dx_1 dx_2, \tag{2.1}$$

where B_i is the bending modulus of the i^{th} sheet, and x_i is the horizontal distance. The function V describes the interaction potential energy density between the two sheets, as yet unspecified (note that the integration along the widths of the sheets has already been performed formally in V). Extremizing this functional yields mechanical equilibrium, as shown by the following system of coupled integro-

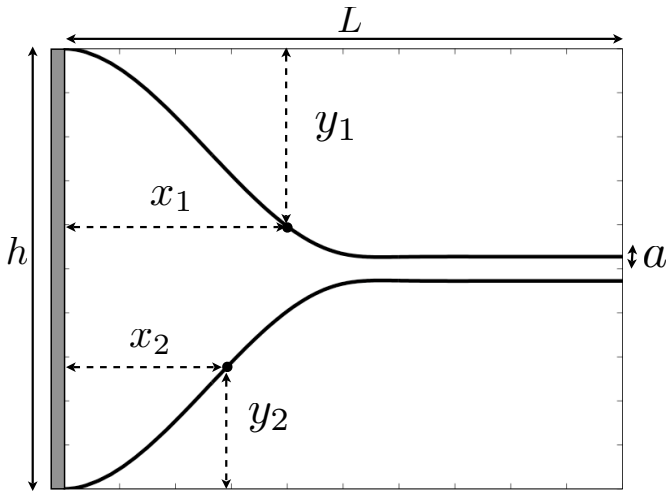

Figure 2.2: A schematic representation of a two-dimensional cross-section for a system of two flexible sheets (see text for notation). Our analysis will be limited to the regime where $\epsilon = h/L \ll 1$.

differential equations with boundary terms

$$B_1 y_1'''' + \int_0^L dx_2 \frac{\partial V}{\partial y_1} = 0, \tag{2.2}$$

$$B_2 y_2'''' + \int_0^L dx_1 \frac{\partial V}{\partial y_2} = 0, \tag{2.3}$$

$$y_1''' \delta y_1 \Big|_0^L = 0 \quad y_1'' \delta y_1' \Big|_0^L = 0, \tag{2.4}$$

$$y_2''' \delta y_2 \Big|_0^L = 0 \quad y_2'' \delta y_2' \Big|_0^L = 0. \tag{2.5}$$

The boundary conditions are set by the physical conditions of the sheets. While there are many possible cases that could be examined, we will consider the common physical scenario in which the sheets are fixed and clamped on the left ($y_1(0) = h$, $y_2(0) = 0$, $y_i'(0) = 0$, $i = 1, 2$) and the right edge of the sheets are force- and moment-free ($y_i''(L) = y_i'''(L)$=0, $i = 1, 2$).

The potential V can be chosen to describe the physical mechanism responsible for the adhesion between the sheets, [15, 25, 20]. In this paper, we are considering a general long-range potential of the form V $\sim 1/r^n$, where $r = \sqrt{(x_1 - x_2)^2 + (y_1(x_1) - y_2(x_2))^2}$, and n is a positive integer. More specifically, we

set

$$V = \sum_{n=1}^{N} \frac{A_n W \sigma^n}{[(x_1 - x_2)^2 + (y_1(x_1) - y_2(x_2))^2]^{n/2}}, \tag{2.6}$$

where σ is the van der Waals-like radius, W is the strength of the interaction, and N is the number of singular modes. The sign of A_n determines whether the interaction is attractive or repulsive. We will examine the more specific form of this general potential where only two terms remain, an attractive term $n = p$ with $A_p = -1$ and a repulsive term $n = q$ with $A_q = +1$. This is the familiar Lennard-Jones-like potential that is used to model intermolecular interactions [19]. We will also work with the case that $\sigma > a$, so no "true" contact between the sheets will occur. In a related study, Oyharcabal and Frisch [27] use a van der Waals-like medium range potential with values of $p = 3$ and $q = 9$ to model the attraction between a thin filament and a nonpolar substrate. Other examples include the van der Waals interaction between two filaments ($p = 6$, $q = 12$), polarized attraction between two sheets ($p = 2$, $q > p$), Coulombic attraction ($p = 1$, $q > p$), and many others (see Ref. [19] for a review). In fact, a surface with an arbitrary charge distribution can be represented by a standard multipole expansion, and in a suitable far-field regime a charged polymer or conducting elastic sheet can be modeled by this potential as well. Very generally, by specifying the values of p and q, any number of potential interactions can be represented, except in the rather exceptional cases in which a power-law potential model is insufficient.

2.3.2 Dimensionless Equations

The system described by Eqs. (2.2)-(2.5) is non-dimensionalized by scaling the vertical displacements by h, and horizontal distances by L. In what follows variables are understood to be dimensionless. In that case, Eqs. (2.2)-(2.5) become

$$y_1''''(x_1) + \Pi_{p,1} I(x_1, y; p, 2) - \Pi_{q,1} I(x_1, y; q, 2) = 0, \tag{2.7}$$

$$y_2''''(x_2) - \Pi_{p,2} I(x_2, y; p, 1) + \Pi_{q,2} I(x_2, y; q, 1) = 0, \tag{2.8}$$

$$y_1(0) = 1, \quad y_1'(0) = y_1''(1) = y_1'''(1) = 0, \tag{2.9}$$

$$y_2(0) = 0, \quad y_2'(0) = y_2''(1) = y_2'''(1) = 0, \tag{2.10}$$

where $\Pi_{p,i} = p\sigma^p L^{3-p} W/B_i$ is a dimensionless quantity, and where we have defined the integral $I(x_i, y; \alpha, k)$ as

$$I(x_i, y; \alpha, k) = \int_0^1 \frac{y\, dx_k}{[(x_i - x_k)^2 + \epsilon^2 y^2]^{\frac{\alpha}{2}+1}}, \tag{2.11}$$

with $y = y_1(x_1) - y_2(x_2)$.

2.3.3 Asymptotics

We now take advantage of the long wavelength approximation ($\epsilon \ll 1$) to simplify the integrals of the form $I(x_i, y; \alpha, k)$. Introducing the substitution $x_1 - x_2 = \epsilon\xi$ we obtain

$$I(x_1, y; \alpha, 2) = \frac{1}{\epsilon^{\alpha+1}} \int_{\frac{-x_1}{\epsilon}}^{\frac{1-x_1}{\epsilon}} \frac{y_1(x_1) - y_2(x_1 - \epsilon\xi)}{(\xi^2 + [y_1(x_1) - y_2(x_1 - \epsilon\xi)]^2)^{\frac{\alpha}{2}+1}} d\xi. \tag{2.12}$$

Expanding to leading order in ϵ,

$$I(x_1, y; \alpha, 2) = \frac{1}{\epsilon^{\alpha+1}} \int_{-\infty}^{\infty} \frac{y_1(x_1) - y_2(x_1) d\xi}{(\xi^2 + [y_1(x_1) - y_2(x_1)]^2)^{\frac{\alpha}{2}+1}} + o\left(\frac{1}{\epsilon^{\alpha+1}}\right) \tag{2.13}$$

$$= \frac{1}{\epsilon^{\alpha+1}[y_1(x_1) - y_2(x_1)]^\alpha} \int_{-\infty}^{\infty} \frac{du}{(1+u^2)^{\frac{\alpha}{2}+1}} + o\left(\frac{1}{\epsilon^{\alpha+1}}\right) \tag{2.14}$$

$$= \frac{\sqrt{\pi}}{\epsilon^{\alpha+1}[y_1(x_1) - y_2(x_1)]^\alpha} \frac{\Gamma(\frac{1+\alpha}{2})}{\Gamma(1+\frac{\alpha}{2})} + o\left(\frac{1}{\epsilon^{\alpha+1}}\right), \tag{2.15}$$

where we have used $u = \xi/[y_1(x_1) - y_2(x_1)]$. The other integrals in Eqs. (2.7)-(2.8) are evaluated similarly. Physically, Eq. (2.15) expresses the fact that, in the long wavelength limit $L \gg h$, each sheet see the other one as being locally flat, and therefore at leading order the integration along the horizontal direction can be performed first.

2.3.4 Identical sheets

Having derived above the general system of equations for two interacting sheets, we now consider the simplified case where the sheets are identical. Defining $z(x)$ as the distance between the sheets, $z(x) = y_1(x) - y_2(x)$, Eqs. (2.7)-(2.10)

become

$$z'''' + \Omega\left(\frac{1}{z^p} - \frac{\beta}{z^q}\right) = 0, \tag{2.16}$$

$$z(0) = 1, \quad z'(0) = 0, \tag{2.17}$$

$$z''(1) = 0, \quad z'''(1) = 0, \tag{2.18}$$

where $\Omega = (2WJ_pL^3\sigma^p)/(Bh^p\epsilon)$, $\beta = (\sigma/h)^{q-p}J_q/J_p$ and $J_\alpha = \Gamma((1+\alpha)/2)/\Gamma(1+\alpha/2)$. Note that the divergent behavior $z = 0$ is prohibited thanks to the repulsive part of the potential in Eq. (2.16). The dimensionless quantity Ω, which we refer to as the bending parameter, is a measure of the relative importance of the interaction forces to the elastic forces, while β is a dimensionless van der Waals-like radius with a numerical prefactor. Hence the symmetric system is completely described by the four parameters $\{\Omega, \beta, p, q\}$.

2.3.5 Numerics

The symmetric nonlinear system described by Eqs. (2.16)-(2.18) is solved numerically on an adaptive grid to an absolute error tolerance 10^{-12}, along with a standard Newton-Raphson shooting method using MATLAB. A continuation scheme in Ω and β allows efficient computation of nearby systems. This treatment is similar to that followed in Ref. [27].

2.4 Adhesion transition

2.4.1 Main result

The main result of this paper is illustrated in Fig. 2.3. For the particular values $p = 3$, $q = 9$ and $\beta = 0.05J_9/J_3$, we display the nondimensional bending energy of the sheets E_B — *i.e.* the sum of the first two terms in Eq. (2.1) — as a function of the bending parameter Ω. Although here we have chosen values for $\{p, q, \beta\}$, the results are similar for other values, with some possible qualitative differences highlighted in the sections below.

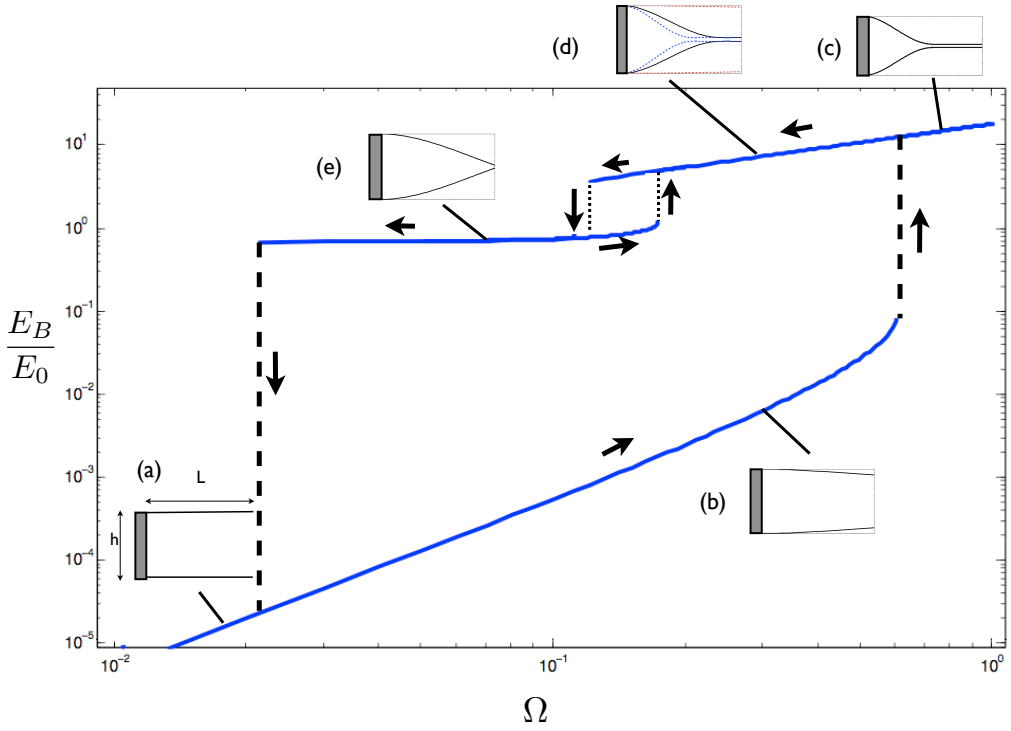

Figure 2.3: (Color online) Dimensionless bending energy E_B/E_0 as a function of the bending parameter, Ω, with $p = 3$, $q = 9$ and $\beta = 0.05J_9/J_3$. Here E_0 is a typical bending energy, $E_0 = Bh^2/L^3$. Representative shapes of the two interacting sheets are shown in the different regions. In Fig. 2.3a, the sheets are essentially straight. Fig. 2.3b shows a slightly bent state due to weak attraction between the sheets. Fig. 2.3c: Past a critical value of Ω, the sheets abruptly adhere to one another. As Ω is decreased, the sheets retain their adhered character, although the shapes change, as seen in Fig. 2.3d (dashed lines indicate shape from Fig. 2.3c). There is also another sharp transition as Ω is decreased even more, and the sheets detach into a bent arc-like shape (Fig. 2.3e). As Ω is decreased further still there is a final sharp transition back to the original weakly attracted shapes shown in Fig. 2.3a.

The sudden shape changes, quantified by the bending energy, are reminiscent of the behavior observed experimentally in §2.2. For $\Omega \ll 10^{-2}$, the two sheets are essentially free-standing, as indicated in Fig. 2.3a. As Ω is increased the sheets are attracted weakly to one another, resulting in a small shape change (Fig. 2.3b). At a critical value of Ω, the bending energy jumps discontinuously and the sheets abruptly snap together (Fig. 2.3c). As Ω increases further, the sheets become more tightly bound, with the unclamped portion becoming smaller.

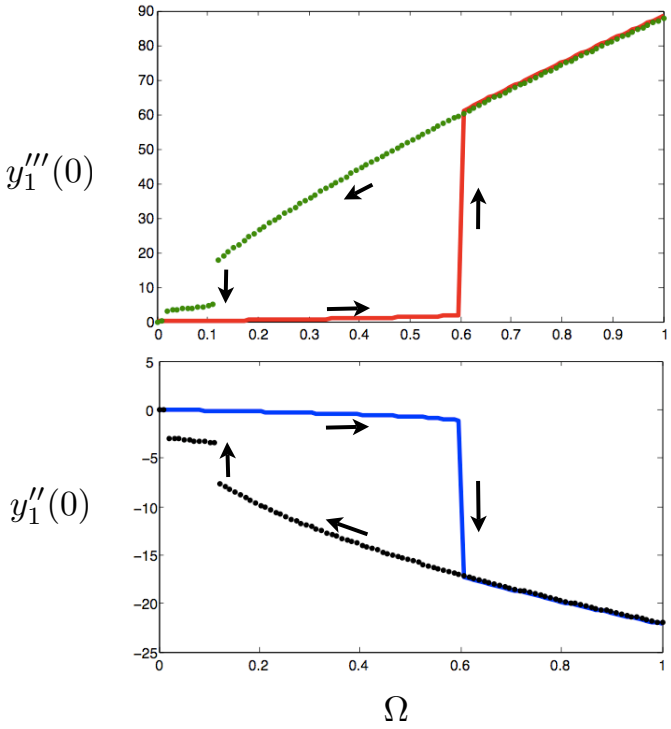

Figure 2.4: (Color online) Dimensionless force, $y_1'''(0)$, and moment, $y_1''(0)$, on the left side of the first sheet as a function of the bending parameter, Ω, for values of $p = 6$, $q = 12$, and $\beta = 0.15J_{12}/J_6$. Note the lack of a second hysteresis loop for these values of the parameters.

If Ω is then decreased, the system exhibits hysteretic behavior, with the sheets remaining adhered as shown in Fig. 2.3d (dashed lines indicate the previous shape from Fig. 2.3c). As Ω is decreased further still there is another discontinuity in the energy, and the sheets once again take on a qualitatively different shape, arc-like, as displayed in Fig. 2.3e. Remarkably, there exists a second (smaller) hysteresis loop on this branch of the energy profile. The jump in the energy at this second hysteresis corresponds to a large change in the contact between the sheet end points and the slope of the sheets. Finally, for decreasing Ω, the sheets return to the positions shown by Fig. 2.3a via another sharp transition.

We also plot in Fig. 2.4 the dimensionless force, $y_1'''(0)$, and moment, $y_1''(0)$, necessary to apply to the left edge of the first sheet to maintain it clamped. For the values of $\{p, q, \beta\}$ considered (6, 12, and $0.15J_{12}/J_6$, respectively), the system models two filaments interacting via van der Waals forces. Much like the shapes

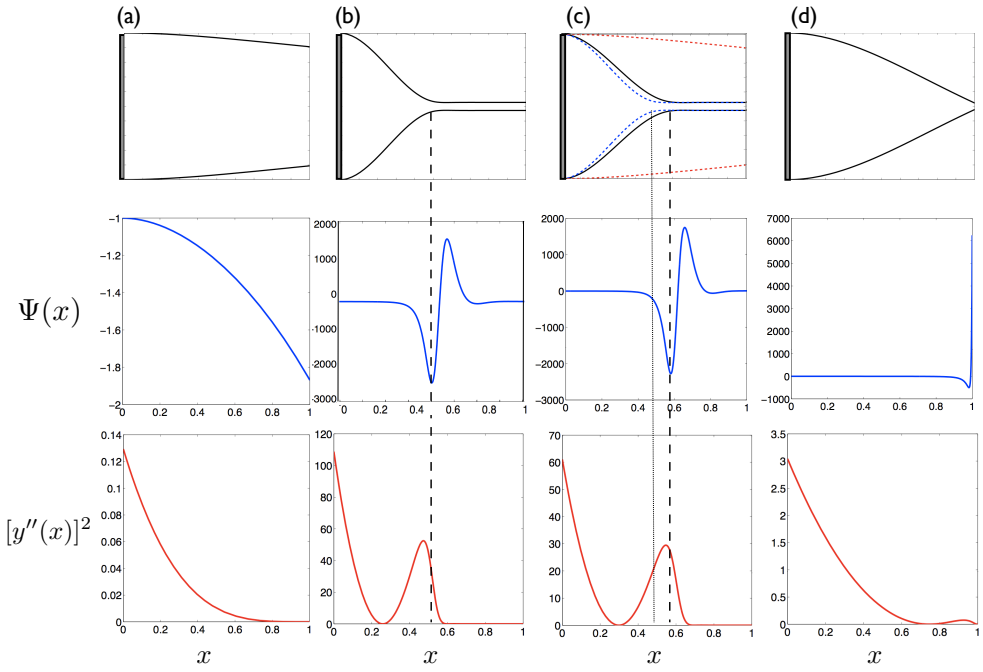

Figure 2.5: (Color online) Bending energy density, $[y''(x)]^2$, and interaction energy density, $\Psi(x)$, for various sheet shapes (top) along the hysteresis loop for $p = 3$, $q = 9$, and $\beta = 0.05 J_9/J_3$: (a) Weak bending ($\Omega = 0.5$), with ends of the sheets approximately straight (zero bending energy); (b): Tightly clamped configuration ($\Omega = 0.89$) with local minimum in the interaction energy density denoting the end of the unclamped region. The local minimum in the interaction energy is in the same vicinity, but not at the same point; (c): Hysteretic clamped shape ($\Omega = 0.5$), with vertical dashed line indicating the position of the local maximum of bending energy density, and the vertical dotted line indicates where this local maximum was in Fig. 2.5b. The red (outer horizontal dashed) line in the upper inset denotes the weakly bent shape from (a), while the blue (inner horizontal dashed) line denotes the shape from (b). (d): Arc-shape ($\Omega = 0.11$), with a notable small local maximum in $\Psi(x)$ near the end point indicating localized adhesion.

themselves, the forces and moments undergo sharp transitions and exhibits hysteresis. Note that if the sheets were free to interact they would adhere along their entire length, and a force would need to be applied to one end in order to peel them apart. In essence the same effect is seen in our system. Hysteresis is known to occur in the strong loading of cantilevers [30], and recent experimental investigations into the peeling of CNTs from a substrate have reported results qualitatively similar to ours [29].

2.4.2 Phase transition and physical quantities

By viewing the shape-change as a phase transition, where the control parameter is Ω instead of temperature, we can borrow several concepts from statistical physics in order to further characterize our model system. The natural order parameter to assign is the distance between the sheets, $z(x)$, as $z(x) = 1$ denotes totally unadhered sheets and $z(x) = \beta^{1/(q-p)}$ corresponds to complete adhesion (see Eq. 2.16). A natural analogy exists between the energy functional given by Eq. (2.1) and a one-dimensional magnetic system with two-component spin subject to an external field [31]. In our system, there is an energy penalty associated with deforming the sheets (analogously, misaligning spins), and there is an interacting field that acts to order the system (analogously, the external magnetic field). It is known that even at zero temperature, the magnetic system displays a phase transition at a critical value of the ordering field (except in the thermodynamic limit of the sheet length $L \to \infty$), and as such we could expect such behavior from our system as the relative field strength (i.e. Ω) is increased.

In analogy to the external field of the magnetic system, we define an interaction energy density given by $\Psi(x) = \Omega\,(-1/z^p + \beta/z^q)$, and discuss the qualitative changes that govern the phase behavior of the system by studying the minima in the free energy (see Ref. [32] for a textbook treatment). When a local minimum appears or disappears along the length of the sheets we can expect a change in shape, and whether this change is dramatic or smooth will correspond to a first- or second-order phase transition (first-order when $\partial E/\partial\Omega$ is discontinuous, second-order when $\partial^2 E/\partial\Omega^2$ is discontinuous).

In Fig. 2.5, we display a representative sampling of the energy densities (bending and interaction energies) with their associated shapes, for $p = 3$, $q = 9$, and $\beta = 0.05 J_9/J_3$. We see qualitatively different energy densities, confirming the transitions between three different phases. In Fig. 2.5a, the sheets store little elastic energy and are only weakly attracted. Past the critical adhesion point, the shape as displayed in Fig. 2.5b now shows a large energetic favorability from the interaction force, with large deformation energy penalties on the left edges of the sheets and at the end of the un-adhered length. As the bending parameter is

increased further, the spatial location of the energy minima shifts, as displayed by Fig. 2.5c. The length of the adhered region (or domain wall), δ, increases with Ω as $\delta \sim \Omega^{-1/4}$, as expected from the boundary layer scaling arising from Eq. (2.16). This scaling is confirmed by our numerical simulations (not reproduced here). Decreasing Ω, and coming down on the hysteresis loop, at a lower critical value of Ω the adhered sheets become arc-like, and the second local minimum in $\Psi(x)$ disappears (see Fig. 2.5d).

2.4.3 General Behavior

Although our investigation to this point has considered particular values for the parameters $\{\beta, p, q\}$, qualitative changes in the hysteresis and transition behavior can be obtained for different values of these parameters. Not only can the hysteresis region be made to shrink, but it can also disappear entirely. In addition, while the transitions seen so far have been first-order, by tuning the model parameters this transition can be made to become second-order.

These different behaviors are illustrated in Fig. 2.6, where for convenience we have introduced the parameter $b = \beta J_p / J_q$. As we saw above, there are three characteristic shapes for the sheets that we will denote as weakly bent (W), adhered/clamped (C), and arc-shaped (A). The areas that exhibit each of these shapes are depicted in Fig. 2.6. In Fig. 2.6a and b, we display the total energy (bending plus attraction) for a system with $p = 6$, $q = 12$. These values model the attraction between two thin non-polar filaments, and the characteristic shapes seen are similar to those in Fig. 2.3. If b is increased, representing an increase in the minimum adhesion distance between the fibers, the arc-shapes and associated phase transition vanish. Similarly for the case where $p = 3$ and $q = 9$ [27], increasing the value of b causes the hysteresis region to shrink and the arc-shape vanishes (Figs. 2.6c and 2.6d). Furthermore, the hysteresis region can be made to disappear completely for $p = 2$ and $q = 4$ (Fig. 2.6e and 2.6f).

The transformation of a first-order transition into a second-order transition indicates that there may be a cusp catastrophe in the parameter space we are exploring [33]. For the case $p = 3$ and $q = 9$, we plot on Fig. 2.7 the bending

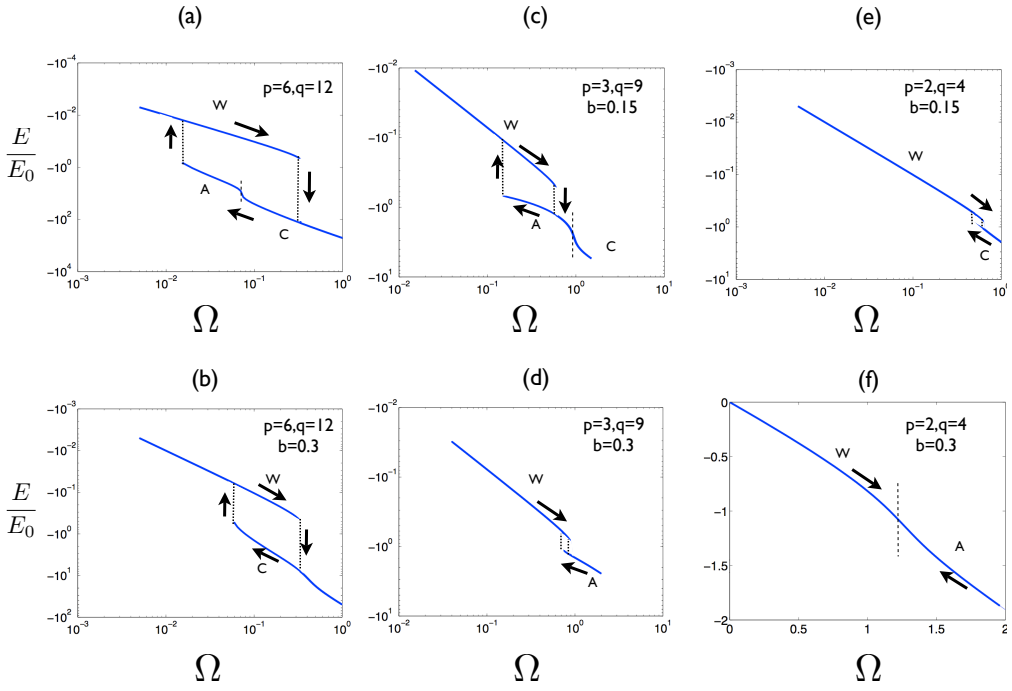

Figure 2.6: (Color online) A comparison of total energies for the system (bending + attraction energy) for different values of p, q, and β. For convenience we have introduced the parameter $b = \beta J_p/J_q$. (a): For $p = 6$ and $q = 12$, these values model the attraction between two thin non-polar filaments. Dotted lines denote sharp phase transitions, while dashed denote smooth transitions. This system displays all three characteristic shapes; (b): By changing the value of b so that the sheets do not come as close during adhesion, the tightly clamped region is seen to disappear; (c) and (d): For $p = 3$ and $q = 9$, further qualitative changes shrink the hysteresis region and cause the disappearance of characteristic shapes; (e) and (f): In the case where $p = 2$ and $q = 4$, the hysteresis can disappear completely even in the presence of a transition.

energy landscape as both Ω and $b = \beta J_3/J_9$ are varied. For small values of β, the first-order nature of the transition is apparent. For a fixed value of Ω, increasing β decreases the area of hysteresis, until a critical value is reached where the hysteretic behavior vanishes completely.

2.4.4 Non-identical sheets

We have considered so far the case where the two sheets are identical. If we allow instead their bending rigidity to be different, we now have two parameters,

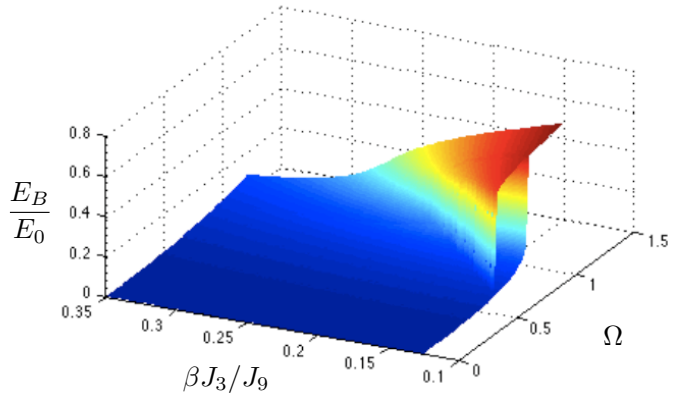

Figure 2.7: (Color online) Bending energy landscape for $p = 3$, $q = 9$ over a range of β and Ω. Note that there is a distinct cusp in this parameter space, indicative of the "catastrophic" behavior that is associated with first order phase transitions.

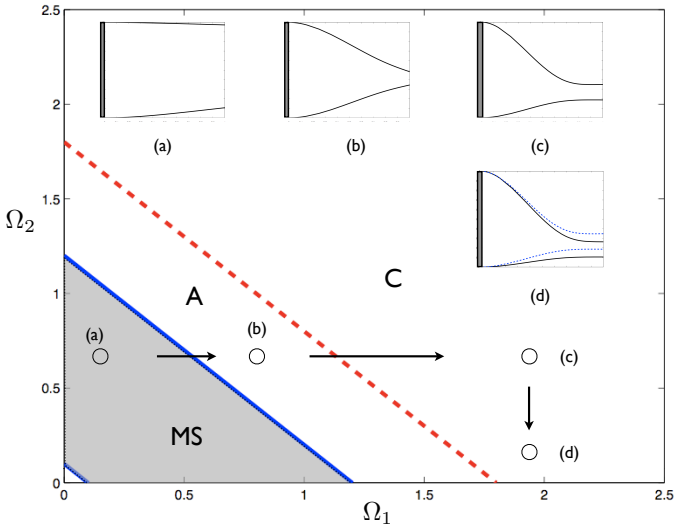

Figure 2.8: (Color online) Phase diagram of sheets with asymmetric bending parameter for $p = 3$, $q = 9$, and $\beta = 0.15 J_3/J_9$. There is a region of multiple stability (MS) where arc-shapes and weak bending are both possible, arc-shapes only (A) and tightly clamped (C) sheets. (a): In this region, the sheets are either bending weakly, or in the hysteretic case they exhibit arc-shapes; (b): As Ω_1 is increased, the sheets snap together into an arc-shape (a first-order transition); (c) As Ω_1 increases further, there is a smooth variation from arc-shapes into clamped (*i.e.* a second-order transition, dashed line); (d) If Ω_1 remains fixed, and Ω_2 is decreased, the bottom sheet will become relatively more rigid, producing a net shift in the equilibrium adhesion position (the dashed lines indicate the adhesion shape in Fig. 2.8c).

$\Omega_i = (2WJ_pL^3\sigma^p)/(B_ih^p\epsilon)$ for $i = 1, 2$. In this case, the difference in rigidity causes a change in both the equilibrium point of adhesion and the critical values of Ω_i. The different shapes can be characterized by a phase diagram that maps the transition points for different values of the two bending parameters, as displayed on Fig. 2.8. Three distinct regions exist: Multistability of both arc-shapes and weak bending (MS), arc shapes exclusively (A), and adhered or clamped states (C). As shown in Fig. 2.8a, for small values of Ω_2 and Ω_1, weak attraction occurs, unless the hysteretic regime has been entered, in which case there will be adhesion (not shown). As Ω_1 is increased past the fixed value of Ω_2, the sheets adhere in an asymmetric arc shape (Fig. 2.8b). This transition is first-order, and the sheets snap together. As Ω_1 crosses the second-order transition threshold (dashed line in Fig. 2.8), the shapes smoothly evolve into a clamped phase (Fig. 2.8c). In this final clamped state, the position of the adhered portion of the sheets depends on the relative values of the bending parameters (Fig. 2.8d).

2.4.5 Adhesion of three sheets

We now consider the adhesion transition for an array of multiple sheets, and illustrate the complexity and richness of the system considered on a few examples. Assuming nearest-sheet interaction for simplicity, with identical potentials, we can easily extend the modeling approach offered above to the case of N interacting sheets [1]. The equation of shape for the ith sheet, $1 \leq i \leq N$, is then given by

$$y_i'''' + \Omega_i \sum_j \left[\frac{1}{(y_i - y_j)^p} - \frac{\beta}{(y_i - y_j)^q} \right] = 0, \tag{2.19}$$

where the sum on j runs over nearest neighbors, and Ω_i, p, q, and β are defined as in the $N = 2$ case.

For multiple sheets, any asymmetry in the system now plays a role in determining the order in which sheets adhere to one another. For three sheets, unless there is perfect symmetry between the top and bottom sheet, the adhesion events always occur in a sequential fashion (see Fig. 2.9 and 2.10). Specifically, two sheets

[1] Even for $p = 1$ (long-ranged or Coulombic attraction) adding contributions from all neighbors does not qualitatively change our results.

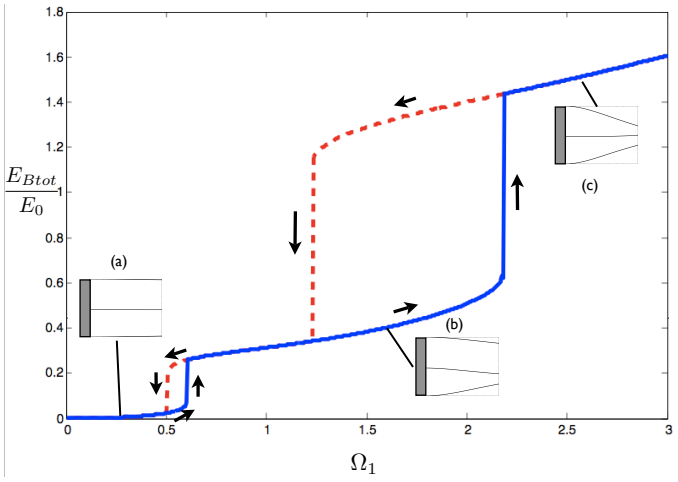

Figure 2.9: (Color online) Sequential adhesion transition for three sheets: $(1,1,1) \rightarrow (1,2) \rightarrow (3)$. Two consecutive first-order transitions occurring for the total bending energy of the sheets as a function of the (identical) bending parameters in the case $p = 3$, $q = 9$ and $\beta = 0.35 J_9/J_3$. An inherent asymmetry has been introduced in that the middle sheet is pinned slightly closer to the bottom sheet than to the top one (five percent difference in height). (a): Weak attraction; (b) As the bending parameters are increased, a first-order adhesion transition takes place where two of the three sheets adhere; (c): A second first-order transition occurs when the three sheets adhere. Both transitions display hysteresis.

first come together, and then adhere to the third sheet for a further increase in the relevant bending parameter. By locating the middle beam slightly closer to one of its neighbors, this sequential can be made to occur preferentially between two previously-chosen sheets (by changing the clamping distance, the competition between bending and interaction energy changes, and in effect one of the bending parameters gets a boost from the geometric asymmetry). For three identical sheets, as the bending parameters are increased, there is a transition from the weakly attracted phase (Fig. 2.9a and 2.10a) to a regime where two sheets adhere to each other (Fig. 2.9b and 2.10b). As the bending parameters are further increased, a subsequent transition occurs where all three sheets come together (Fig. 2.9c and 2.10c). As for the $N = 2$ case, tuning the value of β can change the nature of the first adhesion transition (a$\rightarrow$b), from first-order (Fig. 2.9) to second-order (Fig. 2.10). The second adhesion transition, however, remains first-order.

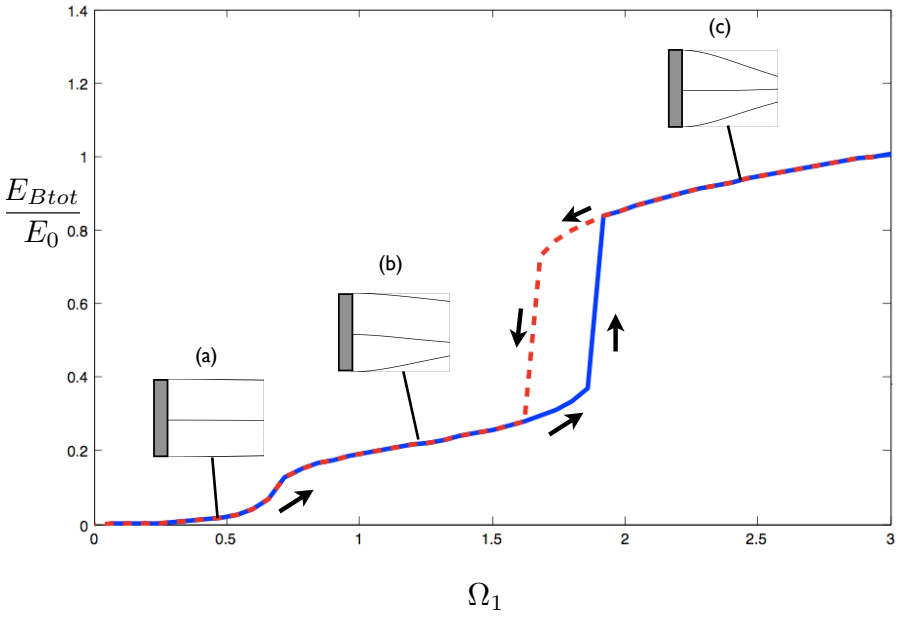

Figure 2.10: (Color online) Same as Fig. 2.9, but for $\beta = 0.45 J_9/J_3$. In contrast with the case depicted in Fig. 2.9, the first adhesion transition is now of second order.

2.4.6 Adhesion of four sheets

When a fourth sheet is added, the adhesion transitions can be made to occur in either a hierarchical or a sequential fashion. This is illustrated in Figs. 2.11 and 2.12.

We show in Fig. 2.11 an example of sequential adhesion for four identical sheets, similar to the one discussed in the three-sheet case. The values of p, q and β, as well as the geometric asymmetry, have been chosen so that there is a mix of first- and second-order transitions (see figure captions). The relative distances between the four sheets are as follows: The top sheet is pinned at $y = 3h$, the second-highest at $y = 1.8h$, the third-highest at $y = 0.7h$ and the final sheet at $y = 0$. As all four bending parameters are increased at the same rate, the sheets start by a state of weak attraction, with more bending exhibited by the sheets that are closer to one another. Past a critical value of the bending parameters, there is a second-order transition for these values of the model parameters, and the two bottom sheets adhere (Fig. 2.11b). As the bending parameters are increased

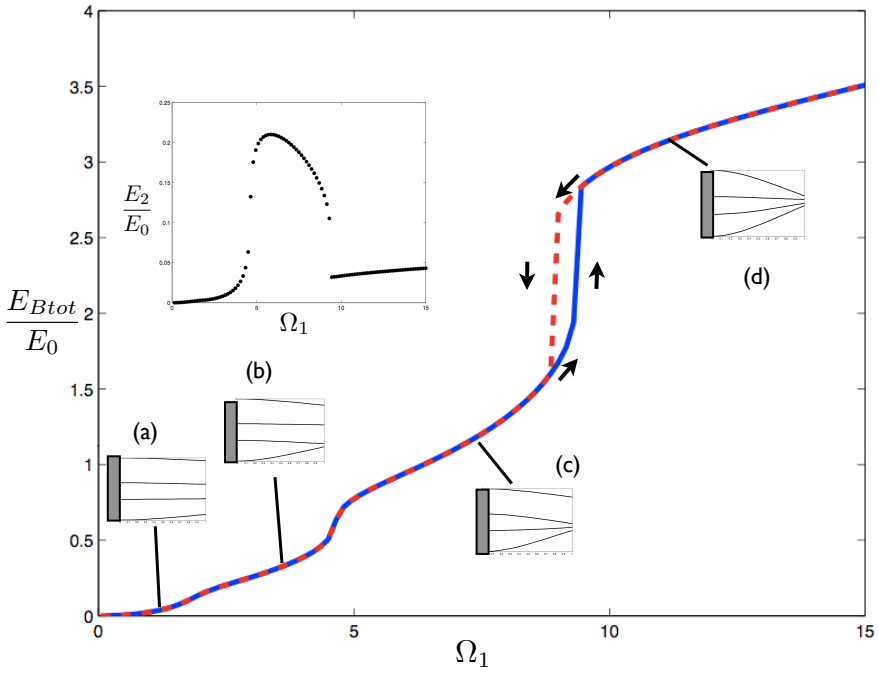

Figure 2.11: (Color online) Sequential adhesion transition for four sheets: $(1,1,1,1) \rightarrow (1,1,2) \rightarrow (1,3) \rightarrow (4)$. Total bending energy as a function of the (identical) bending parameters for $p = 1$, $q = 2$, and $\beta = 0.1J_2/J_1$. The four sheets form first an adhered pair, then a triplet, then all four clamp together. Adhesion in this manner is highly dependent on the asymmetry of the array of multiple structures. In this case the top sheet is placed at $y = 3h$, the second highest at $y = 1.8h$, the third at $y = 0.7h$ and the lowest beam placed at $y = 0$. (a): Weakly bent state; (b): Adhesion between the lower two sheets; (c): Adhesion between the lower three sheets; (d): Adhesion of all four sheets. Inset: Non-monotonic variation of the bending energy in the second-highest sheet.

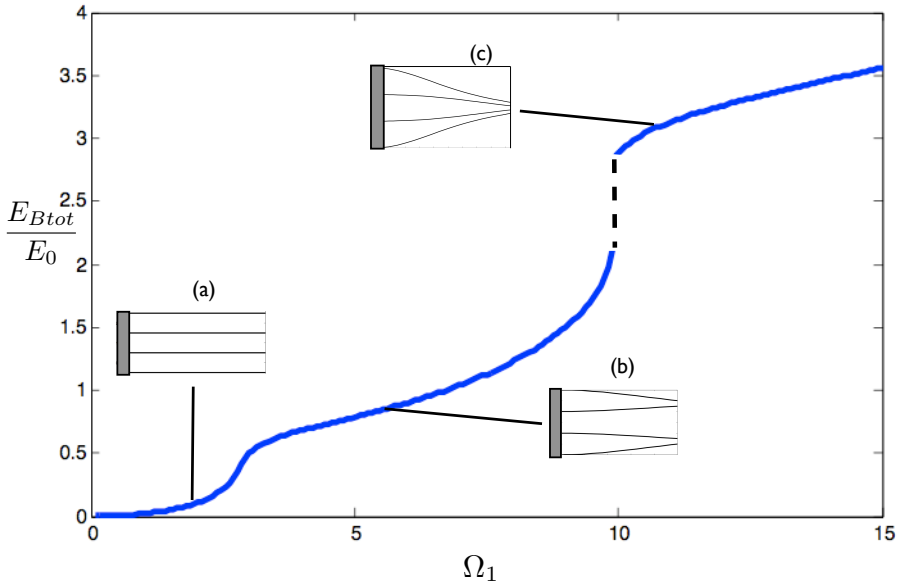

Figure 2.12: (Color online) Same as Fig. 2.11 except that the original distances between each sheet is now identical. As a result, the adhesion transitions occur in a hierarchical fashion: $(1, 1, 1, 1) \rightarrow (2, 2) \rightarrow 4$.

further, another second-order transition takes place and the lower three sheets adhere (Fig. 2.11c). Finally, a final first-order transition occurs when the four sheets adhere (Fig. 2.11d). Note the non-monotonic variation of the bending energy in the second-highest sheet (inset of Fig. 2.11).

An example of hierarchical adhesion transition is displayed in Fig. 2.12, where we plot the total bending energy profile for a symmetric four-sheet system (*i.e.* there is no asymmetry in the relative distances between the sheets). As the bending parameters are increased, a second-order phase transition leads to adhesion between two pairs of sheets (Fig. 2.12a). First-order transitions are also possible for other values of the model parameters (not shown here). As the bending parameters are increased further, a first-order transition occurs and the four sheets all adhere to one another (Fig. 2.12b). Remarkably, in this case, the first-order transition does not display any hysteresis.

2.5 Conclusion

In this chapter we have studied the prototypical dry adhesion problem between flexible sheets or filaments, and focused on their morphological transitions. Motivated by a simple macro-scale experiment showing hysteretic adhesion, we have introduced a model of dry adhesion between two elastic, slender sheets interacting via a power-law potential, and studied numerically the transitions in their conformations. Given a particular form of interaction potential, the system is completely described by a single dimensionless parameter quantifying the relative effect of long-range attraction and bending rigidity, and governing the nature of the adhesion transitions (first or second-order). We have also generalized the model to multiple sheets, showing in particular that additional geometric considerations dictate the order in which structure adhere to each other. The physical systems modeled here include the interactions between charged sheets, or between nonpolar filaments. Future work will focus on the presence of thermal fluctuations allowing the adhered states to "jump" from one state to another. We will also consider the case where the filaments are actuated, and will include the effect of hydrodynamic interactions. Finally, using an approach similar to ours, the adhesion of three-dimensional structures such as coiled filaments or planar arrays could be investigated.

Acknowledgments

We would like to thank Saverio Spagnolie for many useful conversations and help with some numerical aspects of this work. This work was funded in part by the National Science Foundation (grants CTS-0624830 and CBET-0746285 to Eric Lauga). This chapter is reproduced in it's entirety from A. A. Evans and E. Lauga, *Phys. Rev. E*, **79**, 066166, 2009.

Chapter 3

Active filament locomotion

3.1 Introduction

In the highly viscous environment inhabited by micro-organisms, locomotion is a difficult task, and one rarely achieved in the absence of fellow organisms, boundaries or other obstacles. Because drag forces from the fluid dominates inertia, swimming becomes a problem for microscopic life qualitatively different from that of larger organisms such as fish, and nature has evolved several strategies for solving it. Flagellated organisms such as bacteria and spermatozoa utilize the fluid drag anisotropy of slender filaments (flagella) in order to propel themselves through a viscous fluid [10]. From a biological standpoint, both prokaryotic and eukaryotic flagella serve the same purpose, to propel the organism through the fluid, but from a mechanical standpoint the filaments are quite different. Bacteria such as *E. coli* and *B. subtilis* actuate passive helical filaments using rotary motors embedded in the cell walls, and whose rotation gives rise to propulsion [34, 35]. In contrast, spermatozoa (and more generally, eukaryotic) flagella are active filaments. They possess an internal musculature, termed the axoneme, which deforms in a wave-like fashion due to the action of molecular motors. These motors generate time-varying and coordinated bending moments along the flexible flagellum, giving rise to traveling waves, and propulsion of the cell [36, 10]. In that case, the waveform displayed by the cell is a physical balance between the motor activity, the flagellum elasticity, and the fluid forces.

Near solid boundaries, the behavior of both types of swimming cells is strongly affected. Since the governing equations for inertialess fluid flow are time invariant, the geometry of the system fully defines the hydrodynamics. Bacteria swim in circles near a wall, as the chirality of the flagellar rotation induces a hydrodynamic torque on the body [37, 38, 39]. Boundaries also tend to hydrodynamically attract swimming cells, and as a result the steady-state distribution of motile cells strongly peaks near walls [40, 41, 42, 43, 44, 45]. Near walls, large arrays of cilia (short flagella) are known to synchronize, and display coordinated modes of deformation known as metachronal waves [46, 36, 47, 48, 9, 49].

One topic of renewed interest concerns the dynamics of spermatozoa in confinement, as relevant to the situation in mammalian reproduction [50]. Early

theoretical studies considered flagellated cells with waveforms unchanged by the presence of walls. In that case, because of increased drag forces, the cells have to increase their work against the fluid to maintain their waveforms, and as a result they speed up when near a boundary [51, 52, 53, 54, 42]. If instead the cells are assumed to work with a fixed power, the presence of a boundary leads in general to a decrease of the swimming speed [51, 52].

Physically, the speed at which a cell swims is a balance between the propulsive force generated by its flagellum and the drag from the surrounding fluid. Near a boundary, both the flow field generated by the flagellum and the subsequent propulsion generated are expected to be modified, but in a manner which has not been quantified yet.

Recently, an experimental investigation was carried out using optical trapping on human spermatozoa to investigate the influence of boundaries on force generation. Briefly, spermatozoa cells swimming near and parallel to a cover glass (distance about 5 μm) were optically trapped, and then moved to a pre-defined distance of up to 100 μm from the glass surface. As the flagellum of the trapped cell continuously beat, the trap power was then gradually attenuated until the cell escaped. The magnitude of the propulsive force applied by the cell, equal to the minimum force required to hold the cell in place by the optical trap, was found to be decreased by the presence of the glass surface [55]. These results indicate that the cells do not maintain their waveforms, as for a cell with a fixed waveform the propulsive force would increase near the wall. This experimental result suggests therefore that, for eukaryotic cells, the interplay between flagellum elasticity, internal actuation, and hydrodynamics can lead to a non-trivial relationship between the environment (here, confinement) and the propulsive force generated by the cells.

In this chapter, we use a series of simple models to examine the propulsive effects of a solid boundary on passively actuated filaments and model flagella. Our work aims at capturing the essential physics that describes the geometric effects on the body, and builds on previous studies of flagellar locomotion far from external influences, both for passive filaments [56, 57, 58, 59, 60], and for active flagella

[61, 62, 63, 64, 65] (see also Ref. [10] and references therein). By considering different modeling approaches for the filament actuation, and by quantitatively including the change in viscous friction due to the presence of the wall, we predict analytically the change in flagellar waveform, as well as the resulting change in propulsive force. We demonstrate that the relationship between the wall-flagella distance and the propulsive force it generates is in general non-monotonic. For the case of passive flagella actuated at one end, the presence of the wall increases the propulsive forces generated by the filament dynamics for displacement-driven actuation, but decreases them in the case of force-driven actuation. In contrast, for active filaments we demonstrate that the manner in which a solid wall affects propulsion cannot be known a priori, but is instead a complicated function of the flagella frequency, wavelength, their boundary conditions and the manner in which the molecular motors self-organize to produce oscillations.

The chapter is organized as follows. We start with a summary of the general class of elastohydrodynamics problems, and prescribe our course of action for determining the propulsive force and force gradients in the presence of a wall for our models (Sec. 3.2). Following this we consider a passive filament actuated at one end, and the modification of the thrust it produces in the presence of the no-slip boundary (Sec. 3.3). We then consider two models for active flagella swimming very close to the wall, first the case of a prescribed internal sliding force, and then the more realistic case of flagellar beating via self-organization of molecular motors in the axoneme (Sec. 3.4). In both cases, we determine the propulsive force, and how it is modified by the presence of the wall. We finish with a discussion of our results in the context of spermatozoa locomotion (Sec. 3.5)

3.2 Elastohydrodynamics and setup

3.2.1 Setup

The physical system that we will investigate is illustrated schematically in Fig. 4.4. We consider a single flagellated cell (or synthetic device with a flagellum-like filament), for which the flagellum undergoes planar beating a distance h from

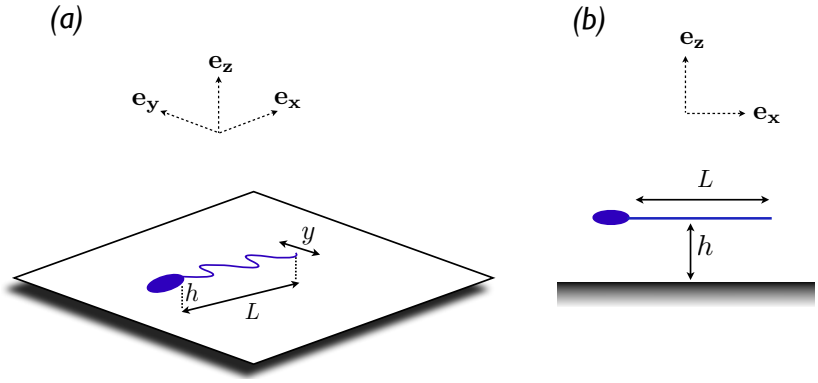

Figure 3.1: (color online) Schematic diagram of a flagellated cell (or passive flexible filament) in the presence of a stationary no-slip boundary. (a): 3/4 view of the model system. The planar beating of the flagellum or filament takes place parallel to the plane of the wall (x, y), and the cell is located at a distance h from the surface. For simplicity we ignore the head effects in this work; this is a reasonable assumption as many experiments to measure the propulsive force would anchor the head in place (e.g. an optical trap or micropipet). (b): Side-view of the model system. Note that from this angle the flagellum or filament appears only as a straight rod, as it is assumed to beat along the y direction.

the surface of a solid boundary. The plane of actuation is assumed to remain parallel to the plane of the wall (directions x and y in Fig. 4.4). In the experiment of Ref. [55], when the cells are trapped, their plane of beating is parallel to the surface, and thus it is a reasonable approximation to assume that it remains so at different heights. We will consider both the case of a passive filament actuated at one end (Sec. 3.3) as well as an active filament with internally distributed actuation (Sec. 3.4)

3.2.2 Hydrodynamics

Since the Stokes equations are time-invariant, the geometry of the system completely defines the fluid dynamics at zero Reynolds number. Although the governing equations are themselves linear, nonlinearities in the shapes of swimming organisms can make calculating the flow difficult. Furthermore, because the flow is determined by the instantaneous shapes of the surfaces immersed in the flow, nonlocal hydrodynamic effects can make the calculations impossible to do without

numerical analysis.

Fortunately, for flagellated organisms the slenderness of the swimming surface in question leads to several simplifications that can be made to the fluid dynamics. Using the asymptotic limit of a slender filament, the force acted by the fluid on the moving filament is approximately given by [66]

$$\mathbf{f}_{fl} = -\left[\zeta_{\parallel}\hat{\mathbf{t}}\hat{\mathbf{t}} + \zeta_{\perp}(\mathbf{I} - \hat{\mathbf{t}}\hat{\mathbf{t}})\right] \cdot \mathbf{v}, \tag{3.1}$$

where $\zeta_{\perp}$ and $\zeta_{\parallel}$ are the force-velocity resistance coefficients derived from resistive force theory ($\zeta_{\parallel} < \zeta_{\perp}$) [10], and accounting for filament motion perpendicular and parallel to the filament axis respectively; here $\hat{\mathbf{t}}$ is the unit tangent vector along the filament, $\mathbf{I}$ is the identity tensor, and $\mathbf{v}$ is the velocity of the filament as it moves through the quiescent fluid.

In addition to slenderness, for small amplitudes of the flagellar beat the geometric terms simplify considerably. Although real flagella beat with a large amplitude, experiments and numerics have shown that corrections to linearized dynamical shape equations are sub-leading [67, 68, 60]. In the linearized regime, only the normal velocity component of the filament is important for calculating the fluid force, as the tangential motion enters only for higher-order curvature or bending of the filament. In that case, we can represent the amplitude of the filament perpendicular to the propulsive direction as a function $y(x,t)$, and the fluid drag on the filament can be simply expressed in terms of the amplitude y as $\mathbf{f}_{fl} \approx -\zeta_{\perp}\partial y/\partial t\, \mathbf{e}_y$.

3.2.3 Flexibility and activity

In order to model propulsion, we need to balance the expression for the fluid force on the filament with the internal forces, $\mathbf{f}_{int}$, of the model flagellum. In the case of a passive filament actuated at one end, only the elastic forces contribute to this term. For a model of spermatozoa, the internal distribution of molecular motors in the axoneme leads to an active bending moment that contributes to force and torque balance. In the inertialess realm of low Reynolds number that is inhabited by the swimming cells that we examine, the total force on each infinites-

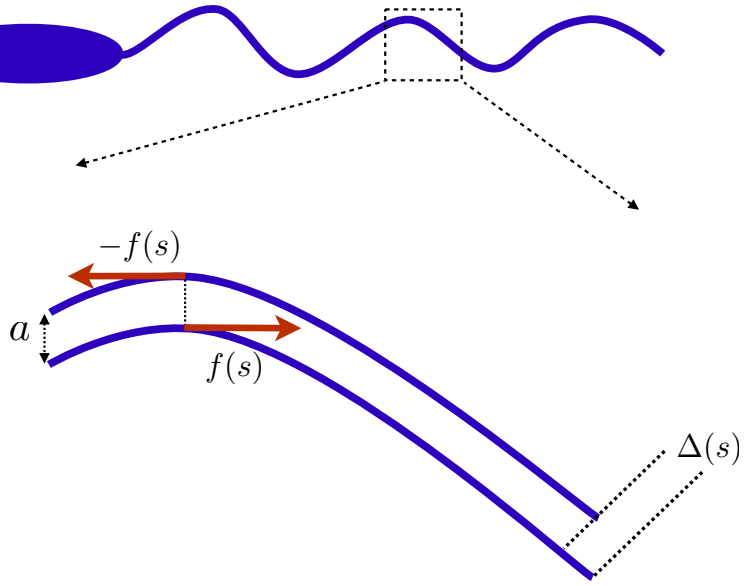

Figure 3.2: (color online) Schematic of a flagellated micro-organism swimming via an active flagellum. The inset shows the model of the active filament that we use in this analysis (adapted from Ref. [63]). The two pieces of the filament slide past one another, each exerting an equal and opposite active force $f(s)$ that is dependent on the position along the flagellum (the arclength s). This produces a sliding displacement Δ. In the simplest case, that of purely elastic response, and for small amplitude motion, this displacement Δ induces a restoring force that is proportional to the magnitude of $f(s)$. The distance between filaments, a, has been exaggerated for viewing purposes.

imal element of the flagellum sum to zero, and therefore mechanical equilibrium is written as

$$\mathbf{f}_{fl} + \mathbf{f}_{int} = 0. \tag{3.2}$$

Thin passive filaments are well modeled by the elastic beam theory [69]. Their elastic strain energy associated with deformation is given by

$$E_{el} = \frac{A}{2} \int_0^L \kappa(s)^2 ds, \tag{3.3}$$

where A is the bending rigidity of the filament, L its length, and $\kappa(s)$ its local curvature along the arclength, s.

For an active filament that is powered by an internal musculature, such as a eukaryotic flagellum, we must consider not only similar elastic restoring forces, but also any internal actuation forces. We use in this paper the model of Camalet &

Julicher [63] to address the mechanics of active filaments, as illustrated in Fig. 3.2. The active filament is assumed to be composed of two inextensible elastic beams which are attached to the basal (or head) region, but allowed to bend relative to one another, and acted upon by a distribution of equal and opposite active force $f(s)$. As the filaments bend, they induce a distribution of sliding displacements, $\Delta(s)$, given geometrically by

$$\Delta(s) = \int_0^s a\kappa(s')ds', \tag{3.4}$$

where a is the fixed distance between the filaments at the base. The work done by the filament against the internal forces is then added to the enthalpy functional, and we get

$$E = \int_0^L ds \left[\frac{A}{2}\kappa^2(s) + f\Delta(s)\right]. \tag{3.5}$$

In the case of a passively actuated filament, the internal forces are zero, and thus only the elastic contributions enter the equations of motion. Extremizing the energy given by Eq. (4.7), for a particular form of the active forces, yields the total internal force per length on the flagellum, $\mathbf{f}_{int}$, which must then be equal and opposite to the fluid force.

3.2.4 Propulsion and wall effects

Given a system, either the passive or active filament, and a set of boundary conditions for the flagellum corresponding to a given physical situation, the elastohydrodynamics balance allows us to solve for the flagellar beating pattern and thus for the propulsive force. For small-amplitude motion, the propulsive force, defined as the force acted by the beating flagellum on the surrounding fluid when it is beating but not swimming, is given by

$$\mathbf{F} = \left[(\zeta_{\parallel} - \zeta_{\perp}) \int_0^L \frac{\partial y}{\partial t}\frac{\partial y}{\partial x}dx\right] \mathbf{e}_x, \tag{3.6}$$

where $\mathbf{e}_x$ is the unit vector along the average position of the beating filament [59] (see Fig. 4.4). In particular, if $y(x,t)$ deforms as a pure traveling wave propagating

in the $+x$ direction, $y(x,t) = y_0(x-ct)$, we get $\mathbf{F} = \left[(\zeta_\perp - \zeta_\parallel)c\int_0^L (\partial y_0/\partial x)^2 dx\right]\mathbf{e}_x$. In that case, the force on the fluid is in the $+x$ direction, and therefore the force on the filament, and the swimming direction if it was free to swim, is in the $-x$ direction.

To determine the values of $\zeta_\perp$ and $\zeta_\parallel$ in Eq. (3.6), we look at previous work calculating friction coefficients for slender bodies near walls [36]. For a slender body of radius a and length L in an unbounded fluid the drag coefficients can be calculated asymptotically in the slender limit $a \ll L$, and are given by

$$(\zeta_\perp)_\infty \approx \frac{4\pi\mu}{ln(2L/a) + C_1} \quad (\zeta_\parallel)_\infty \approx \frac{2\pi\mu}{ln(2L/a) + C_2} \tag{3.7}$$

where μ is the fluid viscosity and C_1 and C_2 are $O(1)$ constants that depend on the specific geometry of the filament. Near a boundary, if h is the distance between the filament and the wall, the situation relevant to the experiments in Ref. [55] is that of $h \lesssim L$. In this near-field limit, the resistance coefficients relevant to the planar beating geometry considered in Fig. 4.4 are given by

$$\zeta_\perp \approx \frac{4\pi\mu}{\ln(2h/a)}, \quad \zeta_\parallel \approx \frac{1}{2}\zeta_\perp. \tag{3.8}$$

The far-field limit, $h \gtrsim L$, yields only a small correction to the values of $\zeta_\perp$ and $\zeta_\parallel$ in Eq. (3.7) which would likely be too small to be measured experimentally, and thus we will not consider this case here. For a comprehensive account of these calculations see Ref. [36] and references therein. Experiments on sedimenting cylinders near boundaries were considered in Ref. [70], where it is shown that the difference in drag between a cylinder far from a wall, and one in the near-field regime that we consider can easily be as much as 50%. In particular, the result of Eq. (3.8) implies that there is a gradient in the fluid friction if the body changes its distance, h, from the wall. The friction gradient is given by

$$\frac{\mathrm{d}\zeta_\perp}{\mathrm{d}h} = -\frac{\zeta_\perp^2}{4h\pi\mu}, \tag{3.9}$$

which is always negative, reflecting physically that viscous forces are increased by the presence of a solid boundary.

For a slender rod dragged through a viscous fluid with a fixed velocity, the sign of this force gradient implies that moving the rod closer to the wall will

increase the force required to maintain its speed. For an actuated filament, friction from the surrounding fluid plays a dual role. It first affects the propulsive force, as given by Eq. (3.6), through change in the drag coefficients. In addition, for either boundary- or internally-actuated filaments, the change in $\zeta_\perp$ and $\zeta_\parallel$ in Eq. (3.1) modifies the force balance, Eq. (3.2), thereby changing the shape of the flagellum, and therefore affecting the propulsion in Eq. (3.6) through a modification of $y(x,t)$. It is this interplay between viscous friction, elasticity, and activity that we propose to quantitatively analyze in this paper. As we detail below, it usually results in a non-trivial and non-monotonic relationship between wall distance and propulsive force.

3.3 Passive filaments

We first consider the case of a passive elastic filament driven at one end. In that case, the elastic energy is

$$E_{el} = \int_0^L \frac{A}{2} \left(\frac{\partial^2 y}{\partial x^2} \right)^2 dx, \tag{3.10}$$

where the linearized regime allows for the approximation of the curvature κ by the concavity of the function $y(x)$. Calculating the functional derivative of the energy in Eq. (3.10) leads to the elastic force density which, when balanced with the fluid force density, results in the linearized dynamics equation

$$\zeta_\perp \frac{\partial y}{\partial t} = -A \frac{\partial^4 y}{\partial x^4}, \tag{3.11}$$

as obtained in previous studies [56, 59]. We will consider a harmonic driving with frequency ω, and by focusing only on post-transient effects, we will assume a similar periodic dynamics for the filament.

Since the filament is driven only at one end, the boundary conditions at the tail ($x = L$) end are

$$A \frac{\partial^2 y}{\partial x^2}(L,t) = 0, \tag{3.12}$$

$$A \frac{\partial^3 y}{\partial x^3}(L,t) = 0. \tag{3.13}$$

This guarantees that the ends of the filament are force- and torque-free. At the driving position ($x = 0$), different types of physical actuation could be implemented experimentally, leading to different boundary conditions. If the tangent angle is prescribed, with the position of the filament fixed in place, the boundary conditions are

$$y(0,t) = 0, \tag{3.14}$$
$$\frac{\partial y}{\partial x}(0,t) = \epsilon \cos \omega t, \tag{3.15}$$

where $\epsilon \ll 1$ is the magnitude of the tangent angle deviation from horizontal and ω the driving frequency (pivoted case). Alternatively, for experiments that involve manipulating a passive filament via optical tweezers, the driving position would be made to oscillate harmonically under torqueless conditions, leading to the boundary conditions

$$y(0,t) = y_0 \cos \omega t, \tag{3.16}$$
$$A\frac{\partial^2 y}{\partial x^2}(0,t) = 0, \tag{3.17}$$

where y_0 is the magnitude of the oscillation in space (tweezed case). Finally, we could also consider the case where an oscillating force or torque is applied to the driving end leading to boundary conditions

$$y(0,t) = 0, \tag{3.18}$$
$$A\frac{\partial^2 y}{\partial x^2}(0,t) = M_0 \cos \omega t \ \text{(Torqued)}, \tag{3.19}$$
$$A\frac{\partial^3 y}{\partial x^3}(0,t) = F_0 \cos \omega t \ \text{(Forced)}. \tag{3.20}$$

Here M_0 and f_0 are the magnitudes of the time-varying torque and force, respectively. These boundary conditions described above are experimentally realizable, for example using micro-pipets.

Since we ignore transient effects, the steady solution for the amplitude can be written as $y(x,t) = \mathrm{Re}\{\tilde{y}(x)e^{-i\omega t}\}$. Additionally, we can define a natural length scale through the dimensionless "sperm number", $Sp = L/\ell_\omega$ where $\ell_\omega = (A/\zeta_\perp \omega)^{1/4}$; Sp is the only dimensionless number in this problem, and as such it

fully governs the filament dynamics. For $Sp \ll 1$, the penetration length ℓ_ω is much larger than the length of the filament, and thus oscillations will not decay along the length of the flagellum. For a passive filament, this is equivalent to a very rigid rod being actuated back and forth. Conversely, for $Sp \gg 1$, oscillations decay very quickly, indicating a floppy string or very viscous fluid. For an active filament, there are additional length scales that must be considered, as will be discussed later.

We nondimensionalize time by $1/\omega$ and the direction x along the filament by L, and the filament amplitude by y_0 which is specified in the tweezed case, and can be related to the forcing parameters in the other three cases. Specifically we have $y_0 = \epsilon L$ for pivoted actuation, $y_0 = F_0 L^3/A$ for forced actuation, and $y_0 = M_0 L^2/A$ for the torqued condition. By doing so, we obtain the following dimensionless equation for the amplitude $\tilde{y}$ as

$$\tilde{y}'''' - iSp^4 \tilde{y} = 0. \tag{3.21}$$

The dimensionless boundary conditions for the tail are thus given by

$$\tilde{y}''(1) = 0, \tag{3.22}$$

$$\tilde{y}'''(1) = 0, \tag{3.23}$$

while the various possible boundary actuations at the driving end are

$$\begin{aligned}
\tilde{y}(0) &= 0, \quad \tilde{y}'(0) = 1 \quad \text{(Pivoted)}, \\
\tilde{y}(0) &= 1, \quad \tilde{y}''(0) = 0 \quad \text{(Tweezed)}, \\
\tilde{y}(0) &= 0, \quad \tilde{y}'''(0) = 1 \quad \text{(Forced)}, \\
\tilde{y}(0) &= 0, \quad \tilde{y}''(0) = 1 \quad \text{(Torqued)},
\end{aligned}$$

With a solution to the amplitude equation, Eq. (3.21), we find the total force exerted on the filament by the fluid. Because we consider harmonic actuation, we only look at the time-averaged propulsive force, which is given, in a dimensional form, by

$$\langle F \rangle = \frac{1}{4} \frac{\omega \zeta_\perp y_0^2 I(Sp)}{Sp^4}, \tag{3.24}$$

where $I(Sp)$ is a dimensionless integral defined by

$$I(Sp) = Re\left[\frac{1}{2}\tilde{y}_{xx}\tilde{y}^*_{xx} - \tilde{y}_x\tilde{y}^*_{xxx}\right](x=0), \tag{3.25}$$

where an asterisk denotes the complex conjugate, and Re the real part. This expression is a direct consequence of the integral for the propulsive force, Eq. (3.6), being a total derivative when the filament is passive, and thus the function depends only on the non-dimensional amplitude $\tilde{y}$ evaluated at the endpoints [56]; the free end $x = 1$ does not contributed because of Eqs. (3.22)-(3.23).

If we then define a scaling function $Z(Sp) = I(Sp)/Sp^4$ to contain all of the dependence on Sp for the propulsive force, we have that the four cases are given by

$$\langle F\rangle = \frac{1}{4}\omega\zeta_\perp\epsilon^2L^2Z(Sp) \quad \text{(Pivoted)}, \tag{3.26}$$

$$\langle F\rangle = \frac{1}{4}\omega\zeta_\perp y_0^2Z(Sp) \quad \text{(Tweezed)}, \tag{3.27}$$

$$\langle F\rangle = \frac{1}{4}\frac{\omega\zeta_\perp F_0^2L^6}{A^2}Z(Sp) \quad \text{(Forced)}, \tag{3.28}$$

$$\langle F\rangle = \frac{1}{4}\frac{\omega\zeta_\perp M_0^2L^4}{A^2}Z(Sp) \quad \text{(Torqued)}, \tag{3.29}$$

and each of the scaling functions are unique to the four boundary conditions that solve the amplitude Eq. (3.21)

We can now examine how the propulsive force changes as the filament changes its distance h to the wall. Using the chain rule, the force gradient is given by

$$\frac{\mathrm{d}}{\mathrm{d}h}\langle F\rangle = \frac{1}{4}\omega y_0^2\left(\frac{\mathrm{d}\zeta_\perp}{\mathrm{d}h}Z + \zeta_\perp\frac{\partial Z}{\partial h}\right) \tag{3.30}$$

$$= \frac{1}{4}\omega y_0^2\left(\frac{\mathrm{d}\zeta_\perp}{\mathrm{d}h}Z + \zeta_\perp\frac{\partial Z}{\partial Sp}\frac{\partial Sp}{\partial\zeta_\perp}\frac{\mathrm{d}\zeta_\perp}{\mathrm{d}h}\right) \tag{3.31}$$

$$= \frac{1}{4}\omega y_0^2\frac{\mathrm{d}\zeta_\perp}{\mathrm{d}h}\left(Z + \frac{1}{4}Sp\frac{\partial Z}{\partial Sp}\right), \tag{3.32}$$

where we have used the definition of Sp to take a partial derivative with respect to the resistive coefficient. Since Sp is monotonic in the resistive coefficient $\zeta_\perp$, and from Eq. 3.8, we see that $\zeta_\perp$ itself is a monotonic function of h, we can examine the qualitative behavior of the force gradient by recasting the derivatives with respect

to h in terms of the dimensionless number Sp. It is important to note at this point that the variation of Sp with the distance between the flagellum and the wall is weak, with a scaling $Sp \sim [\log h/a]^{-1/4}$, and thus even large changes in the distance from the wall will produce small changes in Sp. Quantitative details are discussed in Sec. 3.4.1, and for a bull spermatozoa cell with $Sp \approx 7$ away from a boundary, bringing the cell closer to the wall will lead to a typical increase of Sp of about 10%.

The force gradient is now composed of two terms: the first is due entirely to the changing fluid friction, but the second is a more complicated effect that incorporates the elasticity of the filament through the shape change. This term reflects the fact that, in the presence of a wall, the elastohydrodynamic penetration length is a function of the distance from the wall. Changing that distance changes the essential character of viscous-induced oscillation in the filament. Due to the competition between these terms, it is now not necessarily the case that this gradient be negative, as we would expect for the case of the rigid rod. From a dimensional standpoint, we can write

$$\frac{\mathrm{d}}{\mathrm{d}h}\langle F\rangle = \frac{1}{4}\omega y_0^2 \left|\frac{\mathrm{d}\zeta_\perp}{\mathrm{d}h}\right| Z' \tag{3.33}$$

where we have therefore, since $\mathrm{d}\zeta_\perp/\mathrm{d}h$ is negative (see Eq. 3.9),

$$Z' = -\left(Z + \frac{1}{4}Sp\frac{\partial Z}{\partial Sp}\right). \tag{3.34}$$

To represent the change of the force with the wall distance, we plot in Fig. 3.3 the dimensionless force, Z (top, blue solid line) and force gradient, Z' (bottom, red dashed line) for all four different boundary conditions. Representative shapes of the filament over an entire period of oscillation are also shown for various values of Sp. For low values of Sp, the filament behaves like a rigid rod, while for larger values the decay length of the actuated filament becomes apparent. In both the pivoted and the tweezed cases, there is a maximum propulsive force (blue curve) that occurs for $Sp > 1$: $Sp \approx 4$ for the tweezed case, $Sp \approx 2$ for the pivoted case. For the torqued and forced, the maxima occur for $Sp < 1$, and as Sp approaches zero these conditions leave the linearized regime, and the model breaks down.

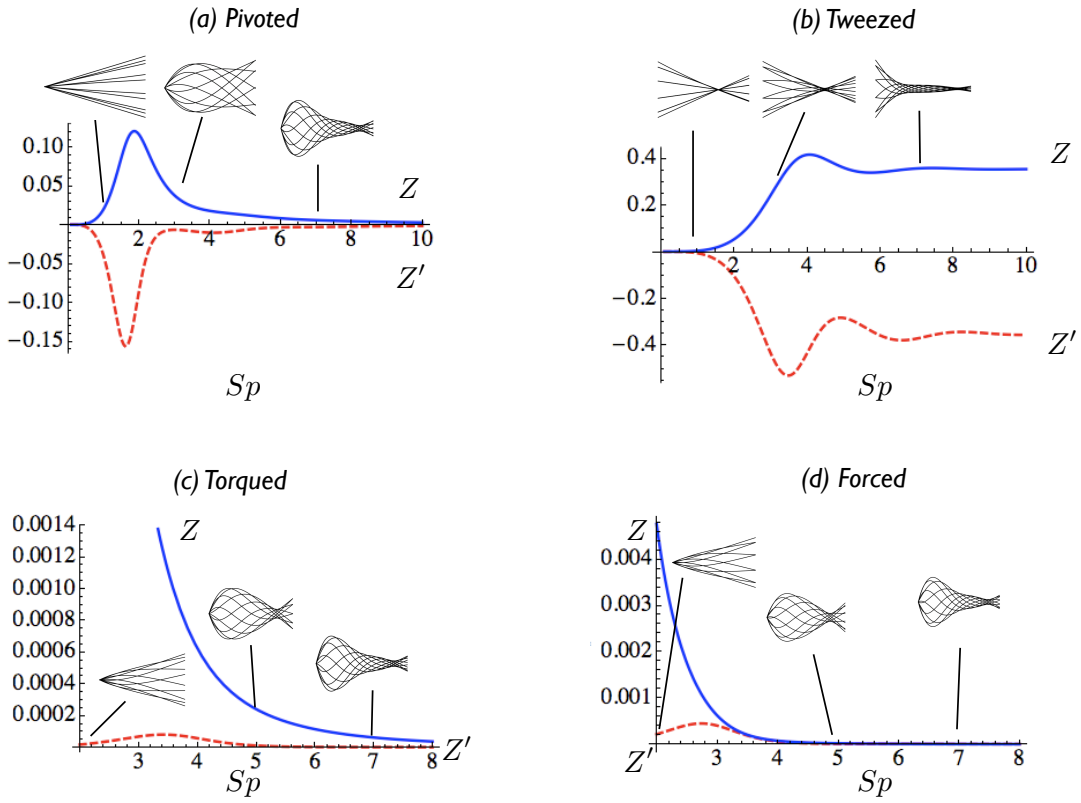

Figure 3.3: (color online) Passive filament: Normalized propulsive force, Z, (blue solid line /top curve) and propulsive force gradient, Z' (red dashed line/bottom curve) as a function of the dimensionless parameter Sp, for all four boundary conditions. Shapes of the filament for different Sp are superimposed. (a): Pivoted case; (b): Tweezed actuation; (c): Torqued condition; (d): Forced boundary condition. In the case of displacement-driven actuation, $\mathrm{d}Z/\mathrm{d}h$ is negative; since $\zeta_\perp$ is also a decreasing function of h (see Eq. 3.9), the time-average propulsive force, Eq. (3.24), is a decreasing function of h, and the presence of a boundary always increase the propulsion of the filament. On the contrary, for force-driven actuation, the sign of $\mathrm{d}Z/\mathrm{d}h$ is positive, indicating that the presence of the boundary decreases the propulsive force.

As can be seen in Fig. 3.3, Z is always positive meaning that the actuation at $x = 0$ leads to filament dynamics pushing against the fluid always in the $+x$ direction. In addition, we see that Z' is always negative for the pivoted and tweezed cases (displacement-driven actuation), indicating that the force (or Z) is a decreasing function of the distance to the wall, h. The time-average propulsive force, Eq. (3.24), generated is therefore always increased by the presence of a boundary. As such, it is somewhat similar to the increase of the drag on a body driven at a constant velocity by the presence of a boundary. Note however that Z' displays a non-monotonic dependence on Sp (and therefore on h, since Sp is a monotonically decreasing function of h), which is due entirely to the change in the filament shape accompanying the change in height. In contrast, in the torqued and forced cases (force-driven actuation), we see that Z' is positive, indicating that the opposite is true, and the propulsive force is now decreased by the presence of the wall. These result are reminiscent of early work showing a similar contrast between two-dimensional swimming with fixed kinematics or fixed hydrodynamic power [51, 52, 53, 54].

3.4 Active flagella

We now turn to the case of an active filament as a model for a eukaryotic flagellum, and investigate how the changes in hydrodynamic drag induced by the wall and the response of the flagellar amplitude couples to the internal activity. As before, we examine force balance, but for an active flagellum we retain the internal forcing term, and the linearized dynamics equation becomes [63, 62, 68]

$$\zeta_\perp \frac{\partial y}{\partial t} = -A\frac{\partial^4 y}{\partial x^4} + a\frac{\partial f}{\partial x}. \tag{3.35}$$

Since the total force and moment on the filament must vanish, this imposes boundary conditions on the distal, or "tail", end as

$$-A\frac{\partial^3 y}{\partial x^3}(L,t) + af(L) = 0, \tag{3.36}$$

$$-A\frac{\partial^2 y}{\partial x^2}(L,t) = 0. \tag{3.37}$$

Regarding the other side of the flagellum (its "head" side), we will examine two different types of boundary conditions, either clamped or hinged. For a clamped filament, physically corresponding to a cell that is immobilized via micropipet, both the head and its tangent angle cannot change, and the boundary conditions are thus

$$y(0,t) = 0, \tag{3.38}$$

$$\frac{\partial y}{\partial x}(0,t) = 0. \tag{3.39}$$

In the hinged case, the head remains fixed, but the tangent angle can move torquelessly. This is the situation that would take place in the presence of an optical trap, so the boundary conditions become

$$y(0,t) = 0, \tag{3.40}$$

$$A\frac{\partial^2 y}{\partial x^2}(0,t) + a\int_0^L f(x)dx = 0. \tag{3.41}$$

If we non-dimensionalize x by L and time by $1/\omega$ as in the previous section, but additionally scale the magnitude of the flagellar beat y_0 by af_0L^3/A, where f_0 is the magnitude of the internal force, then the equation for mechanical equilibrium becomes

$$\tilde{y}'''' - iSp^4\tilde{y} = \frac{\partial \tilde{f}}{\partial x}. \tag{3.42}$$

The dimensionless version of the boundary conditions are

$$-\tilde{y}'''(1) + \tilde{f}(1) = 0, \tag{3.43}$$

$$\tilde{y}''(1) = 0, \tag{3.44}$$

for the tail end, and $\tilde{y}(0) = 0$ and one of the following for the head

$$\tilde{y}'(0) = 0 \text{ (Clamped)}, \tag{3.45}$$

$$\tilde{y}''(0) + \int_0^1 \tilde{f}(x)dx = 0 \text{ (Hinged)}. \tag{3.46}$$

In order to consider the response of the flagellum due to changing the distance from a wall, and thus changing the friction of the fluid, the mechanism of the axoneme itself must be taken into account, *i.e.*, a model for f must be prescribed. We proceed in the next two sections by considering two such models.

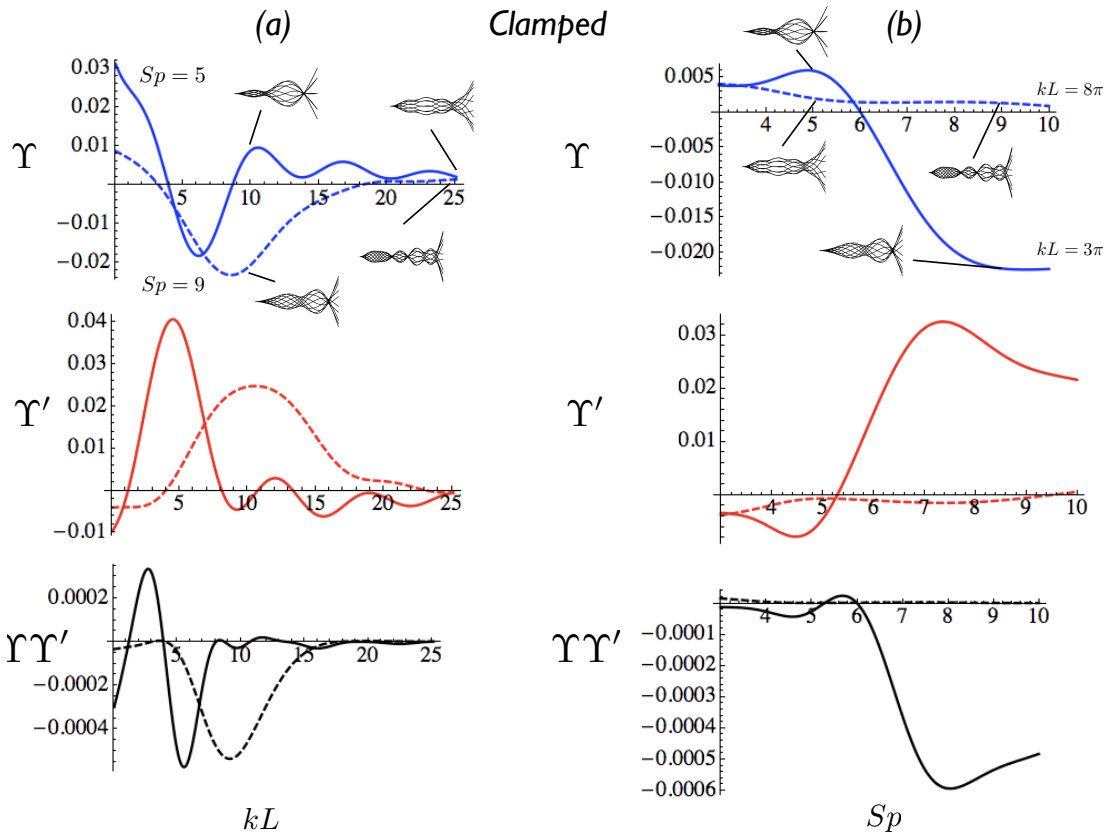

Figure 3.4: (color online) Active filament with prescribed activity and clamped boundary conditions: dimensionless force, Υ, force gradient, Υ', and gradient of the square of the norm of the force, $\Upsilon\Upsilon'$, for various values of (Sp, kL). The corresponding shapes are displayed at their representative values on the curves. (a) Υ (blue, top), Υ' (red, middle) and $\Upsilon\Upsilon'$ (bottom, black) as a function of kL for $Sp = 5$ (solid) and 9 (dashed); kL runs from 0.1 to 8π (b) All three again as a function of Sp for $kL = 3\pi$ (solid) and $kL = 8\pi$ (dashed); Sp varies from 3 to 10. The axis limits were chosen to cover a wide range of biologically relevant filaments and viscosity solutions, keeping in mind that for small Sp the rigid rod limit renders the model inaccurate and is irrelevant for biological locomotion.

3.4.1 Prescribed activity

In the first approach, we consider that the active force per unit length takes the form of a prescribed traveling wave, i.e. $f(x,t) = \mathrm{Re}\{f_0 e^{ikx - i\omega t}\}$ [62], whose frequency (ω) and wavenumber (k) are not modified by the presence of a boundary. This enables us to completely specify the filament shape, its propulsive force, and the propulsive force gradient, with two dimensionless numbers: Sp and kL. The

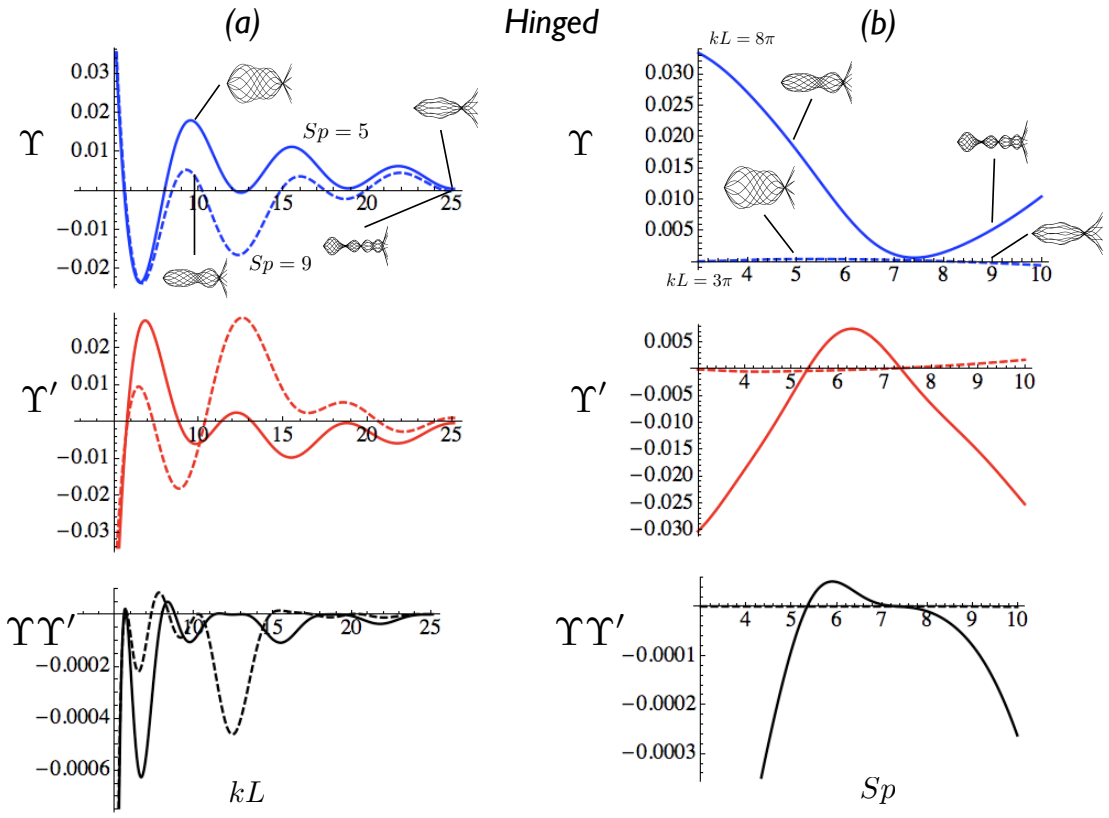

Figure 3.5: (color online) Active filament with prescribed activity and hinged boundary conditions: Dimensionless force, Υ, force gradient, Υ', and gradient of the norm squared of the force, $\Upsilon\Upsilon'$, for various values of (Sp, kL). The corresponding shapes are displayed at their representative values on the curves. (a) Υ (blue, top), Υ' (red, middle) and $\Upsilon\Upsilon'$ (bottom, black) as a function of kL for $Sp = 5$ (solid) and 9 (dashed); kL varies from 0.1 to 8π (b) All three again as a function of Sp for $kL = 3\pi$ (solid) and $kL = 8\pi$ (dashed); here Sp runs from 3 to 10.

dimensionless equation of mechanical equilibrium is now written as

$$\tilde{y}'''' - iSp^4\tilde{y} = ikLe^{ikLx}, \tag{3.47}$$

with boundary conditions

$$\begin{aligned} \tilde{y}(0) &= 0, & (3.48)\\ \tilde{y}'''(1) &= e^{ikL}, & (3.49)\\ \tilde{y}''(1) &= 0, & (3.50) \end{aligned}$$

and either of the following

$$\begin{aligned} \tilde{y}'(0) &= 0 \quad \text{(Clamped)}, & (3.51)\\ \tilde{y}''(0) &= -\frac{(1-e^{ikL})}{ikL} \quad \text{(Hinged)}. & (3.52) \end{aligned}$$

It is then straightforward to calculate the propulsive force on the fluid due to the active filament, which is given by

$$\langle F \rangle = \frac{1}{4}\omega\zeta_\perp y_0^2 \Upsilon(Sp, kL), \tag{3.53}$$

where the scaling function $\Upsilon(Sp, kL)$ is defined as the dimensionless integral

$$\Upsilon(Sp, kL) = Im\left[\int_0^1 \tilde{y}^* \frac{\partial \tilde{y}}{\partial x} dx\right]. \tag{3.54}$$

Here Im denotes the imaginary part. Note that the amplitude of the flagellar beat is proportional to the magnitude of the active force, and thus the propulsive force scales quadratically with it. This dependence has been scaled out of the propulsive force, and is assumed to remain constant.

As in the previous section, the force gradient can be calculated using the chain rule and we get

$$\begin{aligned} \frac{d}{dh}\langle F \rangle &= \frac{1}{4}\omega y_0^2 \left(\frac{\mathrm{d}\zeta_\perp}{\mathrm{d}h}\Upsilon + \zeta_\perp \frac{\mathrm{d}\Upsilon}{\mathrm{d}h}\right) & (3.55)\\ &= \frac{1}{4}\omega y_0^2 \frac{\mathrm{d}\zeta_\perp}{\mathrm{d}h}\left(\Upsilon + \frac{1}{4}Sp\frac{\partial \Upsilon}{\partial Sp}\right). & (3.56) \end{aligned}$$

The main difference between Eq. (3.56) and Eq. (3.32) is that the scaling function Υ is a function of both the elastohydrodynamic length scale parameterized by Sp

and an active length scale defined by kL; the interaction of these two lengths leads to several non-intuitive results, as shown below. From a dimensional standpoint, we can write

$$\frac{d}{dh}\langle F\rangle = \frac{1}{4}\omega y_0^2 \left|\frac{\mathrm{d}\zeta_\perp}{\mathrm{d}h}\right| \Upsilon' \tag{3.57}$$

where, as above, we have defined the dimensionless force gradient as

$$\Upsilon' = -\left(\Upsilon + \frac{1}{4}Sp\frac{\partial \Upsilon}{\partial Sp}\right). \tag{3.58}$$

Anticipating that the mean force, $\langle F\rangle$, can change sign, we compute the gradient in the norm squared of the force and get

$$\frac{d}{dh}\left[\frac{1}{2}\langle F\rangle^2\right] = \frac{1}{16}\omega^2 y_0^4 \left|\frac{\mathrm{d}\zeta_\perp}{\mathrm{d}h}\right| \zeta_\perp \Upsilon\Upsilon', \tag{3.59}$$

so that $\Upsilon\Upsilon'$ is the dimensionless gradient in the norm (squared) of the propulsive force.

In Fig. 3.4a we display Υ (top, blue), Υ' (middle, red) and $\Upsilon\Upsilon'$ (bottom, black) for $Sp = 5$ (solid line) and $Sp = 9$ (dashed line) as a function of kL in the case of clamped boundary conditions. In Fig. 3.4b we show the same system, only this time several representative values of kL are chosen and the resulting dimensionless force and force gradients are plotted as a function of Sp. Similar results are shown in Fig. 3.5 in the case of hinged boundary conditions.

First, we observe that although the activity wave is always traveling from the body of the cell to the tip of the active filament ($\omega/k = c > 0$), the propulsive force can change sign: $\Upsilon > 0$ means a force on the fluid in the same direction as the wave, and therefore (if the cell was free to move) swimming in the direction opposite to the wave. As a difference, $\Upsilon < 0$ means the generation of a force on the fluid opposite to the wave propagation, and therefore swimming along the direction of the wave propagation. Recall that in the passive case analyzed in the previous section, we always had a positive force. We also observe here, in general, a non-monotonic variation of the propulsive force with both the activity wavelength (through kL) and frequency (through Sp). We further note the importance of the boundary conditions as markedly different results are obtained in Fig. 3.4 and Fig. 3.5.

The second important results to note from Figs. 3.4 and 3.5 are the variations in the sign of the force gradient. In all cases where the product $\Upsilon\Upsilon' > 0$, the presence of the boundary causes the magnitude of the propulsive force to decrease. The opposite is true in all cases where $\Upsilon\Upsilon' < 0$. It should be obvious from Figs. 3.4 and 3.5 that the sign of the force gradient displays a complex dependence on the parameters (Sp, kL), as well as on the type of boundary conditions considered.

To demonstrate the physical significance of our results, we consider as an example the case of a bull spermatozoa. For such a cell, we have $L \approx 60$ μm, $A \approx 10^{-21}$ Nm^2, $\omega \approx 10$ Hz and the "bare" resistive coefficient $(\zeta_\perp)_\infty \approx 10^{-3}$ Ns/m^2 far from the wall, leading to $Sp_\infty \approx 7$ [36]. As discussed above, the wall increases fluid drag, and thus it increases the value of Sp. Since is possible to change the drag coefficient by as much as 50%, and since $Sp \sim \zeta^{1/4}$, the change in the value of Sp can be as high as about 10%. The active length scale kL is more difficult to estimate, because the prescribed activity is not immediately obvious through direct observation of the flagellar beat, but reasonable estimates give kL between 3π and 5π [71, 62]. In the context of the prescribed activity model studied here, kL is assumed to not change with distance from the wall.

We show in Fig. 3.6 contour plots of the gradient of the norm of the propulsive force, $\Upsilon\Upsilon'$, as a function of both Sp and kL (left: clamped conditions; right: hinged conditions). The force gradient is positive in the filled contour regions; contour lines are 5×10^{-3} in dimensionless units of force square per unit length. Any given point in the (Sp,kL) plane gives a particular value of the dimensionless force gradient. By bringing the beating flagella closer to the wall, the sperm number is progressively increased, and the value of the new force gradient is found by gradually moving along horizontal lines in Fig. 3.6 (which are lines of constant kL). We show in Fig. 3.6 arrows corresponding to this gradual increase starting at $Sp = 7$ and for $kL = 3\pi$, 5π and 7π.

First we observe, again, that the nature of the boundary condition strongly affects the sign of the force gradient, and experiments performed using optical trapping should give different results from experiments employing micropipettes. Second, we see that three distinct cases are possible depending on the domain

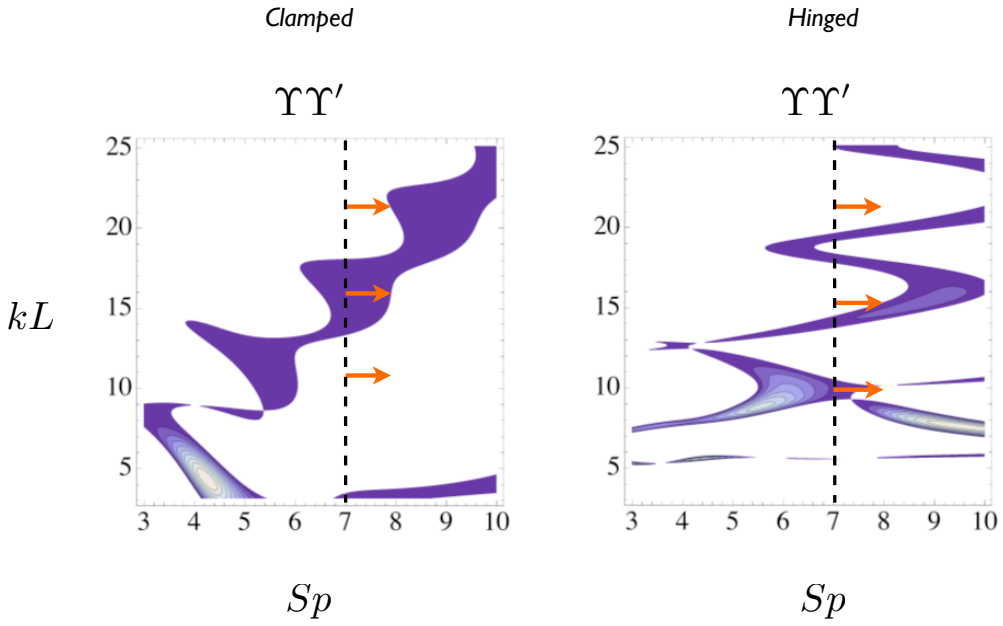

Figure 3.6: (color online) Contour plots for the dimensionless propulsive thrust gradient, $\Upsilon\Upsilon'$, as a function of Sp and kL. Left: clamped boundary conditions (micro-pipette); right: hinged conditions (optical trap). The force gradient is positive in the filled contour regions; contour lines are 5×10^{-3} in dimensionless units of force square per unit length. The arrows indicate the increase in the value of Sp taking place as a beating cell is gradually approached to a solid boundary, starting at $Sp = 7$ and for $kL = 3\pi$, 5π and 7π.

crossed by one of the arrows in Fig. 3.6. In the first case, the cell away from the wall is in a region where $\Upsilon\Upsilon'$ is negative (white domains in Fig. 3.6) and remains in it during the increase of Sp; in that case, a measurement would lead to a monotonic increase of the propulsive force as the flagellum comes closer to the boundary. A second case is the one for which $\Upsilon\Upsilon'$ is always positive (for example the middle arrow in the left figure, which remains located inside the positive contour plots), in which case the force would be measured to be monotonically decreased by the presence of boundaries. Finally, a third situation can arise where the arrow crosses the boundary between a region of positive (resp. negative) gradient and a region of negative (resp. positive) gradient, leading to a surprising non-monotonic variation of the propulsive force with the flagellum-wall distance.

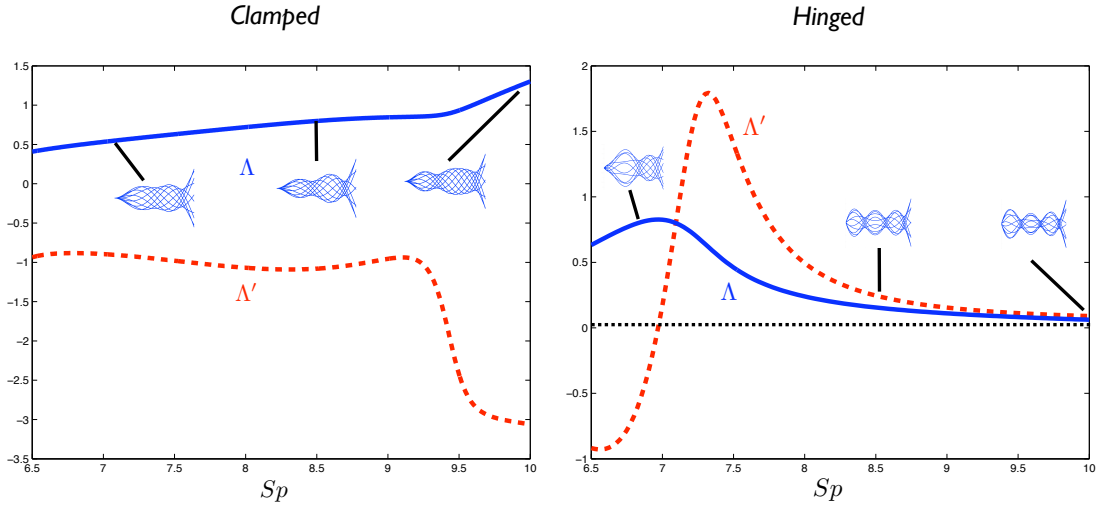

Figure 3.7: (color online) Dimensionless force (Λ, blue line) and force gradient (Λ', red dashed line) for the linear response model with clamped (left) and hinged (right) boundary conditions, as a function of Sp. Characteristic flagellar beat patterns are also shown at several values of Sp.

3.4.2 Self-organized axonemal beating

The prescribed activity model studied in the previous section assumes that the internal activity of the flagellum is not modified by the change in the fluid friction near a wall. In a more physically realistic model, the oscillations of the flagellum would arise from a self-organized motion of the molecular motors, and thus the internal force generation would in turn be a function of the force distribution on the filament (both bending and fluid drag).

We consider in this section such a model as first introduced by Camalet and Julicher [63]. In this framework, the active force is described by a linear response to the filament sliding, $f = \chi\Delta$. Spontaneous oscillations of flagellum then arise as a self-organized phenomenon for specific values (eigenvalues) of the response function χ. If we use Eq. (3.35) with the linear response relationship $f = \chi\Delta \approx a\chi\partial y/\partial x$, then we obtain the following dimensionless eigenvalue equation for the filament amplitude

$$\tilde{y}'''' - \bar{\chi}\tilde{y}'' + iSp^4\tilde{y} = 0, \tag{3.60}$$

where $\bar{\chi} = aL^2\chi/A$.

The amplitude can be solved as $\tilde{y} = \sum_{i=1}^{4} A_i e^{q_i s}$, where the q_i are the four solutions to the characteristic equation corresponding to the characteristic modes of Eq. (3.60). For a given value of Sp, we note that there is an infinite number of discrete eigenvalues χ_n; as in previous work, we will consider only the eigenvalue with lowest norm as they correspond to the lowest degree of motor activity. Non-trivial solutions to Eq. (3.60) exist only for certain critical pairs of parameters (Sp_c, χ_c), set by the boundary conditions [63, 68]

$$\sum_{i=1}^{4} M_{ij} A_j = 0, \tag{3.61}$$

where the matrix $\mathbf{M}$ is defined by the boundary conditions (clamped or hinged, same as in the previous section). Since the solution, $\tilde{y}$, is an eigenfunction for a linear equation, it is known only up to a multiplicative constant, and the absolute magnitude for the oscillations can therefore not be obtained. Away from a wall, it has been shown theoretically and experimentally that the beating amplitude depends only weakly on nonlinear corrections [68, 67], so we will proceed by writing the (arbitrary) amplitude of the filament oscillations as y_0, which we assume is the magnitude of the first component of the eigenvector (i.e. $A_1 = y_0$), and is assumed to remain constant.

The propulsive force acting from the flagellum on the fluid in this case is given by

$$\langle F \rangle = \frac{1}{4} \omega \zeta_\perp y_0^2 \Lambda(Sp), \tag{3.62}$$

where

$$\Lambda(Sp) = Im \left[\int_0^1 \tilde{y}^* \frac{\partial \tilde{y}}{\partial x} dx \right] \cdot \tag{3.63}$$

and which can be written more explicitly as

$$\Lambda(Sp) = Im \left[\int_0^1 \sum_{i=1}^{4} A_i^* e^{q_i^* x} \sum_{j=1}^{4} A_j q_j e^{q_j x} dx \right], \tag{3.64}$$

In Eq. (3.64), the A_i's and q_i's are all implicit functions of the response χ, which is in turn a function of Sp. These functions are all known, albeit verbose, and thus allow us to explicitly write the force in terms of Sp.

Near a wall, the fluid friction modifies the fluid resistance coefficient, $\zeta_\perp$, but the bending modulus A remains constant. In order to elucidate the variation of the propulsive force with a change of flagellum-wall distance, we thus need to know how both the beat frequency, ω, and the response function, χ, vary. Without further biological information about the behavior of molecular motors under changing load, we now have to make modeling assumptions.

The functional dependence of the response function χ, on the oscillation frequency and other materiel parameters is, in general, unknown. In order to satisfactorily solve Eq. (3.60) we need to find the complex eigenvalues that allow for non-trivial solutions of the equation to exist. To fully model the active system, the filament response function should be derived from a model for the molecular motors, and without such an explicit model, χ could very generally be a function of on Sp, ATP production and concentration (i.e. activity level), load distribution, structural inhomogeneities, and any other parameter(s) that govern activity in the axoneme. The most general solution would thus require a detailed model of the molecular motors (see e.g. [63, 68, 67]).

Since our primary focus in this paper is to explore the hydrodynamic consequences of activity, boundaries, and elasticity, we will make below several modeling assumptions in order to examine extreme cases, by essentially specifying the functional dependence of χ. In general both the frequency ω and the response function χ will vary, but we are going to assume here that one of them remains essentially constant as the wall-flagellum distance is varied. We thus assume that one parameter shows a strong variation with h whereas the other depend only weakly on h.

In the first case, the linear response function remains constant, such that the only way for the eigensolution to Eq. (3.60) to have non-trivial values requires the oscillation frequency, ω, to change in such a manner that Sp remains constant. Given the definition of Sp, this means that one would observe experimentally a frequency change given by $\omega(h)/\omega(h=\infty) = \zeta_\perp(h=\infty)/\zeta_\perp(h)$, but no waveform variation. In that case, the only change in the propulsive force, Eq. (3.62), would arise from the variation of $\zeta_\perp$ with h, and therefore one would experimentally

measure a increase of the magnitude of the force near boundaries.

The second case, more complex, is one in which the frequency of oscillation of the filament would remain fixed. Although there is no experimental evidence that demonstrates that ω does remain constant as the distance between the cell and the boundary is changing, it is a reasonable assumption to make in the absence of this information. This assumption, however, puts a stringent constraint on the response function χ; in order to provide non-trivial solutions to Eq. (3.60) the response function must be only a function of Sp in such a fashion as to match the eigenvalues exactly. In this case, varying the distance between the flagellum and the wall, h, modifies the value of Sp. As a result of changes in Sp, both the response function χ, and the eigenfunction, will be continuously modified, which will produce a non-trivial variation in the propulsive force. As in the previous section, we will write the force gradient formally as

$$\frac{\mathrm{d}}{\mathrm{d}h}\langle F\rangle = \frac{1}{4}\omega y_0^2 \left|\frac{\mathrm{d}\zeta_\perp}{\mathrm{d}h}\right| \Lambda'. \tag{3.65}$$

For this scenario, we plot in Fig. 3.7 the dimensionless propulsive force (Λ) and force gradient (Λ') for the clamped and hinged boundary conditions respectively, as well as several exemplary beat patterns. With this modeling approach, we see that Λ is always positive. Using the notation of Fig. 4.4, the flagellum is therefore always pushing the fluid along the x direction, and is thus expected to swim in the $-x$ direction. Furthermore, we obtain that the sign the force gradient depends on the nature of the boundary conditions. In the clamped case, we get that Λ' is always negative, and therefore the presence of boundaries systematically increases the propulsive force. In contrast, in the hinged case, the function Λ' is seen to be negative for Sp below 7, and positive otherwise. In that case, and similarly to what was reported experimentally using optical trapping in Ref. [55], the measurements would show a decrease of the propulsive force near boundaries.

3.5 Discussion

Biological cells do not swim in a vacuum; the environment itself is what makes swimming possible, and thus we must consider characteristics of the sur-

roundings that may modify motility behavior. Since flagellated organisms generate propulsion by actuating an elastic filament to do work against their viscous environment, the specific response of that environment can be crucial to understanding the overall locomotion characteristics. The particular environmental effect that we have studied in this paper is the modification of fluid drag by the presence of a no-slip boundary, and the balance between the deformable waveform of the flagellum and the viscous fluid forces that generate propulsive thrust.

For driven filaments, we have shown that fluid drag plays a dual role: not only does it change the propulsion generated by a given filament waveform, but it also affects the waveform itself expressed by the beating filaments. For passively actuated filaments, the resulting wall effect is a systematic increase of the propulsive force that the beating filament imparts on the surrounding fluid in the case of displacement-driven actuation, while a decrease is obtained in the case of force-driven actuation. In contrast, for active filaments as models for eukaryotic flagella, the modification to the propulsive force depends sensitively on a combination of the flagellar material properties, the boundary condition applied to the flagellum, and the manner in which the molecular motors organize to cause oscillation; different values of parameters can increase, decrease or even display non-monotonic influence on the cellular propulsive force.

Using simple scaling arguments, let us finally estimate the expected size of the propulsive force change induced by a wall on an active flagella . Let us compare the order of magnitude for the force far away from the boundary to the average change in force between near- and far-field. Far from the wall the propulsive force scales as $F_\infty \sim \omega y_0^2 (\zeta_\perp)_\infty \Upsilon$. Since our calculation for the force change due to a wall focuses on the near field, we can estimate the average change in force as $\Delta F \sim L \times dF/dh$ as L, the cell length, gives approximately the spatial range over which the near-field matches with the far-field. Using the estimate $dF/dh \sim -\omega y_0^2 (\mathrm{d}\zeta_\perp/\mathrm{d}h)\Upsilon'$ we therefore get

$$\frac{\Delta F}{F_\infty} \sim -\frac{L(\mathrm{d}\zeta_\perp/\mathrm{d}h)\Upsilon'}{(\zeta_\perp)_\infty \Upsilon}. \tag{3.66}$$

According to Eq. (3.9), we have $\mathrm{d}\zeta_\perp/\mathrm{d}h \sim -\zeta_\perp^2/h\mu$ hence the scaling becomes

$$\frac{\Delta F}{F_\infty} \sim \frac{L\zeta_\perp^2}{h\mu(\zeta_\perp)_\infty}\left(\frac{\Upsilon'}{\Upsilon}\right). \tag{3.67}$$

Since we know that $(\zeta_\perp)_\infty \approx \mu/\ln(2L/a)$ and $\zeta_\perp \sim \mu/\ln(2h/a)$, we get the final scaling relationship

$$\frac{\Delta F}{F_\infty} \sim \frac{\ln(2L/a)}{[\ln(2h/a)]^2}\left(\frac{\Upsilon'}{\Upsilon}\right)\frac{L}{h}. \tag{3.68}$$

From the results obtained above, we observe that $\Upsilon'/\Upsilon \sim \pm 1$. For human spermatozoa, the parameters are $L \approx 40$ μm, $a \approx 0.20$ μm. In the experiment of Ref. [55] the near-field measurements get as close as $h = 5$ μm which leads to $\Delta F/F_\infty \sim \pm 1$. This simple order-of-magnitude calculation shows that the force could be expected to be changed by order one by the introduction of a boundary. In the experiment conducted in Ref. [55] the force was measured to be reduced by a factor of three, which is consistent with this simple estimate.

Acknowledgments

We thank Michael Berns and Linda Shi for useful discussions, and for the collaboration which planted the seeds for this theoretical investigation. Funding by the National Science Foundation (grant CBET-0746285 to EL) is gratefully acknowledged. This chapter is reproduced in it's entirety from A. A. Evans and E. Lauga, *Phys. Rev. E.*, **82**, 041915, 2010.

Chapter 4

Membrane locomotion

4.1 Introduction

In the previous two chapters we explored the ramifications of elasticity, activity, and interactions (both of the potential and dissipative variety) for thin flexible filaments. To broaden our approach we now consider two dimensional surfaces; specifically, we examine the fluid-elasticity coupling between membranes immersed in a viscous environment, and study the transduction of deformation into macroscopic fluid pumping.

Modeling viscous locomotion, and the dual problem of pumping, are generally approached in one of two ways: the first simplifies the geometry of the problem while retaining full fluid interactions, while the second retains more complicated geometric nonlinearities but simplifies the non-locality of Stokes flow.

We present here a natural extension of this modeling by considering active processes in flexible membranes. We explore two different ways to model the interaction of an elastic membrane with an external fluid: we will prescribe an internal activity and then solve the fluid mechanics precisely using linear response in order to find the pumping of fluid caused by this activity, and we will prescribe the kinematics of deformation according to an energy minimization model in order to calculate propulsion for a more complex geometry. The former method allows analytical calculations to be performed, thus elucidating the fundamental scalings involved with relating an internal stress state to a macroscopic flow velocity, while the latter solves the fully nonlinear shape equations and fluid mechanics using a robust numerical method.

As before, in considering elasticity of filaments and rods, we now use an example of a soft material that occurs readily in biological systems: the lipid bilayer membrane. Many of the properties of this particular material are easily generalizable to non-bilayer surfaces, but the ubiquity with which the lipid bilayer appears in biology makes it a tempting target for our analysis.

The preeminence of viscous dissipation over inertial effects at low Reynolds numbers leads to many interesting consequences for life and engineering efforts at the micron-scale. In particular, swimming at zero Reynolds number is impossible using time-reversible motions, a result known as the Scallop theorem [72].

As a result, at least two actuation degrees of freedom are necessary to generate locomotion. The breaking of this time-reversal symmetry has been studied both from a mathematical point of view, and in the context of modeling real organisms [36, 73, 74, 62, 10]. Unlike in high Reynolds number flows, such as those relevant in describing the swimming of fish and flying of birds, fluid motion at low Reynolds numbers is set almost instantaneously by the time-dependent geometries of the immersed bodies. Thus it is natural to inquire about the shapes of immersed (and possibly fluctuating) cell membranes, and their relationships to locomotion.

Membranes composed of lipid bilayers are ubiquitous in nature, and the study of bilayer vesicles as a model system for biological cells has yielded significant insight into their behavior [75, 76]. In addition to the biological relevance of lipid bilayer vesicles, or liposomes, advances in self-assembly have paved the way for other types of vesicles to be developed experimentally [77, 78]. Vesicles assembled from block copolymers [79], liquid crystal amphiphiles [80], and membranes with embedded proteins or anchored polymers [81, 82, 83, 84, 85] all have tunable material properties which can be manipulated with unprecedented control [86, 87]. It is also well known that many biological cells actively modify or maintain the shapes of their membranes [88, 89], either for developmental [90] or locomotive processes [91, 92].

Recently, synthetic microswimmers inspired by the locomotion of eukaryotic cells have been successfully designed in experiments [93], exploiting the planar beating of a flagellum-like organelle. Beyond biomimetic engineering, other small-scale synthetic swimmers or swimming strategies have also been proposed, both theoretically and experimentally [72, 94, 95, 96, 97, 98, 99, 10, 100]. One recently-studied example is a self-propelled colloidal particle which exploits asymmetrically-distributed chemical reactions to swim in a viscous fluid [101, 102].

Active materials, ranging from living fluids to lipid membranes interspersed with force generating molecular machines, present interesting challenges for modern soft matter physicists [103]. Understanding the dynamics of materials whose characteristics and responses depend on dynamically varying internal stresses is not only intellectually stimulating but also holds promise for revealing meaningful

features of the cellular world. Mechanical feedback between the environment that a cell is immersed in and the fluctuating inner behavior of its internal constituents plays an important role in motility, morphology, and reproduction [104, 88, 92, 91]. The study of biological membranes, in particular, and the role of morphology in ultimately determining the functionality of a cell, has long generated interested in the scientific community. The geometry of a cell impacts the proteins embedded in its surface [90], and the shape fluctuations of an active membrane yields insight about the activity within [87, 105, 106, 89].

In recent decades cell locomotion has occupied a great deal of attention from the scientific community [72, 10, 9, 35]. One of the possible justifications for this interest stems from the fact that self-propelled organisms represent one of the ways in which soft active transport is accessible to our intuition. In all of these cases, and in many others, shape matters. The deformation of a biological membrane, and the rate at which it occurs, inevitably determines the effect that the internal stress state has on the world around it: Internal activity competes with dissipative forces arising from viscous fluids, frictional substrates, or other external forces and – in addition to the particular constitutive relationship ruling the behavior of the membrane itself – the final result is the shape of the body.

Focusing on cellular motility, and swimming in particular, the only external stress is that exerted by the viscous fluid on the deforming surface. Provided that the deformation of the membrane is not time-reversible, the body performs work against the fluid and generates a macroscopic velocity [72]. Dual to this problem is fluid pumping, wherein an actively deforming tethered membrane transports fluid, rather than propelling itself through the bulk. This aspect of fluid transport is the focus of the current paper.

To understand the origin of fluid transport by a beating membrane, one only needs to know the deformation of the surface and the fluid properties; this is, in fact, how previous work on the subject has been developed, either to model actual organisms or to provide concepts for locomotion that do not occur in Nature [107, 10, 108, 109, 110]. If the kinematics of a membrane deformation are prescribed, the transport characteristics require thus only solving the fluid mechanics problem

[107].

A more physically-relevant model would start from knowledge of the internal forcing, and then both the deformation and the transport would be solved for at the same time. Recently there have been attempts to prescribe not merely the kinematics, but instead the internal dynamics of a deforming body as model for the physics of axonemal beating in eukaryotic cells [63, 62]. The physical problem becomes then: given an internal state, and a dynamic evolution equation, what are the macroscopic results? Currently this work has covered only active filaments; our present endeavor extends this dynamical analysis to membranes. Bridging the gap between transport properties and an internal stress condition is a vital first step towards synthesizing a comprehensive description of active pumping or locomotion.

In this manuscript we present a model for the internal force generation in an active membrane. Introducing two models for internal actuation, and taking advantage of the asymptotic limit of small forcing, we analytically derive the membrane deformation from its linear response, and then use the deformation to deduce the (quadratic) fluid transport. Our results are recovered by scaling arguments, which allow us to intuitively quantify how the three-way balance between internal forcing, passive (elastic) constitutive modeling and external viscous forcing impact fluid transport.

4.2 Transport by general deformation of a sheet

4.2.1 Setup

For the microscopic regimes that we are interested in the fluid flow is well modeled by the incompressible Stokes equations, $\nabla p = \mu \nabla^2 \mathbf{u}$, $\nabla \cdot \mathbf{u} = 0$, where $\mathbf{u}$ is the fluid velocity, p the pressure and μ the shear viscosity. We consider an infinite, two-dimensional sheet that passes a traveling wave of arbitrary shape h over its surface (see Fig. 4.4 for notation). If there is no variation in the y-direction then the fluid is two-dimensional and a streamfunction ψ such that $\mathbf{u} = \psi_z \hat{x} - \psi_x \hat{z}$ can be defined.

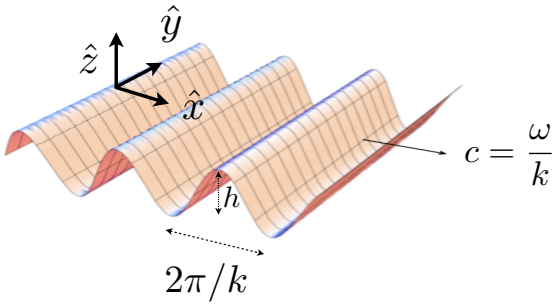

Figure 4.1: Generalized Taylor swimming sheet passing a traveling wave in the positive x direction with constant wave speed $c = \omega/k$. The wavelength is $2\pi/k$ and the height of the membrane denoted $h(kx - \omega t)$. In the reference frame of the sheet, the material points undergo transverse displacements, while at infinity a uniform pumping flow U develops.

For an arbitrarily shaped traveling waveform $h(kx-\omega t)$, we apply a no-slip boundary condition to the sheet to get

$$u_x = \frac{\partial \psi}{\partial z}|_S = 0, \tag{4.1a}$$

$$u_z = -\frac{\partial \psi}{\partial x}|_S = -\frac{\partial h}{\partial t}, \tag{4.1b}$$

where these conditions must be applied on the material itself, S. This is precisely what leads to geometric nonlinearities and precludes a fully general analysis of the present problem.

4.2.2 Fluid pumping

We expand the waveform as $h = \epsilon h^{(1)} + \epsilon^2 h^{(2)} + ...$ where ϵ is a small parameter denoting the magnitude of the wave amplitude. The stream function ψ is expanded similarly.

To leading order, we write $h^{(1)} = \mathrm{Re}\{\sum b_n e^{in(kx-\omega t)}\}$ and, following Childress [47], solve for the stream function to obtain

$$\psi^{(1)} = \mathrm{Re}\{\sum_n \frac{\omega}{k} b_n (1 + nkz) e^{-nkz} e^{in(kx-\omega t)}\}. \tag{4.2}$$

At this order there can thus be no flow far from the sheet: the $h \to -h$ symmetry demands that any expansion of the velocity U be symmetric in powers of h.

At second order, then, we find that

$$\psi_z^{(2)}(x,0) = -\psi_{zz}^{(1)}(x,0)\mathrm{Re}\left\{\sum_n inkb_n e^{in(kx-\omega t)}\right\}. \tag{4.3}$$

Since the sheet is periodic, averaging this quantity over one period in space yields the flow at infinity, or the macroscopic fluid transport velocity, and we obtain

$$U^{(2)} = \frac{1}{2}\sum_n \omega k|nb_n|^2. \tag{4.4}$$

Importantly, we see that the knowledge of only the first order height coefficients, b_n, leads to the determination of the transport properties at second order.

4.2.3 Stress

In the following section we will invoke local force balance at leading order to determine the membrane shape and thus we need to know the distribution of stress from the fluid. The pressure at first order is given by

$$p^{(1)} = -2\mu\omega\mathrm{Re}\{\sum_n inkb_n e^{-nkz}e^{in(kx-\omega t)}\}, \tag{4.5}$$

while the components of the fluid stress are

$$\sigma_{zz}^{(1)} = -p^{(1)} + 2\mu\frac{\partial^2\psi^{(1)}}{\partial x\partial z}, \tag{4.6a}$$

$$\sigma_{xz}^{(1)} = 2\mu\left(\frac{\partial^2\psi^{(1)}}{\partial x^2} - \frac{\partial^2\psi^{(1)}}{\partial z^2}\right). \tag{4.6b}$$

4.3 Active membrane mechanics

We now proceed to derive the dispersion relations for two models of active elastic sheets that will provide a quantitative bridge between the microscopic formulation and the macroscopic flow.

In general the internal forces (i.e. the forces not originating with the viscous fluid) will consist of a passive elastic response and an active component. The general enthalpy functional that describes the internal energetic state of the membrane

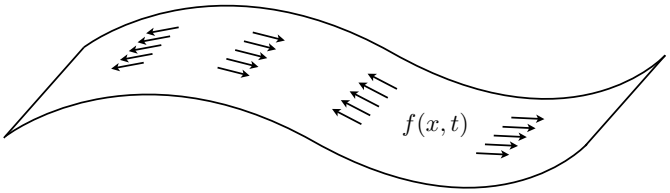

Figure 4.2: Active membrane where active two-dimensional moments are prescribed with density $f(x,t)$. Normal deformations arise over regions with a gradient in the active stress.

is given by [111]

$$G = \int \frac{\kappa}{2}(C - C_0)^2 dS + \int \gamma dS + G_{act}. \tag{4.7}$$

Here κ is the bending rigidity of the membrane, C is the mean curvature, C_0 is the so-called spontaneous curvature of the membrane, and γ the surface tension.

Real biological membranes are complex, containing proteins embedded in the surface, several layers of chemical activity, or possibly even an elaborate scaffolding of interlinked polymer networks (relevant, e.g., to the cytoskeleton in eukaryotic cells). For simplicity, we ignore these effects, as well as possible viscous dynamics inside the membranes, and focus on bending energetics [75, 112]. In addition, although spontaneous curvature can lead to interesting morphological consequences in cells and vesicles ([113, 76]), we work with $C_0 = 0$ and only consider local curvature changes from inclusions in the membrane. The form of the active contribution to the enthalpy, G_{act}, depends on the particular method of internal forcing [114]. Below we consider two models, focusing on internal bending moments and normal forcing to the membrane respectively.

4.3.1 Active bending stresses

Setup

In this first model, we assume that there is a distribution of forces acting entirely within the surface of the membrane. These forces then generate a moment distribution that depends on the thickness of the membrane itself. We then define an internal, prescribed two-dimensional moment per length (units of force) $f(x,t)$

(see Fig. 4.2). Balancing this activity with internal passive response and viscous fluid forces yields the instantaneous equations of mechanical equilibrium

$$\kappa\nabla^2 C + \hat{\mathbf{n}}\cdot\boldsymbol{\sigma}\cdot\hat{\mathbf{n}}|_S = \nabla^2 f \quad \text{(normal)}, \tag{4.8a}$$

$$\tau + \hat{\mathbf{t}}\cdot\boldsymbol{\sigma}\cdot\hat{\mathbf{n}}|_S = 0 \quad \text{(tangential)}, \tag{4.8b}$$

where $\tau = \gamma + \kappa C^2$ is the physical tension in the membrane, and $\hat{\mathbf{t}}$ and $\hat{\mathbf{n}}$ are vector tangent and normal to the membrane respectively. This equation is correct for any arbitrary distribution of forces, or any shape of the membrane, as long as ∇ is taken to be the covariant gradient. For long-wavelength membrane deformation, however, we already solved the fluid mechanics that results in fluid transport. In this case the membrane shape can be parameterized by a height field $h(x,t)$, and the curvature $C \approx \nabla^2 h$. To lowest order in the expansion of the height, the equations for the pointwise force balance across the membrane then become

$$2\kappa\frac{\partial^4 h^{(1)}}{\partial x^4} - \frac{\partial^2 f}{\partial x^2} = -p^{(1)} - 2\mu\left(\frac{\partial^2\psi^{(1)}}{\partial z\partial x}\right)_S, \tag{4.9a}$$

$$\tau^{(1)} = \left[\frac{\partial^2\psi^{(1)}}{\partial z^2} - \frac{\partial^2\psi^{(1)}}{\partial x^2}\right]_S. \tag{4.9b}$$

Using the expression for the first order stream function from the previous section, we find that to first order the tension $\tau^{(1)} = 0$: to lowest order in the deformation of the membrane, only normal effects are important [112].

Scalings

Using scaling arguments we derive in this section the expected scaling of the pumping velocity by the active membrane. In the context of the classical Taylor swimming sheet, the swimming velocity is expected to scale as $U \sim c(bk)^2$, where $c = \omega/k$ is the wave speed.

Two physical regimes need to be considered, those of "stiff" and "floppy" membranes. In the stiff regime, viscous forces are negligible compared to bending resistance, and thus the dynamic balance is between elastic and active stresses. The elastic stress in a membrane with rigidity κ, typical height deformation b_{eff}, and deformations occurring at typical wavenumbers k scales like $\kappa b_{\text{eff}} k^4$, while the

active stress is on the order of $f_0 k^2$. This yields a value for the effective height of the membrane as $b_{\text{eff}} \sim f_0/\kappa k^2$. We then expect pumping to occur at speed $U \sim c(b_{\text{eff}}k)^2 \sim \omega f_0^2/\kappa^2 k^3$.

In contrast, in the floppy limit the bending resistance is negligible and the dynamic balance is between viscous stresses and internal activity. The typical shear stress on the sheet scales as $\mu c b_{\text{eff}} k^2$. Force balance leads thus to the scaling $f_0 k^2 \sim \mu c b_{\text{eff}} k^2$, and the deformation is given by $b_{\text{eff}} \sim f_0/\mu c$. Fluid pumping is thus predicted to happen with speed $U \sim c(b_{\text{eff}}k)^2 \sim f_0^2 k^3/\mu^2\omega$. Interestingly, in floppy limit, the dependence of the pumping speed on both the sheet frequency and wavenumber is opposite to that in the stiff limit.

We now introduce the dimensionless group $a = 1/k\ell$ where $\ell = (\kappa/\mu\omega)^{1/3}$ is an elasto-viscous penetration length that determines how strongly the membrane shape is effected by the bending resistance versus the viscous forces (similar to the so-called "Sperm number" used to model viscous locomotion of flagellated organisms [59, 62]).

The dimensionless number a characterizes thus the relative size of the membrane deformation to this length scale. When $a \ll 1$ the membrane is stiff and hence it is energetically prohibitive to introduce an excitation of linear dimension the order of $1/k$, so the viscous forces do not modify the shape of the membrane and the waveform is a result of the balance between activity and rigidity alone. In contrast, when $a \gg 1$, the membrane is floppy, and the fluid forces dynamically balance the internal forces to determine the shape.

Asymptotics

Expanding the distributed moment in the same basis as the height field, namely $f = f_0 \text{Re}\{\sum f_n e^{in(kx-\omega t)}\}$, and utilizing the results for the pressure and streamfunction from the previous section we find the linear response for the height field as a function of the internal tangential stress

$$b_n = \frac{f_0}{2\kappa k^2 \left[n^3 + i2a^3\right]} f_n. \tag{4.10}$$

Using the result Eq. (4.10), we are then able to derive the pumping flow,

Eq. (4.4), as a function of the activity, elasticity, and viscosity, and we obtain

$$U^{(2)} = \frac{1}{2}\sum_n \omega k |n b_n|^2 = \frac{1}{8}\frac{\omega f_0^2}{\kappa^2 k^3}\sum_n \frac{n^2 |f_n|^2}{n^6 + 4a^6}. \tag{4.11}$$

In the stiff limit, $a \ll 1$, the asymptotic results in Eq. (4.11) recover the scaling derived in Sec. (4.3.1). For the floppy limit, $a \gg 1$, the series in Eq. (4.11) is only asymptotically convergent, but for a finite sum the scaling in Sec. (4.3.1) also holds.

4.3.2 Active normal stresses

Setup

In the section above we neglected the details of the activity within the membrane, in favor of a more generic modeling approach describing the relationship between fluid flow, internally applied bending moments, and passive bending resistance. In a biological context, many sources of activity could instead generate normal stresses in the membrane. Our second model, described below, considers a concentration of active elements dispersed throughout the membrane and generating fluid stresses.

A schematic of the proposed model system is sketched in Fig. 4.3. A dilute concentration of "pumps", each one capable of driving a microscopic flow through the membrane surface, act as inclusions, effectively modifying the material properties. Not only does the shape of the individual pump alter the shape of the membrane [115, 90], but the flow itself generates fluid stresses on the surface.

Each pump is modeled as a circular aperture of radius d. Since d is a molecular length scale far smaller than any other length scale, L, in the system, we can approximate the flow as resulting from a point source embedded in on a flat surface [116], such that the stream function is given by $\psi = -q/2\pi[1 - (\hat{\mathbf{t}} \cdot \mathbf{r}/r)^3]$, where $\hat{\mathbf{t}}$ is the radial tangent vector of the surface, $\mathbf{r}$ is the position of interest in the fluid, and q is the volumetric flow rate through the inclusion. The corresponding pressure drop across the aperture is $\delta p = 3q\mu/d^3$.

In order to satisfy the equations of force balance we need to calculate the normal and tangential stress due to not just one pump, but a concentration of in-

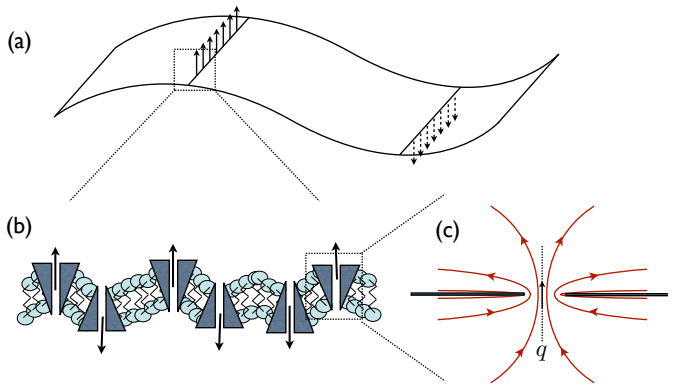

Figure 4.3: Schematic illustration of membrane deformation by active inclusions: (a) Active inclusions embedded in the surface; the inclusions induce flow fields which lead to pressure drop and thus normal stresses acting on the membrane; (b) Zoomed-in version of the membrane where the size of each inclusion and the local bending of the membrane are schematically represented; (c) Sketch of the streamlines for a single circular aperture in a flat surface pumping fluid with flow rate q; at leading order the molecular length scale, d, is much smaller than the typical membrane scale, L, and thus the flow is assumed to be unaffected by membrane curvature.

clusions. Each pump has a preferred direction, and thus we must generally consider the concentration difference, $n = n^+ - n^-$, where n^+ and n^- are the concentrations of pumps pointing in the positive and negative z directions, respectively. For convenience we will consider the dimensionless quantity $\phi = n/n_0$, where n_0 is the equilibrium concentration difference [115].

The normal stress on the membrane due to a single inclusion is simply the pressure drop from the fluid, while the tangential stress on the surface of the membrane decays like $1/\rho^2$, where $\rho = \sqrt{x^2 + y^2}$. The length scale d dominates this contribution, and thus the tangential stress is expected to scale as $1/d^2$. Locally this implies that the tangential stress per length is of the same order as the pressure drop, i.e. $\hat{\mathbf{t}} \cdot \boldsymbol{\sigma} \cdot \hat{\mathbf{n}} \sim q\mu/d^3$. However, because the stream function is axisymmetric, the tangential component of the fluid stress integrates to zero over the entire membrane, and thus does not enter the force balance equations.

A general functional describing the enthalpy of the membrane including

active pumps is given by

$$G = \int \frac{\kappa}{2}(C - H_0\phi)^2 dS, \tag{4.12}$$

where H_0 a signed measure of the intrinsic curvature for the active elements, and we have neglected effects from 2D compressibility in the concentration, as well as higher order effects coming from gradients in the concentration field [117, 115, 89].

Performing the functional extremization and linearization for the active pump enthalpy, and including the fluid stresses from pump activity, we now find the dynamic equations to be

$$\begin{aligned} 2\kappa\frac{\partial^4 h^{(1)}}{\partial x^4} - \kappa H_0\frac{\partial^2\phi}{\partial x^2} &= -p^{(1)} - \frac{q\mu}{d^3}\phi \\ &\quad -2\mu\left(\frac{\partial^2\psi^{(1)}}{\partial z\partial x}\right)_S, \qquad (4.13a) \\ \tau^{(1)} &= \left[\frac{\partial^2\psi^{(1)}}{\partial z^2} - \frac{\partial^2\psi^{(1)}}{\partial x^2}\right]_S. \qquad (4.13b) \end{aligned}$$

As in the case addressed in the previous section, the tangential stress balance yields zero tension at leading order.

Scalings

Here again we use scaling arguments to derive the expect form for the macroscopic flow pumped by the membrane. In addition to the stiff versus floppy regimes explained above, we must consider in addition the competition between by the spontaneous curvature and the deformation induced by the active pumping mechanism: In one limit the local stiffness introduced by the molecular curvature of the inclusions overrides the pumping activity, while in the opposite limit the spontaneous curvature is negligible.

Let us denote by ϕ_0 the typical magnitude of the dimensionless concentration of pumps, and the typical force generated by the pumps as $f_{act} = q\mu/d$. To measure the competition between the natural curvature of the inclusions and the one arising from the activity-induced fluid flow, a dimensionless parameter, $A = H_0\kappa d^2k^2/f_{act}$, needs to be introduced.

For stiff membranes, in the limit where the bending from activity is predominant, i.e. $A \ll 1$, force balance reveals that $b_{\text{eff}} \sim f_{act}\phi_0/\kappa d^2 k^4$, while in the opposite limit where the bending arises from molecular curvature, we get $b_{\text{eff}} \sim \phi_0 H_0/k^2$.

In contrast, for floppy membranes, the case of very active inclusions leads to the scaling $b_{\text{eff}} \sim f_{act}\phi_0/\mu\omega_0 d^2 k$, while in the limit where the inclusions pump a very small amount of fluid transverse to the membrane ($A \gg 1$), we obtain $b_{\text{eff}} \sim H_0\phi_0\kappa k/\mu\omega$.

Now, the expected fluid velocities in the four different limits can be found by again using the analogy with the swimming sheet, $U \sim c b_{\text{eff}}^2 k^2$. For stiff active membranes, we expect $U \sim \omega(f_{act}\phi_0)^2/\kappa^2 d^4 k^7$, while stiff inactive membranes should lead to $U \sim \omega(H_0\phi_0)^2/k^3$. In the inactive case we note that the fluid velocity no longer depends on the membrane stiffness, as the intrinsic curvature H_0 governs the bending penalty at the same order in κ as local deformations in the height field.

In the case of floppy active membranes, we expect to obtain a relationship for $U \sim (f_{act}\phi_0)^2/\mu^2 d^4 \omega k$, while for inactive floppy membranes the pumping flow should scale like $U \sim (H_0\phi_0\kappa)^2 k^3/\mu^2\omega$. It is notable that even in the inactive case, the mismatch of curvature between the inclusions and the elastic membrane they are embedded in can, alone, lead to deformation that gives rise to pumping; even in the floppy limit consequences of the bending rigidity κ cannot be neglected.

Asymptotics

Using the Fourier decomposition for the concentration of inclusions, $\phi(x,t) = \sum \phi_n e^{in(kx-\omega t)}$, the linear response of Eq. (4.13) is found to give

$$n^4 k^4 b_n + \frac{i2\mu\omega n k}{\kappa} b_n = -H_0 n^2 k^2 \phi_n - \frac{f_{act}}{\kappa d^2}\phi_n. \tag{4.14}$$

The final linear response for the height takes the form

$$b_n = -\frac{f_{act}}{\kappa k^4 d^2}\frac{1 + An^2}{n^4 + i2a^3 n}\phi_n. \tag{4.15}$$

Plugging Eq. (4.15) into Eq. (4.4) we finally find that the macroscopic velocity is given by

$$U^{(2)} = \frac{1}{2}\sum_n \omega k |n b_n|^2 = \sum_n \frac{1}{8}\frac{\omega f_{act}^2}{k^7 d^4 \kappa^2}\left[\frac{(1+An^2)^2}{n^8+4n^2a^6}\right]|\phi_n|^2. \tag{4.16}$$

In the stiff ($a \ll 1$) and floppy ($a \gg 1$) limits, as well as the limits where intrinsic pump curvature dominates ($A \gg 1$) or is dominated by ($A \ll 1$) deformation from the active normal stresses, the final asymptotic results in Eq. (4.16) confirm all the scaling predictions in Sec. 4.3.2.

4.4 Discussion

In summary, although the framework for characterizing fluid transport and locomotion by a waving sheet has existed since the 50's, in this work we have attempted to go beyond a prescription of surface deformation by instead prescribing internal activity (so starting from dynamics instead of kinematics). Both membrane deformation and fluid transport can then be solved by solving a dynamic balance between activity, passive resistance, and external fluid stresses. We have used two models to cover a range of possible forcing, a planar distribution of bending moments that generate normal deformation, and a simple model of active constituents that produce normal permeative flow, resulting in sheet undulation.

From an experimental standpoint, what is the typical magnitude of the flow which could be induced by active mechanisms similar to the ones described in this paper? For lipid bilayers, bending rigidities are on the order of $\kappa \sim 10^{-19} Nm$ [118], and using cross-linked molecular motors as one model microscopic force generator, a single molecular machine could generate forces on the order of $\sim 1pN$ [119]. If these were distributed throughout a membrane, say with a dimensionless concentration of $\phi \sim 10^{-3}$,

we could expect a magnitude for the internal moment per unit length of $f_0 \sim 10^{-15} N$.

On cellular length scales $L \sim 100\mu m$, with $k \sim 1/L$, the range of frequencies $\omega \sim 10^0 - 10^2 Hz$ could include both the the stiff and floppy regimes, and as a

result we could expect macroscopic velocities on the order of $U \sim 1\mu m/s$ for low frequencies (stiff limit) or $U \sim 1 - 100\mu m/s$ for higher frequencies (floppy regime).

For transmembrane proteins capable of inducing a microscopic flow through a surface, such as aquaporins or proton pumps, the volumetric flow rate is difficult to estimate, but we can use previous simulation results for guidance [120, 121]. For membrane constituents such as lipids or proteins a typical radius of gyration gives $H_0 \sim 1nm^{-1}$ [118]. This yields a value for the parameter $A \sim (10^{-18}N)/f_0$. For molecular motors generating fluid flow normal to the membrane with a force per motor on the order of $f_0 \sim 1pN$, this makes $A \ll 1$, i.e. the active limit; for aquaporins or other active pores that are not designed specifically to move cellular structures, $A \gg 1$. With a frequency of oscillation of $\omega \sim 1Hz$, these membranes are in the stiff limit. With a dimensionless concentration as small as $\phi_0 \sim 10^{-3}$, the macroscopic pumping velocity can be as large as $U \sim 10 - 100\mu m/s$ for the active case, and $U \sim 1\mu m/s$ for inactive membranes.

One possible experimental realization for a self-propelled active membrane could be in the form of a closed bilayer vesicle with embedded active pumps. For a spherical vesicle of radius R and wavelength undulations satisfying $\lambda \gg R$, we can use the above calculations in tandem with the swimming results of Stone and Samuel [109] to get an estimate of the vesicle swimming speed

$$U\hat{\mathbf{z}} \approx -\frac{1}{4\pi R^2}\int_S \mathbf{u} dS., \tag{4.17}$$

where $\mathbf{u} = U^{(2)}\mathbf{t}$ is the local fluid velocity created by the activity-induced membrane deformation; up to a geometric constant, we thus get that the instantaneous swimming velocity of this active vesicle is the same as that given in our calculations above. Several previous studies have examined the possibility of self-propelled vesicles [122, 110, 101], and our results connecting the internal stress state to macroscopic motion can thus be used as a probe of the activity. One could envision a situation where the diffusivity of active vesicles is measured. In the presence of active pumps, this diffusivity would then be enhanced by the propulsion velocity as $D_{eff} \sim U^2/D_r$, where D_r is the vesicle rotational diffusion [8], which could then be directly related to the activity via the results derived in this paper. This

framework could serve, for example, as a way to rule out specific forms of activity in a membrane.

4.5 Swimming vesicles

In the same spirit, we consider theoretically in this section a novel swimming mechanism based on prescribed shape transformations of a bilayer vesicle. By modulating only its volume and membrane composition, the vesicle can be made to change shape quasi-statically in thermal equilibrium. For two different theoretical vesicle models, we determine numerically the vesicle shapes through an enthalpy minimization, and the fluid-body interactions by solving a boundary integral formulation of the Stokes equations. When the control parameters are tuned appropriately to yield periodic but not time-reversible shape changes, we show that net locomotion can be obtained. Swimming arises either by continuously modulating fore-aft asymmetric vesicle shapes, or by crossing a continuous shape-transition region and alternating between fore-aft asymmetric and fore-aft symmetric shapes. In addition, the calculated hydrodynamic efficiencies are shown to be similar to that of other common low Reynolds number propulsive mechanisms.

This section is organized as follows: we begin with a general discussion of the practical realization of controlled shape-changing vesicles, in particular the relevant time scales, and the possible actuation mechanisms. Two classical curvature-mediated vesicle models (spontaneous curvature and bilayer coupling) are presented, and the formulations used for the shape calculation and the numerical fluid-interaction model are introduced. We then discuss examples of vesicle shape cycles that yield a swimming motion, examine the fluid flow that develops around the vesicles during their deformation cycles, and compute the corresponding swimming speeds and hydrodynamic efficiencies.

4.6 A Roadmap to Vesicle Locomotion

A vesicle immersed in a viscous fluid experiences a highly coupled array of forces, such as those generated by membrane tension, internal pressure, membrane (bending) elasticity, and the surrounding viscous fluid dynamics. In the microscopic, viscous environments relevant to our consideration, the Reynolds number, Re, is very small: $\mathrm{Re} = \rho U_c L_c/\mu \ll 1$, where ρ is the fluid density, μ is the fluid shear viscosity, and U_c and L_c are characteristic velocity and length scales of the vesicle. The fluid behavior at low Reynolds number is highly dependent upon the immersed boundary geometry, and the resultant forces include not only local, but also non-local responses to its motion.

A general study of vesicle dynamics should take non-equilibrium shapes into account, as even simple liposomes that can be created in situ can interact relatively quickly with the environment. It is possible to design experiments where carefully constructed initial conditions and lipid species lead to equilibrated vesicle shapes that are non-trivial, but in order to apply morphological changes and induce locomotion, a reversible parameter-changing mechanism is desirable.

For our first approach to vesicle swimming, we consider in this paper a "stiff membrane" regime. The characteristic time of membrane relaxation in a viscous fluid is given by $t_{rel} = \mu r_0^3/\kappa$, where κ is the elastic bending modulus of the membrane, and r_0 is a characteristic radius of curvature. If we choose the maximum radius of the vesicle for the characteristic length scale L_c, then $r_0 \lesssim L_c$. For parameter variation significantly slower than the membrane relaxation rate, *i.e.* for a cycle time scale $t_{cycle} \gg t_{rel}$, then we operate safely within the decoupled regime. In this case, we may thus assume that there are no hydrodynamically induced shape changes, and that the shapes are determined quasi-statically in equilibrium. Using this time scale t_{rel}, we can also set a maximum swimming velocity scale, $U_c = \kappa/\mu r_0^2$. Similar scaling arguments have been made in Refs. [123, 124]. For biologically relevant systems in water, $\kappa \approx 100$ $\mathrm{k}_B\mathrm{T}$, $\mu \approx 10^{-3}$Pa s, $\rho = 1$ g/cm^3, and $r_0 \lesssim 1 - 10$ μm, leading to $L_c \approx 1 - 10$ μm, $U_c \approx 1 - 10$ μm/s, $t_{rel} \approx 0.01 - 1s$ and $Re \approx 10^{-4}$. For a vesicle with length scale $L_c = 10$ μm, diffusive time scales are approximately $10^4 s$, and thus negligible for the time being. In addition, we

neglect thermal fluctuations in the determination of the vesicle shape, as they come in as a perturbation about the mean equilibrium shape of order $(k_BT/\kappa)^2$, which is very small under most conditions [75].

There are a number of different physical means by which a vesicle shape can be changed in a controlled fashion, and the methods could be different depending on the type of vesicle considered. We will consider two such means, internal volume changes and local membrane compositional changes.

One experimentally feasible example of a possible volume-changing mechanism is a light-induced osmotic change. In an ordinary biological membrane the bilayer is embedded with numerous proteins, many of which are sensitive to mechanical forces, chemical gradients, or light. The protein bacteriorhodopsin, for example, is sensitive to green light, and in response to a signal the protein opens and closes like a valve [104]. The presence of such ion channels or active proteins on the surface of a membrane can cause osmotic changes of the fluid volume contained within the vesicle [87]. Recently, vesicle volume control was demonstrated via pH modulation of block copolymer networks along the surface of membrane [125]. The vesicles in this study were well separated from regimes associated with morphological transition, and thus changes in osmotic pressure induced only a volume change, leading to a "breathing" vesicle.

Adjusting the membrane composition requires a more indirect experimental approach. Some bilayers are composed of different species of constituent parts, leading to an inherent mismatch between the intrinsic curvatures. In other words, there is an intrinsic curvature that would develop across the bilayer in the absence of other considerations. Because of the inherent difficulty in measuring these quantities it is likely to be more difficult to specify an exact change from one value of intrinsic curvature to another. However, the actual process of changing the intrinsic curvature can be achieved through inducing chemical changes of the lipid constituents of the membrane [125], or by conformational changes of polymers grafted to the surface of the vesicle [126].

By combining two shape-changing mechanisms, it would in theory be possible to achieve a periodic shape cycle which is not time-reversible, yielding a net

locomotion. One of many possible configurations that could produce a cycle in shape space is displayed schematically in Fig. 4.4, where we consider a bilayer vesicle with embedded reactive polymers and with polymers grafted to its surface. In the first step (Fig. 4.4a→b), a photo-chemical polymerization reaction is catalyzed by green (short wavelength) light, and the polymer chains in the interior of the vesicle disperse into a solution of particles, thus increasing the available volume within the vesicle. At a later time, another frequency of light (red, or longer wavelength) impinges on the vesicle, and the grafted polymers change from a distended to a coiled conformation, inducing an entropic repulsion and changing the curvature of the membrane (Fig. 4.4b→c). Over time the dispersed particles will polymerize and return the vesicle to its original volume (Fig. 4.4c→d), and finally a third frequency of light (blue or very short wavelength) can be used to change the conformation of the polymers to distended once more, returning the vesicle to its original state (Fig. 4.4d→a).

While osmotic volume change or chemical-induced composition alteration are two possible experimental methods, not only these examples in no way constitute the full set of possibilities, but also they might be difficult to implement experimentally. Other experimental techniques already exist (see Refs. [125, 87]), or may be developed in the near future that could be more suited for controlled two-parameter change.

Rather than suggest specific experimental methodology whose specifics would depend not only on the particular material of the bilayer vesicles, but also on the parameter alternation methods, we adopt in this paper a simplified modeling approach that highlights the qualitative pieces that are required in order to transform a motionless vesicle into a locomotive cargo-carrier. In parallel to the the various practical mechanisms that could be used to implement such shape changes experimentally, it is of fundamental interest to ask theoretically the question of prediction and performance. Would shape change indeed lead to locomotion of the vesicle? How efficient would it be? Can we quantitatively predict the resulting swimming speed and the work done against the fluid to achieve it? This is the approach taken in this paper. Considering two simplified vesicle models, and for slow modu-

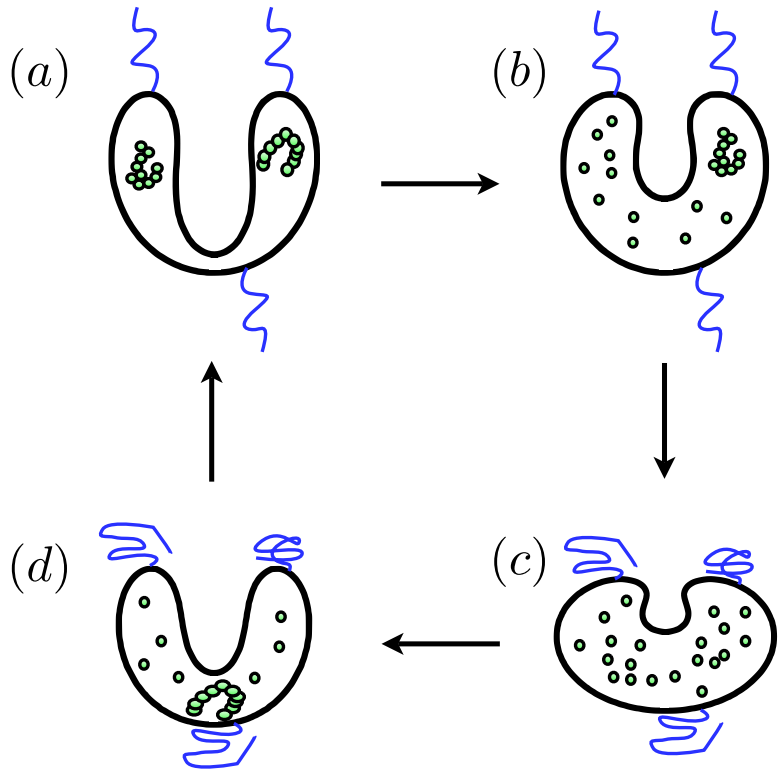

Figure 4.4: Schematic illustration of a possible control mechanism for vesicle shape-change and swimming: Axisymmetric bilayer vesicle with embedded reactive polymers and polymers grafted to its surface. $(a) \rightarrow (b)$: Short frequency light impinges on the vesicle, catalyzing a de-polymerization reaction amidst the particle chains, and increasing the fluid volume available to the vesicle. $(b) \rightarrow (c)$: A second frequency of light induces the grafted polymers to coil up, inducing an entropic repulsion from the membrane and changing the macroscopic morphology. $(c) \rightarrow (d)$: The dispersed particles begin to polymerize back to their initial configuration, deflating the vesicle. $(d) \rightarrow (a)$: A third frequency of light is used to uncoil the polymers, relaxing the entropically induced curvature and returning the vesicle to its initial state.

lations of the vesicle shapes, we introduce below a computational framework able to quantitatively predict swimming kinematics and performance.

4.7 Dynamics of Coupled Fluid-Body System

4.7.1 Vesicle physics

While real biological membranes have multiple constituents, all interacting in non-trivial ways, minimal models can still help to illuminate the fundamental physics of such systems. For length scales on which a membrane is approximately flat a Monge parameterization can be employed [115, 117, 127], but for a closed bilayer vesicle the curvatures can become very large and the small geometric gradient assumption may break down. In order to characterize the shapes of such objects, an enthalpy must be extremized and the full nonlinear shape equations so generated must be solved. There are many models that could be used to describe the physics of curvature-mediated vesicle morphology. In this paper we will consider two classical models as case studies. These formulations, known respectively as the spontaneous curvature and bilayer coupling models, have both been used in classical work [128] and correspond to different interaction dynamics between the membrane monolayers. Both of these models also include exactly two free parameters, which enable us to explore the breaking of the Scallop theorem, and the generation of locomotion via a change in morphology.

The enthalpy functional, F, in the spontaneous curvature model takes the following form [128]

$$F = \frac{\kappa}{2} \int_{S(t)} \left(C_1 + C_2 - C_0\right)^2 dS + \Sigma\, A + P\, V, \tag{4.18}$$

where C_1 and C_2 are the principal membrane curvatures, and Σ and P are Lagrange multipliers which constrain the surface area A and volume V (physically they correspond to the membrane tension and pressure difference across the interface). In Eq. (4.18), $S(t)$ denotes the time-dependent surface boundary, and C_0 is the spontaneous curvature, which introduces an inherent mismatch in equilibrium preference of the membrane curvature. This quantity along with a fixed volume and surface area completely specifies the ensemble. Thus the spontaneous curvature model has area, volume, and integrated spontaneous curvature constrained, and we select as the control parameters the volume V and the spontaneous curvature

C_0 (the fixed surface area merely selects the overall size of the vesicle).

In contrast, in the bilayer coupling model, the enthalpy functional G assumes the area difference ΔA between the membrane monolayers to be constant. One possible representation of this area difference is in terms of the integrated mean curvature,

$$M = \int_{S(t)} (C_1 + C_2)\, dS. \tag{4.19}$$

Then the area difference is $\Delta A = 2hM + O(h^2/A)$, where h is the distance between monolayers [128]. The enthalpy then takes the form

$$G = \frac{\kappa}{2} \int_{S(t)} (C_1 + C_2)^2\, dS + \Sigma'\, A + P\, V + Q\, M, \tag{4.20}$$

where Σ', P, and Q are Lagrange multipliers associated with A (area), V (volume) and M (integrated mean curvature) respectively. We select as control parameters the volume V and the integrated mean curvature M.

It is important to note that the functionals F and G are related via a Legendre transform, $(\Sigma', Q) \to (\Sigma + \kappa\, C_0^2/2, -2\kappa\, C_0)$, and thus describe the same system in a different ensemble. Physically, the spontaneous curvature model corresponds to a bilayer in which the monolayer admits stretching or compression during bending, and thus finds an equilibrium distribution that has a preferred curvature. If the bilayer is composed of more than one species of lipid, each of which has a different preferred curvature (*i.e.* radius of gyration), it is likely that the membrane will actually prefer to be in a non-flat state. Conversely, the bilayer coupling model corresponds to a system that enforces that both monolayers are incompressible. The area difference between monolayers stays approximately constant on the timescales relevant to our consideration, and as long as the distance between layers remains very small this implies that the integrated mean curvature also remains constant.

4.7.2 Determination of the vesicle shape

Assuming an axisymmetric vesicle shape, the body surface $S(t)$ is parameterized at each time t as illustrated in Fig. 4.5. The arc-length measured along the

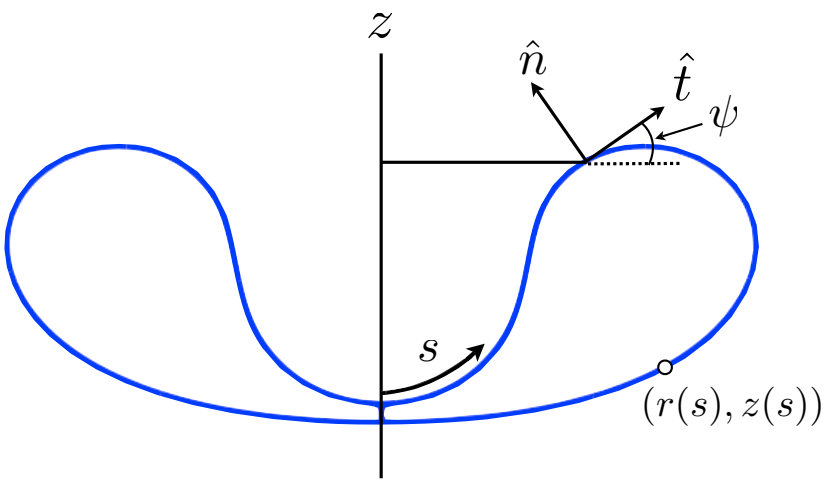

Figure 4.5: Parameterization of an axisymmetric bilayer vesicle. We assume axisymmetry about the z-axis. The surface is described by $\mathbf{x} = (r(s,t), z(s,t))$ in cylindrical coordinates, with s an arc-length parameter, $\hat{\mathbf{t}}$ the unit tangent vector, $\hat{\mathbf{n}}$ the outward pointing normal vector, and ψ the angle between the x-axis and $\hat{\mathbf{t}}$.

surface in the x-z plane is denoted by $s \in [0, L]$, with $\hat{\mathbf{t}}$ the unit tangent vector, $\hat{\mathbf{n}}$ the outward pointing normal vector, and ψ the angle between the x-axis and $\hat{\mathbf{t}}$. The body surface is represented in cylindrical polar coordinates,

$$\mathbf{x}(s, \phi, t) = \tilde{\mathbf{x}}(s, \phi, t) + z_0(t)\hat{\mathbf{z}} = (r(s,t)\cos(\phi), r(s,t)\sin(\phi), z(s,t) + z_0(t)), \tag{4.21}$$

where $\phi \in [0, 2\pi)$ is the azimuthal angle, the surface $\tilde{\mathbf{x}}$ is taken to have its center of volume at the origin, and $z_0(t)$ is a translation of that center of volume which depends upon the fluid interaction. Under this parameterization, the principal membrane curvatures are $C_1 = \partial\psi/\partial s$ and $C_2 = \sin\psi/r$. Upon insertion into either of the enthalpy functionals F or G, and performing a variational extremization, we obtain the following system of first-order ordinary differential equations to describe the energetically stationary vesicle shapes at time t [128]

$$\psi_s = K, \tag{4.22}$$

$$K_s = -\frac{K}{r}\cos\psi + \frac{\gamma}{r}\sin\psi + \frac{\cos\psi\sin\psi}{r^2} + \frac{1}{2}Pr\cos\psi, \tag{4.23}$$

$$\gamma_s = \frac{(K - C_0)^2}{2} - \frac{\sin^2\psi}{2r^2} + Pr\sin\psi + \Sigma, \tag{4.24}$$

$$r_s = \cos\psi. \tag{4.25}$$

Here K is an auxiliary function used to make the system of equations first-order (physically it corresponds to the curvature), γ is the Lagrange multiplier that enforces the interdependence of ψ and r, and the subscript s denotes a derivative with respect to the arclength. The vesicle shape at time t is set by Eqs. (4.22-4.25), subject to the four boundary conditions $r(0,t) = r(L,t) = \psi(0,t) = 0$ and $\psi(L,t) = \pi$. Once the angle ψ is determined from the above, $z(s,t)$ is set by an integration of $z_s = \sin(\psi)$, where the constant of integration is chosen such that the center of volume of the surface $\tilde{\mathbf{x}}$ is at the origin. The vertical position $z_0(t)$ has no bearing on the vesicle shape determination, and we hold off further discussion on its dynamics until the following section.

For the spontaneous curvature model, constraints on the unknown integration length L, the surface area A, the volume V, and the two constant Lagrange multipliers P and Σ are imposed as

$$A_s = 2\pi r, \quad V_s = \pi r^2 \sin\psi, \quad P_s = 0, \tag{4.26}$$

$$\Sigma_s = 0, \quad L_s = 0. \tag{4.27}$$

Defining R_0 as the radius of the sphere with surface area A, the boundary conditions for the five constraint equations above are $A(0) = V(0) = 0$, $A(L) = 4\pi R_0^2$, $V(L) = 4\pi R_0^3 v/3$, where v is a dimensionless "reduced volume." Due to the Lagrange function being independent of the arc-length s, the "Hamiltonian" is a conserved quantity and we have $\gamma(0) = 0$ (see Refs. [128, 129]). Also defining a reduced spontaneous curvature $c_0 = C_0 R_0$, we finally obtain the vesicle morphology as set by the two parameters (v, c_0).

In the bilayer coupling model, Eqs. (4.22-4.27) are solved with two additional constraints. First, the integrated mean curvature M is controlled, $M_s = \pi(rK + \sin\psi)$, and second, a new Lagrangian constraint enters, $Q_s = 0$. The system is now closed with boundary conditions on the integrated mean curvature: $M(0) = 0$ and $M(L) = 4\pi R_0 \Delta a$, where Δa is the reduced surface area difference between monolayers, $\Delta a = \Delta A / 8\pi R_0 h$. In this case the vesicle morphology is set by the two parameters $(v, \Delta a)$, and the reduced spontaneous curvature c_0 has been removed from the shape equations via the Legendre transform given above.

Equations (4.22-4.27) are solved numerically. Due to coordinate singularities in the derivatives of r and z at the poles, the shape is determined on the contracted interval $s \in [L\,\delta, L\,(1-\delta)]$ for $(L\,\delta) \ll 1$, and Taylor-expanded versions of the boundary conditions are applied. For example,

$$\begin{aligned} r(L\,\delta,t) &= r(0,t) + (L\,\delta)\,r_s(0,t) + O\left((L\delta)^2\right) = (L\,\delta)\,r_s(L\,\delta,t) + O\left((L\delta)^2\right) \\ &= (L\,\delta)\cos(\psi(L\,\delta)) + O\left((L\delta)^2\right) \approx L\,\delta. \end{aligned} \tag{4.28}$$

To compute the shapes using either model, the arc-length is discretized using m uniformly spaced grid points, s_i, with $s_1 = L\delta$ and $s_m = L(1-\delta)$. A collocation method is then applied in a formulation and implementation similar to that recently used by Jiang et al. [129]. We employ a standard continuation scheme in order to interpolate solutions from one point in the parameter space (v, c_0) or $(v, \Delta a)$ to neighboring points.

By extremizing the enthalpies F or G, the shape equations give only stationary solutions, not necessarily the lowest energy solutions. A numerically determined shape may correspond to an energy saddle point, maximum, or minimum. Although it is possible that the lowest energy state may not be achievable for a non-equilibrium shape change, for our purposes we will examine the minimum energy shapes, and thus a "phase diagram" for the possible shapes is of great use. Just as in a more conventional phase transition, shape transformations correspond to transitions between different symmetry states. Since we consider only axisymmetric shapes here, spherical solutions have the highest symmetry state. For small perturbations around spherical shapes, the solution can be represented as

$$r(s,t) = R_0\left(1 + \sum_{\ell=0}^{\infty} B_{\ell 0} Y_\ell^0(\theta(s), \phi = 0, t)\right), \tag{4.29}$$

where the functions Y_ℓ^0 are the spherical harmonics, and the constants $B_{\ell 0}$ can generate symmetry breaking. Because we consider only axisymmetric vesicles, only the $m = 0$ spherical harmonics (of the Y_ℓ^m) contribute to the sum, and the angle θ is given by $\tan\theta = r/z$. While it is not possible to produce an analytical solution using this formulation, it is useful for understanding the morphological transitions in terms of symmetry breaking. For example, breaking $\ell = 2$ symmetry

($B_{20} \neq 0$) leads to a prolate or oblate shape, while breaking $\ell > 2$ symmetry can give more complicated shapes, such as the so-called "pear" or "stomatocyte" shapes [75]. In our numerical investigation, symmetry is frequently exploited in order to efficiently compute the equilibrium shape. In regions of multiple stability the solution branches that correspond to lowest energy shapes must be chosen, and by inserting numerically an initial symmetry breaking the algorithm used can more readily converge upon the appropriate solution.

4.7.3 Fluid-body interaction

Modulation of the dimensionless parameter set (v, c_0) or $(v, \Delta a)$ generates quasi-static deformations which in turn lead to motion in the surrounding fluid medium. Given that the Reynolds number is small, the dynamics of the fluid surrounding the vesicle is effectively governed by viscous dissipation and is well modeled by the incompressible Stokes equations,

$$\nabla \cdot \boldsymbol{\sigma} = 0, \quad \nabla \cdot \mathbf{u} = 0, \tag{4.30}$$

where $\boldsymbol{\sigma} = -p\mathbf{I} + 2\mu\mathbf{E}$ is the Newtonian stress tensor with p the pressure, $\mathbf{u}$ the fluid velocity, and $\mathbf{E}$ the symmetric rate-of-strain tensor, $\mathbf{E} = \frac{1}{2}(\nabla\mathbf{u} + (\nabla\mathbf{u})^T)$. The fluid equations are made dimensionless by scaling velocities upon U_c, lengths upon L_c, and time upon $t_{rel} = L_c/U_c$. Since the surface area $A = 4\pi R_0^2$ is constant, we define the characteristic length scale by this radius, *i.e.* $L_c = R_0$. Henceforth, the swimming velocity is understood to be dimensionless, and each shape cycle occurs over a unit in dimensionless time.

A no-slip condition is applied on the body surface. For a given path through the parameter space (v, c_0) or $(v, \Delta a)$, the resulting sequence of instantaneously determined shapes set uniquely the "surface deformation velocity" $\mathbf{u_d}(\mathbf{x}, t)$; namely,

$$\mathbf{u_d}(\mathbf{x}(s, \phi, t), t) = \frac{\partial \tilde{\mathbf{x}}}{\partial t}(s, \phi, t). \tag{4.31}$$

In addition, the surface moves as a rigid body along the $\hat{\mathbf{z}}$ direction due to axisymmetry, with velocity $\mathbf{U} = U\hat{\mathbf{z}} = z_0'(t)\hat{\mathbf{z}}$. The no-slip condition is thus written as $\mathbf{u}(\mathbf{x}, t) = U\hat{\mathbf{z}} + \mathbf{u_d}(\mathbf{x}, t)$.

To close the system of equations describing the fluid-body interaction, we assume that no external forces are acting upon the vesicle, and thus force and torque balance give

$$\int_{S(t)} \boldsymbol{\sigma}(\mathbf{x}) \cdot \hat{\mathbf{n}}(\mathbf{x})\, dS = 0, \quad \int_{S(t)} \mathbf{x} \times [\boldsymbol{\sigma}(\mathbf{x}) \cdot \hat{\mathbf{n}}(\mathbf{x})]\, dS = 0. \tag{4.32}$$

The computation of the swimming velocity is performed using a standard double-layer boundary integral formulation of the Stokes equations. The details of this formulation and numerical method are presented in the appendix.

In addition to computing the swimming velocity, we consider a possibly more important quantity, the hydrodynamic efficiency. This swimming efficiency is defined as (see Ref. [47])

$$\eta_H = \frac{\Big\langle \mathbf{U} \cdot \mathbf{F} \Big\rangle}{\Big\langle \displaystyle\int_{S(t)} (\mathbf{U} + \mathbf{u_d}) \cdot \mathbf{f}\, dS \Big\rangle} = \frac{\Big\langle \mathbf{U} \cdot \mathbf{F} \Big\rangle}{\Big\langle \displaystyle\int_{S(t)} \mathbf{u_d} \cdot \mathbf{f}\, dS \Big\rangle}, \tag{4.33}$$

where $\mathbf{f} = -\boldsymbol{\sigma} \cdot \hat{\mathbf{n}}$ is the force density acting on the fluid at the body surface, $\langle \cdot \rangle$ denotes a time-average over a full shape cycle, and $\mathbf{F} = 6\pi\mu\, a\, U \hat{\mathbf{z}}$ is the force required to move a sphere of radius a at a speed U. At each time we use the maximum vesicle radius, $a(t) = \|r(s,t)\|_\infty$. The first term in the denominator of Eq. (4.33) integrates to zero due to the zero-net force condition (Eq. (4.32)). The computation of the fluid stress $\boldsymbol{\sigma}$ is significantly more involved than the computation of the swimming velocity. We employ a numerical method for computing $\boldsymbol{\sigma}$ based on the evaluation of a hypersingular integral which may be derived from the double-layer formulation of the fluid velocity. The framework and numerical approach are described in the appendix, and a more detailed description of the method and examples of its use will be featured in a subsequent paper.

Physically, η_H measures the proportion of work done by the vesicle against the surrounding fluid which is used for swimming purposes, and is typically on the order of 1% for biological cells. Note that the swimming efficiency only measures the hydrodynamic efficiency, not a total efficiency. For example, the bending energy of the vesicle is not captured in this measure. The inclusion of bending costs into swimming efficiency measures has recently been proposed to study optimal

locomotion strategies in flagellated cells, but presents an avenue of inquiry beyond the scope of this paper [130].

4.8 Vesicle locomotion by shape-change

As stated in the introduction, due to the linearity and time-reversibility of Eqs. (4.30), any time-reversible geometrical surface deformations cannot result in a net locomotion. This result is known as the Scallop theorem, in reference to the sole, time-reversible motions available to a small scallop (opening and closing) [72]. As a consequence of this constraint, a single degree of freedom is insufficient for swimming. Two degrees of freedom are however sufficient to generate a swimming motion, as first described in Ref. [72], and as we shall show presently for the systems of interest.

4.8.1 Spontaneous curvature model

We begin by presenting a characteristic shape cycle that can be generated by adjusting the reduced volume and spontaneous curvature, (v, c_0), in a periodic fashion. By selecting a specific elliptical path in the (v, c_0) parameter space, namely $v(t) = 0.425 + 0.125\cos(2\pi t)$, $c_0(t) = -0.1 + 0.3\sin(2\pi t)$, the resulting shape cycle is not time-reversible; hence, the constraints of the Scallop theorem are bypassed, and locomotion may be achieved. For these parameters the vesicle shapes are always stomatocytes, and the neck separating the internal sphere of fluid from the external fluid is very small. Figure 4.6 shows the corresponding minimal energy vesicle shapes at four times, along with the vorticity generated in the surrounding fluid by the body deformation, $\boldsymbol{\omega} = \nabla \times \mathbf{u}$. Positive vorticity, corresponding to counter-clockwise rotation, is shown in red, and negative vorticity, corresponding to clockwise rotation, is shown in blue. Hollow arrows indicate the instantaneous swimming velocity of the vesicle, while the plain arrows indicate the direction of time. At zero Reynolds number the swimming velocity, external flow, and swimming efficiency are determined uniquely by the time-dependent surface geometry and surface deformation velocity, so we need not consider the internal

flow dynamics (which may in general depend upon the means of modulating the parameters (v, c_0)).

From $t = 0$ to $t = 1/4$ the vesicle volume is decreasing while the spontaneous curvature is increasing. The decrease in volume draws fluid into the stomatocyte cavity, while the surface material near the opening to the cavity moves inward nearly tangentially to the surface itself. While the deformation velocity is normal to the surface near the north and south poles ($s = 0$ and $s = \pi$), the deformations are elsewhere primarily tangential, and vorticity is created as the fluid is sheared accordingly. At $t = 1/2$ the vesicle volume is minimal, and the fluid volume inside the stomatocyte cavity is beginning to decrease. From $t = 1/2$ to $t = 3/4$, the vesicle volume increases while the spontaneous curvature continues to decrease to its minimum value. This can best be understood by observing that when $c_0 < 0$ the membrane prefers a total negative curvature, and as can be seen at $t = 3/4$, the internal cavity of the vesicle takes its smallest value, maximizing negative curvature. The increasing volume expels fluid from the cavity, and leads to a reversing of the sign of the vorticity. The overall sequence of asymmetric shapes is not time-reversible, leading to a net swimming velocity taking place in the $-\hat{\mathbf{z}}$ direction.

A phase diagram for the minimal energy shapes using the spontaneous curvature model is presented in Fig. 4.7a. The limit lines correspond to discontinuous morphological transitions, and therefore cannot be crossed in our quasi-static shape-change approach. One critical line corresponds to vesicles whose north and south poles self-intersect, and a second line corresponds to stomatocyte shapes that have a vanishing opening between the external fluid and the cavity within (*i.e.* the shapes are two spheres, one contained entirely within the other). A third line marks the discontinuous phase transition between stomatocyte and oblate shapes. More details may be found in Ref. [128].

Beyond the symmetry constraints imposed by the Scallop theorem, other symmetry breaking is necessary in order for a body to achieve a net motion from a periodic shape cycle. Namely, the body surface must express fore-aft asymmetry in order to swim preferentially in any direction. Hence, parameter paths in the

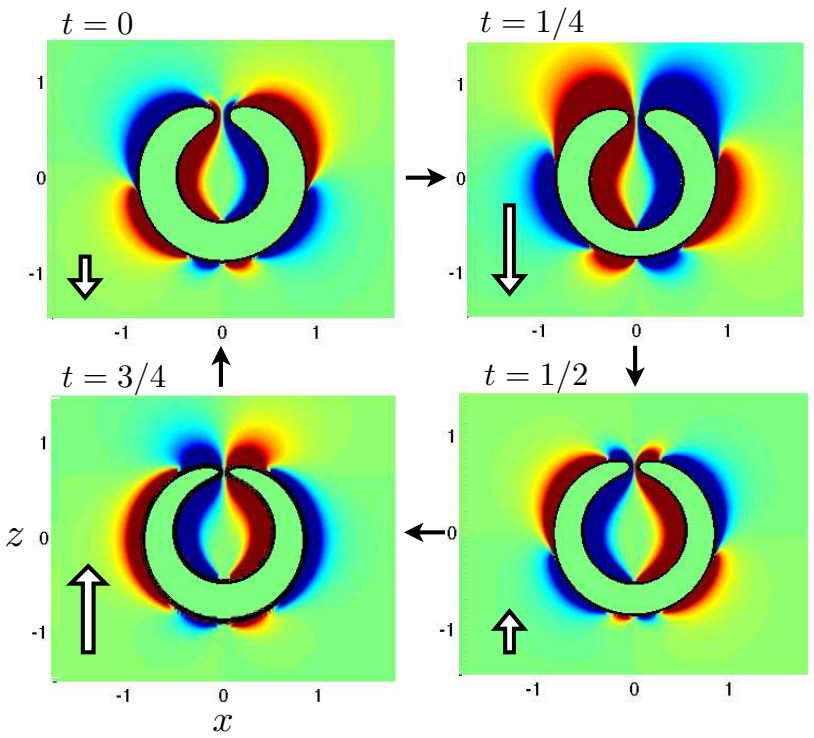

Figure 4.6: (color online) Stomatocyte shapes and vorticity profiles produced using the spontaneous curvature model, with $v(t) = 0.425 + 0.125\cos(2\pi t)$, $c_0(t) = -0.1 + 0.3\sin(2\pi t)$. Positive vorticity, corresponding to counter-clockwise rotation, is shown in red, and negative vorticity, corresponding to clockwise rotation, is shown in blue. Hollow arrows indicate the instantaneous swimming velocity. During one cycle, the vesicle experience net locomotion in the $-\hat{\mathbf{z}}$ direction.

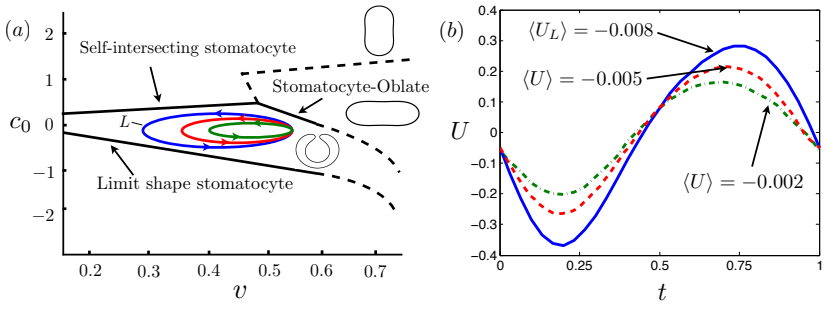

Figure 4.7: (color online) (a) Phase diagram for the spontaneous curvature model in the (v, c_0) parameter space. Solid lines are our numerically-calculated lines that denote morphological transitions, while the dashed lines are qualitative, and adapted from Ref. [128]. (b) Three velocity profiles, corresponding to the elliptic paths through parameter space indicated in (a), with the largest velocities achieved along the elliptic path enclosing the greatest area.

regions of phase space corresponding to prolate or oblate vesicle shapes cannot yield a net motion. However, paths which correspond to stomatocyte or pear shapes are fore/aft asymmetric and can swim. Since the area in phase space that contains pear shapes is very small, we will only examine the swimming stomatocytes. The largest elliptic path shown in Fig. 4.7a corresponds to the shape cycle shown in Fig 4.6. The associated time-evolution of the vesicle center of mass velocity is shown in Fig. 4.7b, along with two other velocities corresponding to elliptic paths enclosing smaller areas in Fig. 4.7a.

We see in Fig. 4.7 that the larger the area of the cycle in parameter space, the faster the vesicle swims. In fact, the mean velocity roughly scales as the square-root of the area enclosed by the elliptic path of phase space. Drawing on an analogy with thermodynamics, cycles with larger area in the appropriate ensemble space do more work, and thus we might expect that the transduction of shape deformation into mechanical work would exhibit similar behavior. Although our equivalent to an equation of state is too complicated to show a simple relationship between swimming velocity and the area enclosed in this phase space, the basic idea appears to remain valid.

We finally note that the net translation during each shape cycle in each case is small compared to the amplitude of the motion, and even smaller when compared to the maximum vesicle radius. The swimming velocities and hydrodynamic efficiencies of shape cycles in the spontaneous curvature model are also small. The maximum velocity achieved for the cycles shown is $\langle U \rangle = -0.008$, while we calculate an efficiency of $\eta_H = 0.4\%$.

4.8.2 Bilayer coupling model

We now consider the bilayer coupling model, for which a schematic phase diagram is shown in Fig. 4.8a. Although in the spontaneous curvature model there are no continuous transitions between oblate and stomatocyte shapes, the interesting feature of the bilayer coupling model is the presence of a continuous stomatocyte-oblate transition. The upper (solid) line in Fig. 4.8a denotes a limit line between oblate and prolate shapes, while the lower (dashed) line represents a

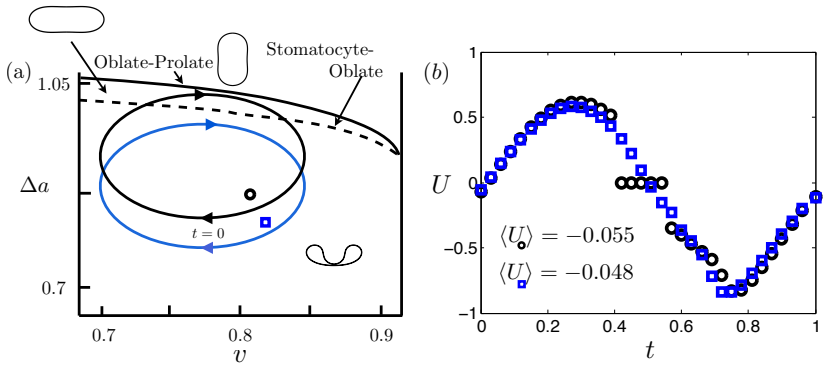

Figure 4.8: (color online) (a) Phase diagram for the bilayer coupling model in the $(v, \Delta a)$ parameter space, adapted from Ref. [128]. The dashed line indicates a continuous transition, while the solid line indicates a limit shape. Both lines are shown schematically in order to exaggerate the difference between the shape cycles. The two elliptical cycles considered enclose the same area in phase space, but one crosses the transition line. (b) Swimming velocity of the vesicle as a function of time, for the two shape cycles shown in (a). The squares denote the continuously varying velocity of the lower cycle in (a), which is similar to what we observed for the spontaneous curvature model. The circles correspond to the upper cycle in (a) and involves a shape transition, and there is a portion of the cycle during which the vesicle has zero swimming velocity due to fore-aft symmetry.

continuous transition between stomatocyte and oblate shapes.

In order to examine how breaking or restoring oblate ($\ell = 2$) symmetry relates to swimming, we now consider two shape cycles with equal enclosed area in phase space, as shown in Fig. 4.8a. The upper cycle crosses the continuous transition line, while the lower cycle remains in the stomatocyte region.

The vesicle shapes in the lower cycle of Fig. 4.8a are displayed in Fig. 4.9. They correspond to a modulation of the volume and surface area difference between monolayers for the vesicle as $v(t) = 0.775 + 0.075\sin(2\pi t)$, $\Delta a(t) = -0.14\cos(2\pi t) + 0.86$. From $t = 0$ to $t = 1/4$ the vesicle volume is increasing, expelling fluid from the cavity and pushing fluid away from the surface of the membrane. Due to the larger amount of surface area facing the aft end of the vesicle, the net motion during this quarter-cycle is forward. From $t = 1/4$ to $t = 1/2$, the "lobes" of the vesicle move downwards, propelling the vesicle upwards, albeit at a decreasing rate. This portion of the motion resembles the characteristic undulatory shape of a jellyfish, albeit one at zero Reynolds number. Between $t = 1/2$ and $t = 3/4$, the vesicle

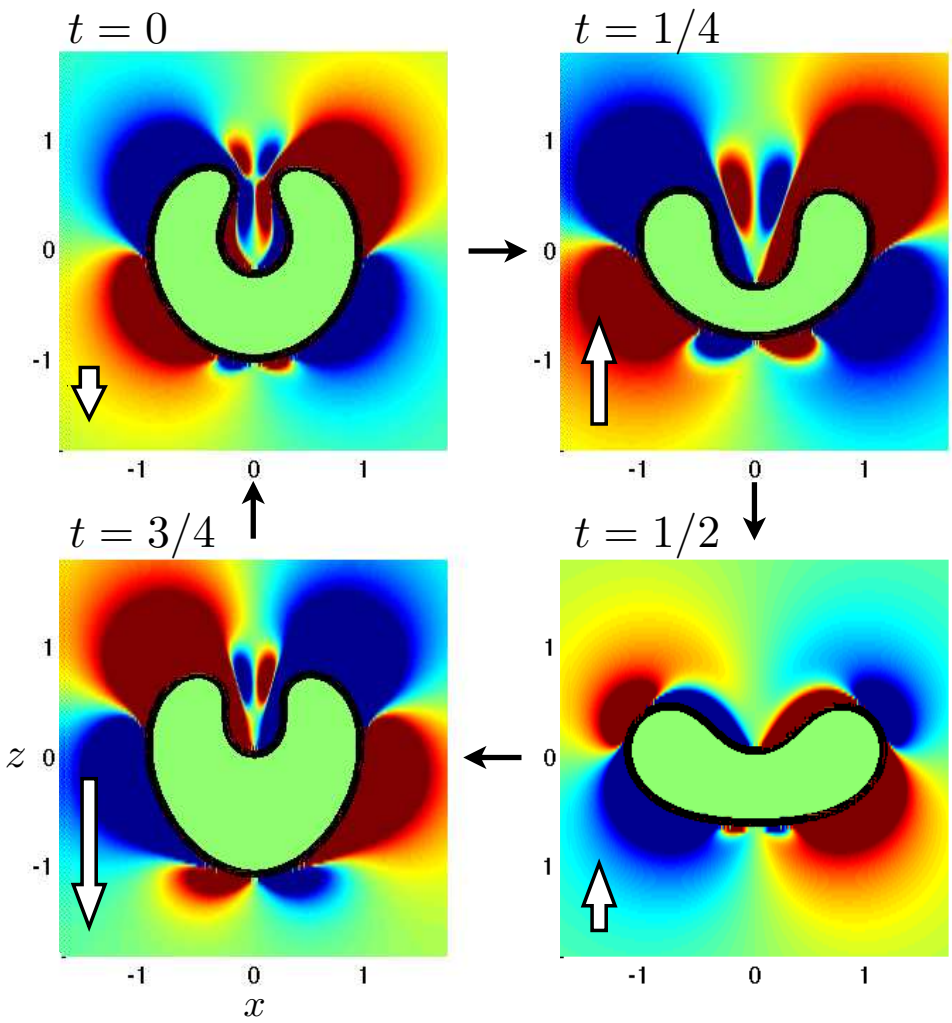

Figure 4.9: (color online) Vesicle shape cycle using the bilayer coupling model, with $v(t) = 0.775 + 0.075\sin(2\pi t)$, $\Delta a(t) = -0.14\cos(2\pi t) + 0.89$, corresponding to the lower cycle of Fig. 4.8a. This vesicle does not change morphological symmetry states during the swimming cycle and remains within the stomatocyte domain. Hollow arrows denote the instantaneous swimming velocity.

deflates and the lobes begin to move upwards again, with the material points of the lobes moving almost completely tangentially to the surface. This creates a vortex dipole at the lobes, leading to the stagnation point that can be seen in the figure. Finally, in the last quarter cycle, the vesicle encloses itself and returns to the starting position. We calculate a mean swimming velocity of $\langle U \rangle = -0.048$, and a hydrodynamic efficiency of $\eta_H = 0.6\%$.

The upper elliptical cycle of Fig. 4.8a, with shapes illustrated in Fig. 4.10,

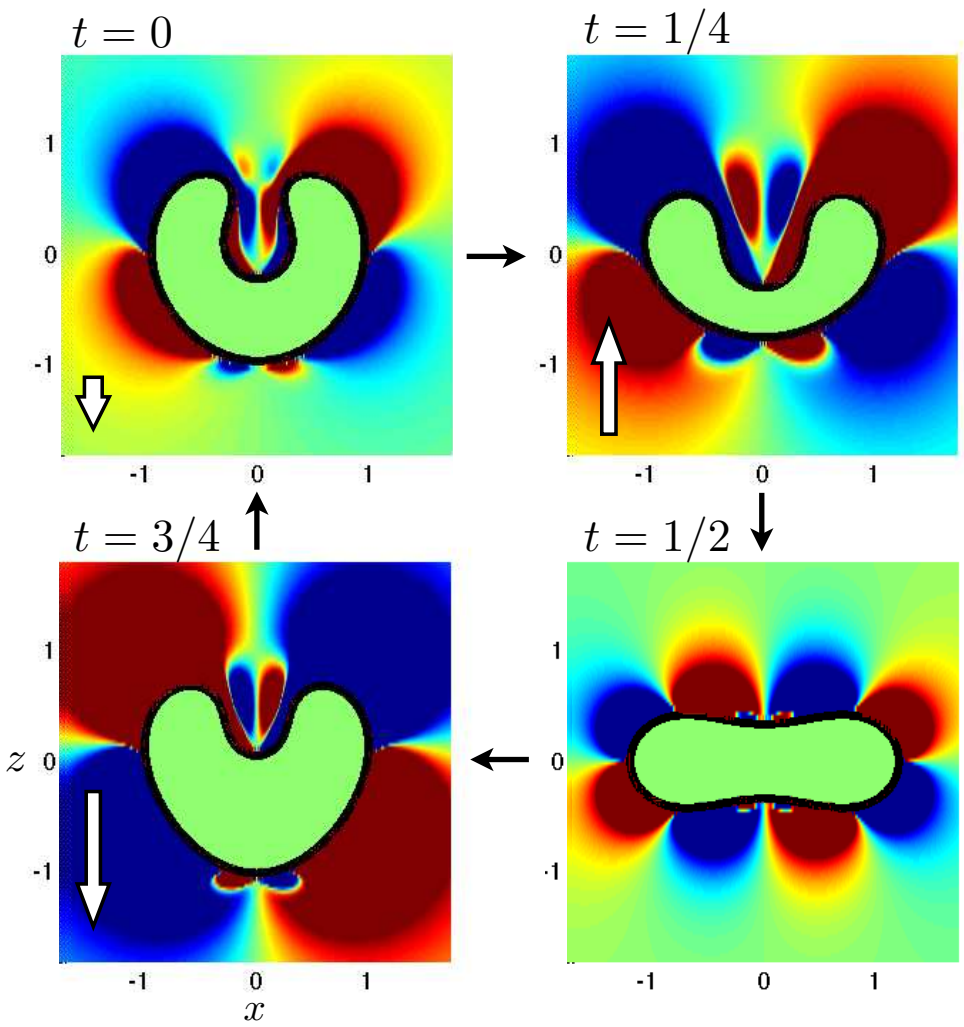

Figure 4.10: (color online) Vesicle shape cycle using the bilayer coupling model across a continuous phase transition, with $v(t) = 0.775 - 0.075\sin(2\pi t)$, $\Delta a(t) = 0.14\cos(2\pi t) + 0.89$, and corresponding to the upper cycle of Fig. 4.8a. This vesicle is oblate for a small part of the cycle, precluding swimming by symmetry, but a net locomotion occurs over the entire cycle. Hollow arrows denote instantaneous swimming velocity.

follows the parameter path $v(t) = 0.775 + 0.075\sin(2\pi t)$, $\Delta a(t) = -0.14\cos(2\pi t) + 0.89$, which lies above the continuous stomatocyte-oblate phase transition line from $t \approx 0.45$ to $t \approx 0.55$. During this portion of the cycle the vesicle has exactly zero swimming velocity due to the fore/aft symmetry of oblate shapes. Between $t = 0$ and $t = 1/4$, the volume and area difference are decreasing, leading the nearly oblate shape into a clearly stomatocyte configuration. For our purposes,

we will not address the spontaneous symmetry breaking that is associated with crossing a transition line, but simply assume that once broken, the cycle will break the symmetry in the same way during each cycle. In the example shown, the stomatocyte inflates as it assumes a more oblate shape, expelling fluid from the cavity and producing vorticity along the lobes. As the vesicle continues to deflate from $t = 1/4$ to $t = 1/2$, the lobes sweep downwards, moving the stomatocyte upwards as it assumes a perfectly oblate shape. At $t \approx 0.42$ the shape transitions into an oblate shape, precluding any net swimming by symmetry. The swimming velocity as a function of time is shown in Fig. 4.8b. As the oblate vesicle deflates, at $t \approx 0.58$ the stomatocyte symmetry state is entered once more, the lobes sweep upwards, and the vesicle moves downwards. Despite the presence of a becalmed period during the vesicle does not move, the cycle that involves the shape transition yields a larger mean velocity than the lower cycle, $\langle U \rangle = -0.055$, and an increased hydrodynamic efficiency, $\eta_H = 0.7\%$.

As previously noted, crossing the shape transition line between stomatocyte and oblate shapes indicated in Fig. 4.8a yields a continuous shape change. However, if we exploit the analogy with phase transitions, we note that some quantities must be discontinuous across the transition. Without exploring the details of a dynamic phase transition in the context of vesicle locomotion, although the order parameter is continuous, derivatives of the order parameter need not be so. In other words, the material at a given point s along the boundary experiences a continuous positional change, but a discontinuous velocity relative to the center of mass of the body as the parameters are varied continuously through the transition line. The discontinuous relative material velocity then generates the discontinuous swimming velocity seen in Fig. 4.8b for the body which exhibits the oblate shapes for part of its periodic cycle.

Interestingly, even though the area enclosed in phase space by the two cycles illustrated in Fig. 4.8a is the same, the relationship between parameter space, efficiency, and swimming velocity is not evident. The upper cycle shown in Fig. 4.10 has a larger mean swimming speed and is more efficient than the cycle shown Fig. 4.9, suggesting that the vesicle can increase its efficiency by passing

through a phase transition.

4.9 Discussion

In this paper, we have shown computationally that it is possible for a bilayer vesicle to swim under a prescribed shape change using two different vesicle models. By modulating the vesicle volume and either its preferred curvature (spontaneous curvature model) or the surface area difference between membrane monolayers (bilayer coupling model), the vesicle can be made to undergo deformations which are not time-reversible, yielding therefore a net swimming motion. Net locomotion can be obtained either by continuously modulating fore-aft asymmetric vesicle shapes (stomatocytes), or by crossing a continuous shape-transition region with fore-aft symmetric shapes, and alternating therefore between fore-aft asymmetric and fore-aft symmetric shapes.

At first sight, the swimming efficiencies obtained in this paper appear to be low. For the swimming stomatocyte shown in Fig. 4.7, the efficiency is on the order of 0.4%, while for the bilayer coupling model we calculate an efficiency of 0.6% for a non-transitioning vesicle, and 0.7% for a vesicle that undergoes a transition from stomatocyte to oblate. However, it is known from many theoretical studies that the hydrodynamic efficiency of swimming microorganisms, such as flagellated bacteria or spermatozoa, is on the order of 1 to 2% (see Ref. [10] and references therein). Our results indicated therefore that the equilibrium morphologies of bilayer vesicles, together with their appropriate modulations as is done in this paper, lead to locomotion means which are almost as efficient as those displayed by biological cells, and might therefore provide an interesting alternative to flagella-based synthetic micro-swimmers. Further optimization of the size and shape of cycle in parameter space will likely lead to swimming vesicle outperforming the efficiency of flagellated cells. In addition, a swimming vesicle has the advantage that the swimmer and the cargo can be one and the same.

Let us now discuss the typical time and velocity scales obtained in our simulations. A typical vesicle size is approximately 10 μm, and for liposomes $\kappa \approx 10^{-19}$

Nm. Except for very curved vesicles, the typical radius of curvature r_0 is approximately 10 μm as well, leading to a velocity scale of 10 μm/s. This gives calculated mean velocities on the order of 0.1 μm/s for the spontaneous curvature model, and 0.5 μm/s for the bilayer coupling model. Translational and rotational diffusion constants for vesicles this size at room temperature are $D \approx 10^{-14}$ m^2/s and $D_r \approx 10^{-3}$ s^{-1}, respectively. This implies a time scale for translational diffusion of approximately 10^4 s, and a time scale for diffusive reorientation of approximately 10^3 s. Since the actuation proposed in this paper can be implemented faster than both of these time scales, significant diffusion will take place only after many actuation cycles. For time scales much larger than D_r^{-1}, the effective vesicle diffusion will then be given by $D_{eff} \approx U^2/D_r$ [8], which accounts for both swimming and orientation loss. The ratio $D_{eff}/D \approx 10^3$ is large, which implies that locomotion will lead to a substantially enhanced diffusion of the vesicles over long time scales.

We have considered only two minimal models for vesicle shape change, and many possible avenues exist to expand upon this basic model, including a study non-axisymmetric vesicles, more advanced curvature models, and arc length-dependent spontaneous curvature. Since we have assumed a quasi-static deformation, non-equilibrium effects would also have to be taken into account for fast deformations, and the shape should be fully determined as a balance between elastic and fluid forces. In addition, swimming is just one example of behavior that could be exhibited by a membrane that is actively deformed. It is perhaps the simplest transduction of geometrical deformation into mechanical work, and one that we hope provides further inspiration for the combined study of membrane physics and low Reynolds number fluid mechanics.

Acknowledgements

This research was funded in part by the NSF (grant CBET-0746285). This chapter is reproduced in part from material being prepared for submission and also from published material: A. A. Evans, S. E. Spagnolie, and E. Lauga, *Soft Matter*, 1737-1747, 2010.

Chapter 5

Collective locomotion

5.1 Introduction

Recent experiments on motile particles, from collections of microorganisms [131, 132, 133] to self-propelled colloids [101], exhibit pattern forming behavior and enhanced transport characteristics that pose fundamental questions for the nonequilibrium statistical mechanics of active systems [103], and have implications in bio- and nano-engineering. One area of interest concerns the hydrodynamics of microorganisms swimming in viscous fluids at zero Reynolds number [10].

Several methodologies have been developed to address the emergence of collective locomotion, basically corresponding to either microscopic or macroscopic formulations. Active hydrodynamic equations developed from a non-equilibrium kinetic theory has been the prevailing microscopic approach to the system [134, 11, 135, 136]. By modeling microswimmers as force-dipoles, these kinetic theories build continuum dynamical equations for fields quantifying the long-wavelength properties (density, orientation...) of suspensions of self-propelled particles. Obvious benefits of this approach parallel the advantages of statistical mechanics, in that large scale phenomena can be predicted by the proper construction of a system of microscopic evolution equations. The difficulty in dealing with interacting particles, however, leads to the necessity of a dilute assumption, and the lack of any specified structure to the microswimmers (self-propelled particles are represented as oriented point singularities).

At the other end of the spectrum, thermodynamic models of active media postulate the existence of phase separation due to relevant (allowed) terms in a dynamical equation, and as a result nonlinearities and coupled modes that cannot be derived from a dilute formulation are accessible [137, 138]. Coarse-grained models, while not specifying hydrodynamic interactions, implicitly include near-field effects that are not disallowed by symmetry. These "flocking" models include many possibilities for ordered states that cannot be captured by the microscopic models, at the expense of introducing phenomenological parameters that may be difficult to explain physically and derive from microscopic considerations [103].

In this paper we use a specific model microswimmer (usually referred to as a "squirmer" [139]) to address global orientational and spatial order compu-

tationally. With our approach both semi-dilute and concentrated suspensions of spherical swimmers can be considered, allowing both to probe dynamics beyond the dilute regime and to compare results with continuum theories made. Contrary to predictions from dilute continuum theories, we find that isotropic suspensions of spherical swimmers are unstable, and evolve dynamically to take on a long-time state of global order. This state of polar order exists in phenomenological flocking models, and is thus shown here to arise from hydrodynamic interactions. A marked asymmetry between pusher and puller swimmers is further shown, which is interpreted to be due to the short-range details of the flow field induced by the active particle. After proposing a physical mechanism behind the polar ordering, we finally examine the behavior of close-packed suspensions.

5.2 Model system

We simulate a system of N squirmer in a cubic box of volume L^3, where the size of the box L is determined from the number of swimmers and preset volume fraction v. The details of the modeling approach can be found in Ishikawa et al. (2006) [139]. The infinite extent of the system is expressed by applying periodic boundary conditions. A squirmer, as defined originally by Lighthill [140] and used subsequently by Blake to model ciliary propulsion [141] is a spherical particle that has a prescribed axisymmetric velocity distribution on its surface. In the case of the swimmer that is used in our model, we impose $u_\theta(\theta) = B_1 P_1(\cos\theta) + B_2 P_2(\cos\theta)$, where P_n is the n^{th} Legendre polynomial. The angle $\theta = 0$ defines the direction, denoted $\mathbf{e}$, in which the squirmer swims, with swimming speed (for a solitary squirmer) $U \sim B_1$ [141].

Fluid disturbances in the far field are governed by the "stresslet" (or force-dipole) of the organisms, quantified by the dimensionless quantity $\beta = B_2/B_1$. Indeed, the stresslet of a swimmer governs not only the far field decay of velocity fluctuations, but also the physical characteristics of the thrust generation. Some organisms, like the algae *Chlamydomonas*, generate thrust in front of their bodies using a pair of flagella, pulling themselves therefore through the fluid. On the

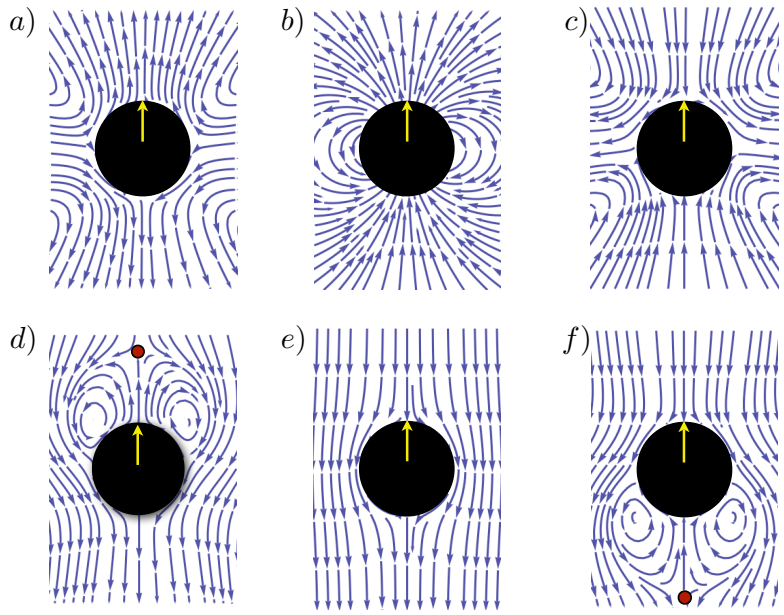

Figure 5.1: Flow streamlines of isolated squirmers for various values of β. Flow streamlines in the swimming frame (top; a to c) and lab frame (bottom; d to f). Left (a and d): Pusher with a negative stresslet ($\beta = -5$), generating thrust at the aft region. Center (b and e): Potential flow developed by a squirmer with $\beta = 0$. Right (c and f): Puller with a positive stresslet ($\beta = +5$) generate thrust at the fore area. In the lab frame, squirmers with $\beta \neq 0$ develop a stagnation point off the body; for pushers (d) this point leads the swimmer, while for pullers (f) this point trails.

other hand, most flagellated cells such the bacteria *E. coli*, or spermatozoa, generate thrust behind them, and instead push themselves through the fluid. Using our modeling approach, "pullers" are characterized by $\beta > 0$, while "pushers" correspond to $\beta < 0$. The flow field decays as β/r^2 far from the swimmer, and – in the absence of thermal fluctuations [142] – the stresslet dominates the long-range interactions. This difference in hydrodynamic signature between pushers and pullers has been addressed at length by dilute theories [11, 134, 10, 136].

The velocity of an isolated microswimmer is fixed, dimensions are scaled such that $U = 1$; the only free parameter characterizing isolated swimmers is therefore the dimensionless stresslet β. In the presence of multiple swimmers, their instantaneous velocities and rotation rates are calculated by enforcing the condition of force- and torque-free swimming. The computational approach is

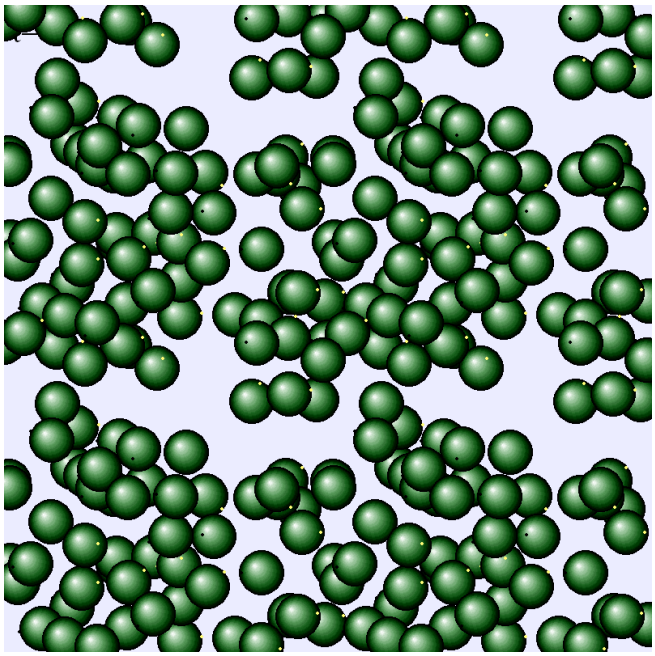

Figure 5.2: A snapshot of a simulation with $v = 0.1$, $\beta = 1$ (pullers), and $N = 64$ squirmers. The figure shown has the computational cell in the middle, with identical copies surrounding this periodic box. Dark dots on the squirmers represent the rear (i.e. $\theta = \pi$), while light dots represent the swimming direction, $\theta = 0$.

based on Stokesian dynamics, with an analytical treatment of lubrication forces for closely separated swimmers, as well as additional short-range repulsive forces to prevent particle overlap, as described in detail in Refs. [139, 143].

The two parameters characterizing the collective swimming dynamics are thus the swimmer volume fraction, v, and the swimmer stresslet, β. In order to probe, as function of both v and β, the development of order in our system, we define an order parameter, P, based on the orientation vector $\mathbf{e}$ of the particles, namely $P(t) = |\sum_i^N \mathbf{e}_i(t)|/N$. If every particle is swimming in the same direction (polar order) then $P = 1$, while for isotropic orientation we expect $P \sim 1/\sqrt{N}$.

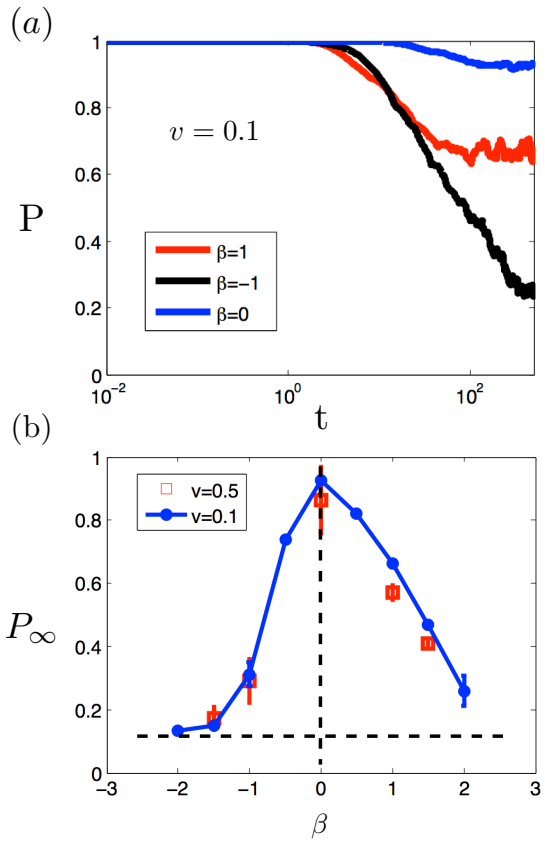

Figure 5.3: Global order of semi-dilute and concentrated suspensions of pushers and pullers starting from polar (aligned) state. (a): Representative evolution in time for the order parameter, $P(t)$, for pushers ($\beta = -1$), pullers ($\beta = 1$), and potential swimmers ($\beta = 0$). Each simulation starts from an initially aligned state (with random positions) and decays to a finite order, P_∞, after a characteristic decay time that depends on the stresslet coefficient β. (b): Long-time order parameter, P_∞, for initially aligned suspensions. Each data point represents an average not only over an ensemble (in this case five separate realizations), but also over time. The time-averaging was performed during the period after the initial decay from alignment until the end of the simulation. Error bars represent standard deviations of the ensemble averaging process. We observe a decrease order with increasing value of β, and an asymmetry between pushers and pullers. The order is only weakly affected by the volume fraction up to $v \sim 0.5$.

5.3 Stability and long-time order: Aligned suspensions

We will first inquire whether certain pathological conditions persist over time. Namely, beginning from a state of order, will the system be driven to

disorder? In contrast, can the activity of a suspension cause an initially disordered system to spontaneously generate orientational order? In the dilute limit, continuum theories for slender self-propelled rods have predicted that aligned suspensions are always unstable, while isotropic states are only unstable for pushers ($\beta < 0$) [11, 135]. The physical nature of this instability is described as resulting from long-range hydrodynamic extensional disturbances that cause reorientation of anisotropic particles, but to which spherical swimmers are immune. In the dilute limit, no instability due to long-range hydrodynamic interactions is thus expected to occur for spherical particles [11, 134].

In Fig. 5.3a we plot the time-evolution of the polar order $P(t)$ for aligned suspensions with three different stresslet values, $\beta = -1$ (pusher), 0 (potential swimmer) and $+1$ (puller). The initial positions of the swimmers are taken to be random. Over the semi-dilute to concentrated range of volume fractions, $v = 0.1 - 0.5$ (the results in Fig. 5.3a are shown for $v = 0.1$), we observe the system to systematically decay from perfect order ($P = 1$) to some finite long-time value ($0 < P_\infty < 1$). The decay time over which the suspension is driven to this new ordered state depends on the stresslet value β, and larger values of the stresslet disturb the fluid more violently, causing reorientation, and loss of polar order, more quickly; β can thus be interpreted as the speed at which orientation decorrelation propagates throughout the suspension.

To further characterize long-time order, we perform ensemble averages on five realizations of our simulation, starting with an aligned orientations and random positions, for volume fractions in the range $v = 0.1$ to 0.5 and stresslets varying from $\beta = -2$ to $+2$. Upon doing ensemble averages, we define a long-time order parameter P_∞. The results are shown in Fig. 5.3b. In the range of volume fractions studied, we observe that the long-time order is independent of the value of v, but it strongly depends on the value of the stresslet β. Larger values of $|\beta|$ lead to increased swimmer-swimmer reorientations due hydrodynamic interactions, and thus lead to decreased values of P_∞. In addition, we observe a marked asymmetry between pushers and pullers, and for a given value of $|\beta|$, pullers are systematically more ordered. This is in contrast with analytical predictions in the dilute limit

where suspensions of pullers are expected to be driven to isotropy [11].

What governs the emergence of long-time global order, and why is there an asymmetry between pushers and pullers? It has been suggested in the past that near-field interactions are the dominant mechanism for global ordering [143]. To address the pusher-puller asymmetry, we take a detailed look at the flow field near the swimmers. The difference between a pusher and a puller, which in the far-field leads to a change of sign in the hydrodynamic perturbation to the environment, leads in the near-field to a change in the location of the flow stagnation point. This is illustrated in Fig. 5.1: for a pusher this stagnation point leads the swimmer, while for a puller it trails it. This hydrodynamic asymmetry causes the different collisional situations (head to head, head to tail, and tail to tail) to produce different reorientations between pushers and pullers. From previous numerical work, it is known that head-to-head interactions are far more likely to occur [144]. For pushers the head-to-head orientation is stable to near-field torques. This can be understood from the sign of the vorticity in the near-field flow around the squirmer (see Fig. 5.1d and f): the presence of a stagnation point establishes vortices near the surface of the swimmer, and in a head to head collision both pairs of vortices will interact in a manner as to maintain this orientation. Pullers, on the other hand, are unstable in this configuration, as their vortices trail in such a collision. In terms of contributing to order, head to head orientations yields $P \sim 0$, and thus any instability of this configuration, as expected for pullers, will lead to an increase of global order.

5.4 Stability and long-time order: Isotropic suspensions

While it is not surprising to find that aligned states of swimmers are unstable, the dynamics of isotropic suspensions remain to be evaluated. Instability in isotropic suspensions is predicted to exist only for pushers, and only then when the swimmers have an elongated shape [11]. Instability of isotropic suspensions has been observed previously in simulations of semi-dilute systems [143], but it

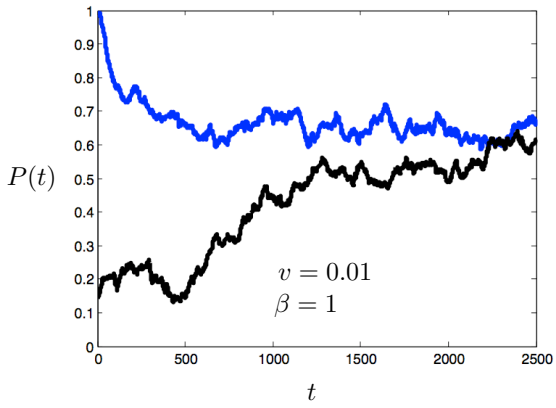

Figure 5.4: Representative data comparing initially aligned and isotropic suspensions. Aligned initial conditions have random spatial positions of the swimmers, while isotropic has randomized position as well as orientation. For $v = 0.01$, both aligned and isotropic states are unstable (data shown for $\beta = 1$). Over time both systems approach the same final state.

is not immediately obvious whether this behavior is purely due to volume fraction considerations or the inclusion of specific near-field interactions. Squirmers may have a particular orientation behavior in the near-field, but in dilute suspensions the long-range hydrodynamics should dominate the dynamics. Figure 5.4 shows a representative time series for suspensions of pullers at low volume fraction (v=0.01), for both aligned and isotropic initial conditions (similar results exist for pushers). Both sets of initial conditions are unstable, as the hydrodynamic interactions drive the system to an intermediate value of the order parameter. The time scale over which the instability takes place is very long compared to more concentrated suspensions, and it is certainly the case that in the limit that $v \to 0$ the instability would disappear. More interesting than the mere presence of the instability, however, is the existence of a shared state of global order at long times.

If the near field interactions are indeed responsible for the order that develops, even in dilute suspensions, how does increasing the volume fraction affect this order? In dispersions of colloidal particles, novel phase behavior and dynamics are observed as the volume fraction of the system is increased [145, 146, 147]. Particles have less room to maneuver, restricting their ability to sample all of phase space, and possibly complicating any kind of thermodynamic phenomena exhibited by

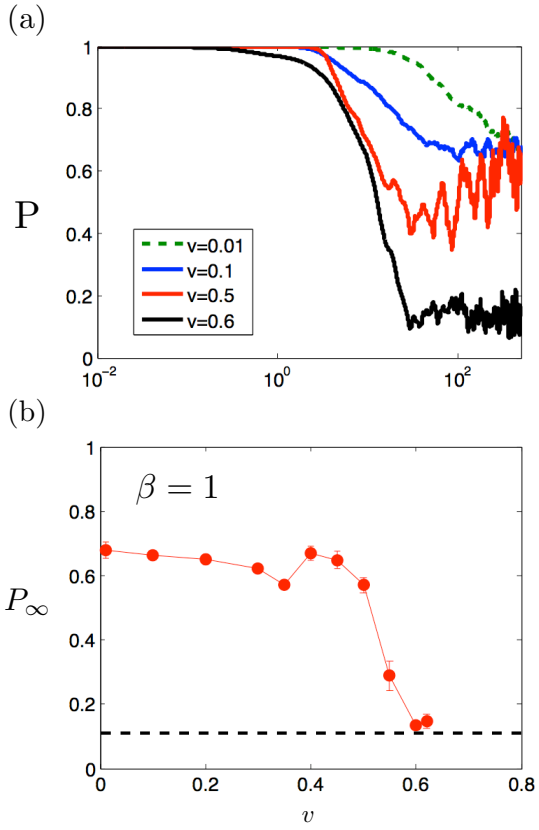

Figure 5.5: Polar order as function of volume fraction. a) Samples of order decay for pullers ($\beta = 1$). As the volume fraction increases, the magnitude of fluctuations increases dramatically. b) Long-time order as a function of volume fraction, for pullers ($\beta = 1$). For relatively dilute suspensions there is only a weak dependence on the volume fraction. At larger volume fractions the order drops sharply to isotropy (indicated by dashed line). Error bars are standard deviation over many realizations.

the suspension. By simulating a system of particles that both occupy space and have an active direction of locomotion we can probe the specifics of how increasing volume fraction destabilizes orientational order of the suspension.

Figure 5.5a displays representative time series for different volume fractions of pullers. As the volume fraction increases the long-time order only changes weakly, but as the simple cubic packing limit is approached ($v_{sc} \sim 0.52$) fluctuations in the order get larger, until finally the order disappears (see Fig. 5.5b). Pushers display a similar dependence, although with decreased magnitude due to the asymmetry noted earlier.

The average value of P_∞ changes only slightly over a wide range of volume fractions, but the magnitude of the fluctuations in the order increases enormously. Given that near-field interactions are the likely culprit for causing the order to develop in the first place, why is it that above a certain volume fraction the order vanishes? What significance does close-packing have on the orientation of the particles?

At low volume fractions the rate of collisions between swimmers, and thus the frequency of near-field interactions, is much lower than in the concentrated limit. The physical asymmetry between pushers and pullers, combined with the statistical likelihood of certain collisions combine to yield the long-time asymmetry between the two species of swimmers. For close-packed suspensions, however, the frequency of near-field interactions increases dramatically, and collisions from all angles become more likely.

5.5 Orientation distribution

Quantifying the global order in the system may show that a particular direction is preferred, but there is no information in the value of P or P_∞ that characterizes the spatial distribution of swimmers; in a continuum model we could define a director field $\mathbf{n}$ that varied throughout space. As it is, the spatial distribution of the order in our system can be measured by defining the correlation function $C(r) = \sum_{i \neq j} \mathbf{e}_i \cdot \mathbf{e}_j$ where the i^{th} particle is a distance r from the j^{th} particle. Figure 5.6 displays this correlation for several volume fraction values, contrasting the semi-dilute case with the highly concentrated, for both pushers and pullers.

Pullers show stronger correlations than pushers at all distances, as could perhaps be expected from comparing the value of the order parameter. For pullers there is also a distinctive similarity with the radial distribution function of the suspension, indicating that there is a strong connection between the density of the particles and their orientation correlation. Strangely, pushers indicate no strong dependence on spatial distribution, but show an isotropic preference for slight

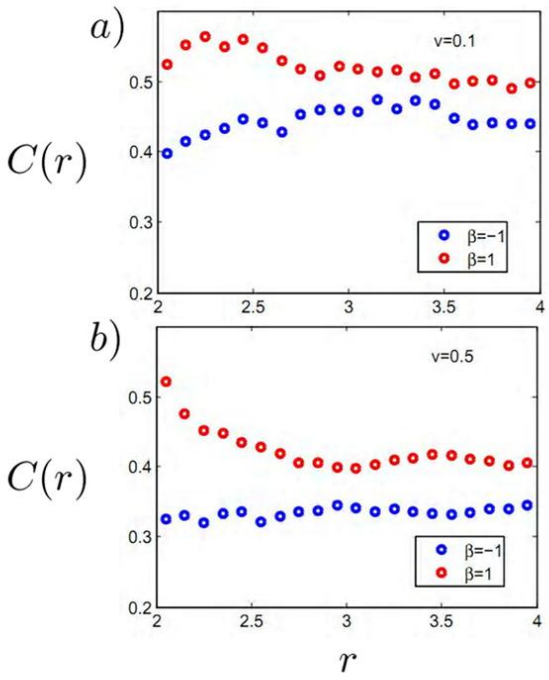

Figure 5.6: Correlation functions for pushers and pullers as a function of distance, at concentrated volume fraction. a) At low volume fractions there is an isotropic tendency for correlation at several particle radii away ($r > 3a$), with pullers more correlated everywhere as compared to pushers. b) At high volume fractions, pullers are correlated most strongly with their nearest neighbors, followed by a peak at $r \sim 3.5$. There is, then, a spatial structure to the orientational order that is not completely dictated by the radial distribution function, possibly implying that hexagonally arranged squirmers have a higher correlation. Pushers on the other hand, while having minor variations in space, appear to have no strong spatial links to the correlation.

correlation. The slight peak for pullers at $r \sim 3.5$ is puzzling in that it does not correspond to short-range order, which for molecular liquids occur at integral spacings with regard to the particle size (i.e. $r = 2a$,$r = 4a$,etc.). A peak at $r = 2\sqrt{3}$ would indicate a next-nearest neighbor correlation in the case of a hexagonally close-packed system, but for a suspension lacking long-range order it is surprising. The best explanation once again probably lies in the presence of vortices near the surface of the squirmers; there will be a preferred angle at which the squirmers will align more strongly, and the bias that this angle gives will set up a structure

to the order in the suspension. It cannot be overstated how interesting it is to have a fluid-ordered suspension, displaying isotropic distribution in the far-field, yet containing ordered spatial structure in the orientation.

The existence of spatial structure demands further exploration of the properties of high volume fraction dynamics, and the avenues of research are far too numerous to be included here in any comprehensive fashion. However, in granular media there is the ever-present specter of ergodicity-breaking, jamming, and glassy dynamics that are all associated with an increasing volume fraction of particles. While our suspensions of squirmers may be athermal, is there any link that we can provide between these very different kinds of systems? There is evidence in jammed systems that above a certain external stress/strain the particles can flow, exhibiting fluidized behavior only in the presence of this external source. Our system contains active particles each of which has it's own ability to generate motion. Is there an analogy between the global effect of an external field and the local effects of internal stress states?

Lacking the room to maneuver unhindered throughout the system, individual particles at high concentration have restricted access to phase space; as a direct result, transient behavior becomes more important than in the semi-dilute case. Although there is an average value of P_∞ that is achieved for certain values of v and β, there are large fluctuations in this average value at high volume fractions (Fig. 5.7a). Frequent reorientations of individual squirmers due to the proximity of many neighbors means that there is the potential for orientational correlation to propagate very rapidly throughout the system. In Fig. 5.7b, different initial conditions for the same suspension ($v = 0.6$, $\beta = 0$) yield results that are drastically different over the time scale considered. While the decay time for the system is unaltered, lending credence to the idea that this decay time is β-dependent, the finite delay time indicates that particles are "trapped" in their initial conditions before finally escaping to the isotropic steady state.

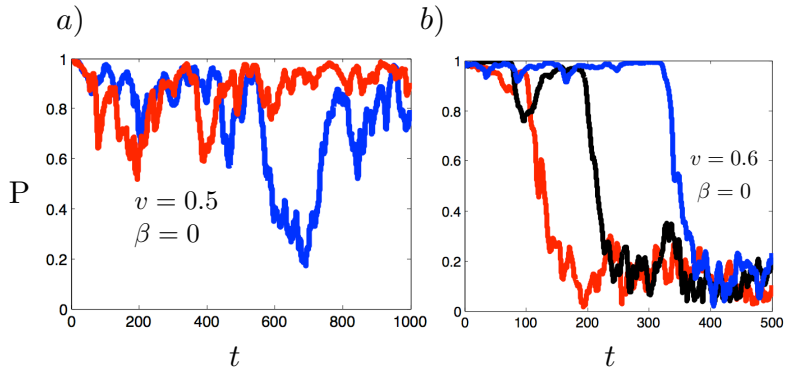

Figure 5.7: High volume fraction shows large fluctuations and transient behavior. a) Although the long-time average over many ensembles converges to a single value, the fluctuations about this average become very large with high volume fraction. Shown here is an example of two suspensions, both at $v = 0.5$ and $\beta = 0$, but with different initial positions. The order fluctuates around the average value near $P = 1$, but there are large jumps down to near isotropic orientation. b) Above $v \sim 0.55$, the order is eventually driven to isotropy, no matter the magnitude of the stresslet, but this transition has an associated delay time. Individual swimmers have difficulty negotiating their surroundings, and thus there is a transient period before the system is driven out of the aligned state. Note that the decay time does not change, as it is dependent on the value of β, but the delay is most likely associated with an inability to sample all of phase space.

5.6 Discussion

While our results for instabilities are by no means a general statement about microswimmers, there are several key points to note. Firstly, even lacking thermal fluctuations, and without the anisotropic geometry inherent in slender swimmers, the spherical squirmers of our simulations develop polar order due to interactions. Secondly, these interactions depend on the nature of the swimmer, i.e. pusher vs. puller. It is entirely possible that the near-field interactions dominate the system dynamics, but even if this is the case, real swimmers have near-field interactions, and although a squirmer is only a simple model it is the next step beyond a pure dipole. Having taken this next step, we see that there is indeed non-trivial differences with the dilute, dipole continuum models, and that there are similarities in the computational results with the phenomenological flocking models.

There is much to be gained from knitting together the disparate theories

for collective locomotion of microorganisms. A general theory for non-equilibrium statistical mechanics is elusive, and by utilizing systems of living fluids as a case study for exploring order in active suspensions we can fill in the many gaps in our understanding. Even suspensions of colloidal particles in thermal equilibrium display complicated behavior when the granularity and packing of the system becomes relevant; by including activity at the level of single particles, this system becomes even more complex. Using our computational model we hope that we can form a bridge to discuss in detail the separate regimes of validity of differing models, illuminate how hydrodynamics influences global order, and further pursue the consequences involved with collective interactions.

Acknowledgements

This chapter is reproduced in part from material being prepared for publication with Takami Yamaguchi and Takuji Ishikawa.

Appendix A

Vesicle-fluid dynamics

The swimming velocity is computed at each time by solving a standard boundary integral formulation of the Stokes equations. As an application of the Lorentz reciprocal identity, the solution to Eqs. (4.30) may be written as integrations upon the surface velocity and the fluid stress,

$$\mathbf{u}(\mathbf{x}) = \frac{1}{8\pi\mu}\int_{S(t)} \mathbf{G}(\mathbf{x},\mathbf{y})\cdot(\boldsymbol{\sigma}(\mathbf{y})\cdot\hat{\mathbf{n}}(\mathbf{y}))\; dS_y + \frac{1}{8\pi}\int_{S(t)} \mathbf{u}(\mathbf{y})\cdot\mathbf{T}(\mathbf{x},\mathbf{y})\cdot\hat{\mathbf{n}}(\mathbf{y})\, dS_y \tag{A.1}$$

where

$$\mathbf{G}_{ij}(\mathbf{x},\mathbf{y}) = \frac{\delta_{ij}}{|\mathbf{x}-\mathbf{y}|} + \frac{(x_i-y_i)(x_j-y_j)}{|\mathbf{x}-\mathbf{y}|^3}, \tag{A.2}$$

$$\mathbf{T}_{ijk}(\mathbf{x},\mathbf{y}) = -6\frac{(x_i-y_i)(x_j-y_j)(x_k-y_k)}{|\mathbf{x}-\mathbf{y}|^5}, \tag{A.3}$$

are the singular Stokeslet and Stresslet tensors, respectively (see Ref. [148]). By introducing a complementary flow $\mathbf{u}'$ which has the same values of the surface force $\boldsymbol{\sigma}\cdot\hat{\mathbf{n}}$ as the flow $\mathbf{u}$ on the surface $S(t)$, Eq. (A.1) may be written solely in terms of the second, double-layer integral,

$$\mathbf{u}(\mathbf{x}) = \int_{S(t)} \mathbf{q}(\mathbf{y})\cdot\mathbf{T}(\mathbf{x},\mathbf{y})\cdot\hat{\mathbf{n}}(\mathbf{y})\, dS_y, \tag{A.4}$$

where $\mathbf{q}(\mathbf{x})$ is an unknown density of the singular Stresslet tensor. In the limit as the $\mathbf{x}$ approaches the body surface $S(t)$, inserting the no-slip condition for the surface velocity there, we find the expression

$$\mathbf{U} + \mathbf{u_d}(\mathbf{x}) = \int_{S(t)} (\mathbf{q}(\mathbf{y}) - \mathbf{q}(\mathbf{x}))\cdot\mathbf{T}(\mathbf{x},\mathbf{y})\cdot\hat{\mathbf{n}}(\mathbf{y})\, dS_y. \tag{A.5}$$

The vertical swimming velocity $U = \mathbf{U}\cdot\hat{\mathbf{z}}$ is related to the Stresslet density as

$$U = -\frac{4\pi}{A}\int_{S(t)} \hat{\mathbf{z}}\cdot\mathbf{q}(\mathbf{x})\, dS \tag{A.6}$$

(recall that A is the vesicle surface area). Equation (A.5) is a well-posed Fredholm integral equation of the second kind for the unknown density $\mathbf{q}(\mathbf{x})$, and has a unique solution. This approach is numerically better conditioned than those based on first-kind equations.

The Stresslet integral operator in Eq. (A.5) has a six-dimensional nullspace corresponding to rigid body motion, and in the presence of external body forces or torques this representation must be closed by a range completion technique (see Ref. [149]). However, in the swimming problem where the deformation velocity $\mathbf{u_d}(\mathbf{x})$ is specified and there are no body forces or torques, Eqs. (A.5-A.6) are closed and prescribe uniquely the swimming velocity U.

The integrand in Eq. (A.5) is discontinuous at the singularity but finite, so that the integrals are computed to second-order in the surface mesh element size using a standard trapezoidal quadrature (setting the quadrature weight to zero at the singularity). The axisymmetry of the problem is inserted into the definition of the body surface as well as the density $\mathbf{q}(\mathbf{x})$. The number of gridpoints is chosen to be sufficiently large such that further resolution does not significantly alter the density $\mathbf{q}(\mathbf{x})$ or the swimming velocity U.

At each time, the curve $(r(s,t), z(s,t))$ is discretized uniformly in s. Application of a Nyström collocation method produces a linear system of equations for the density $\mathbf{q}(\mathbf{x})$ at the gridpoints, which is then solved iteratively using the method GMRES [150], with an inversion error tolerance such that the only errors are due to discritization. Finally, the body position $z_0(t)$ is updated at each time using a second-order Runge-Kutta method. Both convergence tests and comparison with known exact solutions were used to validate the code [151, 116, 152, 109].

Computing the hydrodynamic or swimming efficiency (which requires pointwise information about the stress $\boldsymbol{\sigma}$) is more difficult. Here we compute $\boldsymbol{\sigma}(\mathbf{x})$ using the approach outlined below, though a more detailed description of the method and examples of its use will be featured in a subsequent paper.

Many common methods for computing the stress are developed using a first-kind boundary integral formulation of the Stokes equations, and hence can suffer from the ill-posedness of the underlying equations [148]. Instead, we solve for the surface stress by evaluating a hypersingular integral which may be derived from the second-kind integral equation for the velocity (see Ref. [148]),

$$\frac{1}{\mu}\sigma_{im}(\mathbf{x}) = \int_S q_j(\mathbf{y})\mathcal{L}_{ijkm}(\mathbf{x},\mathbf{y})\hat{n}_k(\mathbf{y})\,dS_y, \tag{A.7}$$

where

$$\mathcal{L}_{ijkm}(\mathbf{x},\mathbf{y}) = -4\frac{\delta_{im}\delta_{jk}}{|\mathbf{x}-\mathbf{y}|^3} - 6\frac{(x_k-y_k)[\delta_{jm}(x_i-y_i)+\delta_{ij}(x_m-y_m)]}{|\mathbf{x}-\mathbf{y}|^5}$$
$$-6\frac{(x_j-y_j)[\delta_{mk}(x_i-y_i)+\delta_{ik}(x_m-y_m)]}{|\mathbf{x}-\mathbf{y}|^5} + 60\frac{(x_i-y_i)(x_j-y_j)(x_k-y_k)(x_m-y_m)}{|\mathbf{x}-\mathbf{y}|^7}, \tag{A.8}$$

and we have set $S(t) = S$ for clarity. The expression $\mathcal{L}(\mathbf{x},\mathbf{y})$ is achieved by differentiating the double-layer integral for the fluid velocity and including the pressure term which may also be written as an integration against $\mathbf{q}(\mathbf{x})$, with $\boldsymbol{\sigma} = -p\mathbf{I} + \mu\left(\nabla\mathbf{u} + \nabla\mathbf{u}^T\right)$ (see Ref. [148]). The stress is determined on the same spatial grid as used to determine the swimming velocity, a uniform discritization in s of the curve $(r(s,t), z(s,t))$ (with polar angle $\phi = 0$). The integration of Eqn (A.7) is performed in local polar coordinates, and the singular contributions are handled analytically as follows. The procedure follows the work of Guiggiani et al. [153].

The integration of Eq. (A.7) is performed on a modified surface $\tilde{S} = s_\epsilon + (S - e_\epsilon)$ and is taken in two parts: the portion of a sphere of radius ϵ centered at the singular point $\mathbf{x}$ which is internal to the body surface (s_ϵ) and intersects the surface S at its boundary, and the body surface punctured by the sphere $(S - e_\epsilon)$. The modified surface limits to the body surface S as $\epsilon \to 0$. For a point $\mathbf{x} \in S$, Eq. (A.7) is written as a small ϵ limit,

$$\frac{1}{\mu}\sigma_{im}(\mathbf{x}) = \lim_{\epsilon\to 0}\left\{\int_{S-e_\epsilon} q_j(\mathbf{y})\mathcal{L}_{ijkm}(\mathbf{x},\mathbf{y})\hat{n}_k(\mathbf{y})\,dS_y + \int_{s_\epsilon} q_j(\mathbf{y})\mathcal{L}_{ijkm}(\mathbf{x},\mathbf{y})\hat{n}_k(\mathbf{y})\,dS_y\right\}. \tag{A.9}$$

Under the assumption that $\mathbf{q}(\mathbf{x})$ is differentiable, with a derivative which is Hölder continuous, we subtract and add the density $\mathbf{q}(\mathbf{x})$ and its gradient at the singular

point in the second integral of Eq. (A.9),

$$\frac{1}{\mu}\sigma_{im}(\mathbf{x}) = \lim_{\epsilon\to 0}\Big\{ \int_{S-e_\epsilon} q_j(\mathbf{y})\mathcal{L}_{ijkm}(\mathbf{x},\mathbf{y})\hat{n}_k(\mathbf{y})\, dS_y \tag{A.10}$$

$$+ \int_{s_\epsilon} \Big(q_j(\mathbf{y}) - q_j(\mathbf{x}) - (x_h - y_h)q_{j,h}(\mathbf{x})\Big)\mathcal{L}_{ijkm}(\mathbf{x},\mathbf{y})\hat{n}_k(\mathbf{y})\, dS_y \tag{A.11}$$

$$+ q_{j,h}(\mathbf{x}) \int_{s_\epsilon} (x_h - y_h)\mathcal{L}_{ijkm}(\mathbf{x},\mathbf{y})\hat{n}_k(\mathbf{y})\, dS_y \tag{A.12}$$

$$+ q_j(\mathbf{x}) \int_{s_\epsilon} \mathcal{L}_{ijkm}(\mathbf{x},\mathbf{y})\hat{n}_k(\mathbf{y})\, dS_y, \Big\} \tag{A.13}$$

where $q_{j,h} = \partial q_j/\partial x_h$. As shown in Ref. [153], the above integration may be reduced to a final formula upon the introduction of a local polar coordinate system (ρ, η) about the target point $\mathbf{x}(s,\phi)$, with

$$\phi' = \phi + \rho\cos(\eta), \quad s' = s + \rho\sin(\eta), \tag{A.14}$$

where $\eta \in [0, 2\pi)$, $\rho \in [0, \bar{\rho}(\eta)]$, and

$$dS_y = J(s')ds'\, d\phi' = J(s'(\rho,\eta))\rho\, d\rho\, d\eta, \tag{A.15}$$

with $J(s') = |\mathbf{x}'_s \times \mathbf{x}_\phi|$ the surface Jacobian. $\rho = \bar{\rho}(\eta)$ is the equation in the local polar coordinate system of the edge of the semi-periodic domain, $(s,\phi) \in ([0, L] \times [0, 2\pi])$. The integration is assisted by the extra factor of ρ in the surface area element, and the final expression for the fluid stress may be reduced to

$$\frac{1}{\mu}\sigma_{im}(\mathbf{x}) = \int_0^{2\pi}\int_0^{\bar{\rho}(\eta)} \Big\{F_{ijk}(\rho,\eta) - \Big[\frac{F_{ijk}^{(-2)}(\eta)}{\rho^2} + \frac{F_{ijk}^{(-1)}(\eta)}{\rho}\Big]\Big\} d\rho\, d\eta \tag{A.16}$$

$$+ \int_0^{2\pi} \Big\{F_{ijk}^{(-1)}(\eta)\ln|\bar{\rho}(\eta)| - F_{ijk}^{(-2)}(\eta)\Big[\frac{1}{\bar{\rho}(\eta)}\Big]\Big\}\, d\eta, \tag{A.17}$$

where $F_{ijk}(\mathbf{x},\mathbf{y}) = q_i(\mathbf{x})\mathcal{L}_{ijk}(\mathbf{x},\mathbf{y})\hat{n}_k(\mathbf{y})$ [153]. The functions $F_{ijk}^{(-1)}(\eta)$ and $F_{ijk}^{(-2)}(\eta)$ are the singular parts of an expansion of $F_{ijk}(\rho,\eta)$ about $\rho = 0$. The integrals above all have finite integrands, and are treated using adaptive quadrature methods.

Convergence tests and comparisons with known exact solutions were used to validate the code. In particular, we have checked to ensure that the surface deformation relation of Samuel & Stone (1996) is satisfied [116, 109]. With the

stress $\boldsymbol{\sigma}$ in hand, the efficiency η_H (Eq. (4.33)) is determined to second-order in the grid-spacing by a simple trapezoidal quadrature. The stress need only be computed for $\phi = 0$ due to axisymmetry.

As a final note, at zero Reynolds number the swimming velocity and efficiency are entirely determined by the surface deformation velocity. Other more general measures of energetic expenditure and total efficiency have been considered for other swimming systems (see Ref. [130]), but in this case the total efficiency will depend significantly upon the means used to produce the vesicle shape-change. In addition, should there be a fluid internal to the vesicle, for example, internal dissipation costs would be relevant in a more general measure of energetic expenditure.

Bibliography

[1] Ho-Young Kim and L. Mahadevan. Capillary rise between elastic sheets. *J. Fluid Mech.*, 548:141–150, 2006.

[2] Jose Bico, Benoit Roman, Loic Moulin, and Arezki Boudaoud. Elastocapillary coalescence in wet hair. *Nature*, 432:690, 2004.

[3] B. Roman and J. Bico. Elasto-capillarity: deforming an elastic structure with a liquid droplet. *J. Phys: Condens. Matter*, 22:493101, December 2010.

[4] Richard R. A. Syms, Eric M. Yeatman, Victor M. Bright, and George M. Whitesides. Surface tension-powered self-assembly of microstructures–the state-of-the-art. *J. Micromech. Systems*, 12:387–417, 2003.

[5] Kenneth K. S. Lau, Jose Bico, Kenneth B. K. Teo, Manish Chhowalla, Gehan A.J. Amaratunga, William I. Milne, Gareth H. McKinley, and Karen K. Gleason. Superhydrophobic carbon nanotube forests. *Nano Lett.*, 3:1701–1705, 2003.

[6] K Autumn, YA Liang, ST Hsieh, W Zesch, WP Chan, TW Kenny, R Fearing, and RJ Full. Adhesive force of a single gecko foot-hair. *Nature*, 405:681–685, 2000.

[7] K Autumn, M Sitti, YCA Liang, AM Peattie, WR Hansen, S Sponberg, TW Kenny, R Fearing, JN Israelachvili, and RJ Full. Evidence for van der waals adhesion in gecko setae. *Proc. Natl. Acad. Sci. U. S. A.*, 99:12252–12256, 2002.

[8] H. Berg. *Random walks in biology.* Princeton University Press, 1993.

[9] D. Bray. *Cell Movements.* Garland Publishing, New York, NY, 2000.

[10] Eric Lauga and TR Powers. The hydrodynamics of swimming microorganisms. *Rep. Prog. Phys.*, 72:096601, 2009.

[11] D. Saintillan and M.J. Shelley. Instabilities, pattern formation, and mixing in active suspensions. *Phys. Fluids*, 20(12):123304 (16 pp.), 2008.

[12] R Voituriez, J. F Joanny, and J Prost. Generic phase diagram of active polar films. *Phys. Rev. Lett.*, 96(2):1–4, Jan 2006.

[13] F Jülicher, K Kruse, J Prost, and JF Joanny. Active behavior of the cytoskeleton. *Physics Reports*, 449(1-3):3–28, 2007.

[14] MC Cross and PC Hohenberg. Pattern formation outside of equilibrium. *Rev. Mod. Phys.*, 65(3):851–1112, 1993.

[15] Jian-Lin Liu, Xi-Qiao Feng, Re Xia, and Hong-Ping Zhao. Hierarchical capillary adhesion of microcantilevers or hairs. *J. Phys. D: Appl. Phys.*, 40:5564–5570, 2007.

[16] Bharat Bhushan. Nanotribology of carbon nanotubes. *J. Phys.: Condens. Matter*, 20:365214, 2008.

[17] Nicola M. Pugno, Pietro Cornetti, and ALberto Carpinteri. On the impossibility of separating nanotubes in a bundle by longitudinal tension. *J. Adhes.*, 84:439–444, 2008.

[18] D. Langbein. Van der waals attraction between cylinders, rods or fibers. *Phys. kondens. Materie*, 15:61–86, 1972.

[19] Jacob Israelachvili. *Intermolecular and Surface Forces*. Academic, New York, 1992.

[20] B. Chen, P.D. Wu, and H. Gao. Hierarchical modelling of attachment and detachment mechanisms of gecko toe adhesion. *Proc. Roy. Soc. A*, 464:1639–1652, 2008.

[21] Liehui Ge, Sunny Sethi, Lijie Ci, Pulickel M. Ajayan, and Ali Dhinojwala. Carbon nanotube-based synthetic gecko tapes. *Proc. Natl. Acad. Sci. U.S.A*, 104:10792–10795, 2007.

[22] HJ Gao, X Wang, HM Yao, S Gorb, and E Arzt. Mechanics of hierarchical adhesion structures of geckos. *Mech. Mater.*, 37:275–285, 2005.

[23] A.E. Allahverdyan, Zh. S. Gevorkian, Chin-Kun Hun, and Th. M. Nieuwenhuizen. Adhesion-induced dna naturation. *Phys. Rev. Lett.*, 96:098302, 2006.

[24] K. Hatch, C. Danilowicz, V. Coljee, and M. Prentiss. Measurements of the hysteresis in unzipping and rezipping double-stranded dna. *Phys. Rev. E*, 75:051908, 2007.

[25] J. Kierfeld. Force-induced desorption and unzipping of semiflexible polymers. *Phys. Rev. Lett.*, 97:058302, 2006.

[26] A.R. Bausch and K. Kroy. A bottom-up approach to cell mechanics. *Nature Phys.*, 2:231–238, 2006.

[27] Xabier Oyharcabal and Thomas Frisch. Peeling off an elastica from a smooth attracting substrate. *Phys. Rev. E*, 71:036611, 2005.

[28] Gen-Wei Wang, Yin Zhang, Ya-Pu Zhao, and Gui-Tong Yang. Pull-in instability of carbon nanotube tweezers under the influence of van der waals forces. *J. Micromech. Microeng.*, 14:1119–1125, 2004.

[29] M. C. Strus, L. Zalamea, A. Raman, R.B. Pipes, C.V. Nguyen, and E.A. Stach. Peeling force spectroscopy: Exposing the adhesive nanomechanics of one-dimensional nanostructures. *Nano Lett.*, 8:544–550, 2008.

[30] Li-Qun Chen, Hao Chen, and Jean W. Zu. Equilibrium and bifurcation of varying cross-section microcantilevers subject to the atomic force. *Chaos, Solitons and Fractals*, 28:1159–1164, 2006.

[31] Krzysztof Baczynski, Reinhard Lipowsky, and Jan Kierfeld. Stretching of buckled filaments by thermal fluctuations. *Phys. Rev. E*, 76:061914, 2007.

[32] Mehran Kardar. *Statistical Physics of Fields*. Cambridge University Press, 2007.

[33] Steven H. Strogatz. *Nonlinear Dynamics and Chaos*. Perseus Books Publishing, 1994.

[34] HC Berg. Motile behavior of bacteria. *Physics Today*, 53(1):24–29, 2000.

[35] H. C. Berg. *E. coli in Motion*. Springer-Verlag, New York, NY, 2004.

[36] C Brennen and H Winet. Fluid mechanics of propulsion by cilia and flagella. *Annu. Rev. Fluid Mech.*, 9(1):339–398, 1977.

[37] P. D. Frymier, R. M. Ford, H. C. Berg, and P. T. Cummings. Three-dimensional tracking of motile bacteria near a solid planar surface. *Proc. Natl. Acad. Sci. USA*, 92:6195–6199, 1995.

[38] P. D. Frymier and R. M. Ford. Analysis of bacterial swimming speed approaching a solid-liquid interface. *AIChE J.*, 43:1341–1347, 1997.

[39] Eric Lauga, WR DiLuzio, GM Whitesides, and HA Stone. Swimming in circles: Motion of bacteria near solid boundaries. *Biophys. J.*, 90(2):400–412, 2006.

[40] L. Rothschild. Non-random distribution of bull spermatozoa in a drop of sperm suspension. *Nature*, 198:1221–1222, 1963.

[41] H. Winet, G. S. Bernstein, and J. Head. Observations on the response of human spermatozoa to gravity, boundaries and fluid shear. *J. Reprod. Fert.*, 70:511–523, 1984.

[42] L. J. Fauci and A. Mcdonald. Sperm motility in the presence of boundaries. *Bull. Math. Biol.*, 57:679–699, 1995.

[43] J. Cosson, P. Huitorel, and C. Gagnon. How spermatozoa come to be confined to surfaces. *Cell Motil. Cytoskel.*, 54:56–63, 2003.

[44] D. M. Woolley. Motility of spermatozoa at surfaces. *Reproduction*, 126:259–270, 2003.

[45] A. P. Berke, L. Turner, H. C. Berg, and E. Lauga. Hydrodynamic attraction of swimming microorganisms by surfaces. *Phys. Rev. Lett.*, 101:038102, 2008.

[46] J. R. Blake and M. A. Sleigh. Mechanics of ciliary locomotion. *Biol. Rev. Camb. Phil. Soc.*, 49:85–125, 1974.

[47] S. Childress. *Mechanics of Swimming and Flying*. Cambridge University Press, Cambridge U.K., 1981.

[48] M. A. Sleigh, J. R. Blake, and N. Liron. The propulsion of mucus by cilia. *Am. Rev. Resp. Dis.*, 137:726–741, 1988.

[49] M. Salathe. Regulation of mammalian ciliary beating. *Annu. Rev. Physiol.*, 69:401–422, 2007.

[50] L. J. Fauci and R. Dillon. Biofluidmechanics of reproduction. *Annu. Rev. Fluid Mech.*, 38:371–394, 2006.

[51] A. J. Reynolds. The swimming of minute organisms. *J. Fluid Mech.*, 23:241–260, 1965.

[52] D. F. Katz. Propulsion of microorganisms near solid boundaries. *J. Fluid Mech.*, 64:33–49, 1974.

[53] D. F. Katz, J. R. Blake, and S. L. Paverifontana. Movement of slender bodies near plane boundaries at low Reynolds number. *J. Fluid Mech.*, 72:529–540, 1975.

[54] D.F. Katz and J.R. Blake. Flagellar motions near walls. In T.Y. Wu, C.J. Brokaw, and C Brennen, editors, *Swimming and Flying in Nature*, volume 1, pages 173–184. Plenum, New-York, 1975.

[55] E. Lauga, L. Shi, J. M. Nascimento, T. Chen, and M. Berns. Solid boundaries decrease the propulsive force of swimming spermatozoa. *submitted*, 2010.

[56] CH Wiggins and RE Goldstein. Flexive and propulsive dynamics of elastica at low reynolds number. *Phys. Rev. Lett.*, 80(17):3879–3882, 1998.

[57] CH Wiggins, D Riveline, A Ott, and RE Goldstein. Trapping and wiggling: Elastohydrodynamics of driven microfilaments. *Biophys. J.*, 74(2):1043–1060, 1998.

[58] RE Goldstein and SA Langer. Nonlinear dynamics of stiff polymers. *Phys. Rev. Lett.*, 75(6):1094–1097, 1995.

[59] E. Lauga. Floppy swimming: Viscous locomotion of actuated elastica. *Phys. Rev. E*, 75:041916, 2007.

[60] T. S. Yu, E. Lauga, and A. E. Hosoi. Experimental investigations of elastic tail propulsion at low Reynolds number. *Phys. Fluids*, 18:091701, 2006.

[61] J Gray and GJ Hancock. The propulsion of sea-urchin spermatozoa. *J. Exp. Biol.*, 32(4):802–814, 1955.

[62] HC Fu, CW Wolgemuth, and TR Powers. Beating patterns of filaments in viscoelastic fluids. *Phys. Rev. E*, 78(4), 2008.

[63] S Camalet and F Jülicher. Generic aspects of axonemal beating. *New J. Phys*, 2(1), 2000.

[64] C. J. Brokaw. Bend propagation by a sliding filament model for flagella. *J. Exp. Biol.*, 55:289–304, 1971.

[65] C. J. Brokaw. Non-sinusoidal bending waves of sperm flagella. *J. Exp. Biol.*, 55:155–169, 1965.

[66] RG Cox. The motion of long slender bodies in a viscous fluid part 1. general theory. *J. Fluid Mech.*, 44(04):791–810, 2006.

[67] Ingmar H Riedel-Kruse, Andreas Hilfinger, Jonathon Howard, and Frank Jülicher. How molecular motors shape the flagellar beat. *HFSP J.*, 1(3):192, Jan 2007.

[68] Andreas Hilfinger, Amit K Chattopadhyay, and Frank Jülicher. Nonlinear dynamics of cilia and flagella. *Phys. Rev. E*, 79(5):1–8, May 2009.

[69] L. D. Landau and E. M. Lifshitz. *Theory of elasticity.* Pergamon Press, Oxford, 3rd edition, 1986.

[70] John F. Stalnaker and R.G. Hussey. Wall effects on cylinder drag at low reynolds number. *Phys. Fluids*, 22:040603, 1979.

[71] S. Ishijima, S. Oshio, and H. Mohri. Flagellar movement of human spermatozoa. *Gamete Res.*, 13:185–197, 1986.

[72] EM Purcell. Life at low reynolds number. *Am. J. Phys*, 45(3):11, 1977.

[73] S. Childress and R. Dudley. Transition from ciliary to flapping mode in a swimming mollusc: flapping flight as a bifurcation in re_ω. *J. Fluid Mech.*, 498:257–288, 2004.

[74] E Lauga. Continuous breakdown of Purcell's scallop theorem with inertia. *Phys. Fluids*, 19(6):061703, 2007.

[75] U Seifert. Configurations of fluid membranes and vesicles. *Advances in Physics*, 46(1):13–137, 1997.

[76] J Käs and E Sackmann. Shape transitions and shape stability of giant phospholipid vesicles in pure water induced .... *Biophys J*, 60:825–844, 1991.

[77] M Antonietti and S Förster. Vesicles and liposomes: A self-assembly principle beyond lipids we cordially thank all our .... *Adv. Mater.*, 15:1323–1333, 2003.

[78] M Li and P Keller. Stimuli-responsive polymer vesicles. *Soft Matter*, 5:927–937, 2009.

[79] H Kukula, H Schlaad, M Antonietti, and S Forster. The formation of polymer vesicles or "peptosomes" by polybutadiene-block-poly (l-glutamate .... *J. Am. Chem. Soc*, 124:1658–1663, 2002.

[80] J Yang, R Pinol, F Gubellini, and D Levy. Formation of polymer vesicles by liquid crystal amphiphilic block copolymers. *Langmuir*, 22:7907–7911, 2006.

[81] R Lipowsky. Bending of membranes by anchored polymers. *Europhys. Lett.*, 30:197–202, 1995.

[82] J Wang, K Guo, F Qiu, H Zhang, and Y Yang. Predicting shapes of polymer-chain-anchored fluid vesicles. *Phys. Rev. E*, 71:041908, 2005.

[83] K Guo, J Wang, F Qiu, H Zhang, and Y Yang. Shapes of fluid vesicles anchored by polymer chains. *Soft Matter*, 5:1646–1655, 2009.

[84] M Breidenich, R Netz, and R Lipowsky. The influence of non-anchored polymers on the curvature of vesiclesô. *Molecular Physics*, 103:3169–3183, 2005.

[85] Filipe E Antunes, Eduardo F Marques, Maria G Miguel, and Björn Lindman. Polymer–vesicle association. *Advances in Colloid and Interface Science*, 147-148(C):18–35, 2009.

[86] HG Dobereiner. *The budding transition of phospholipid vesicles: a quantitative study via phase contrast microscopy.* PhD thesis, Simon Fraser University, 1995.

[87] PG Petrov, JB Lee, and HG Dobereiner. Coupling chemical reactions to membrane curvature: A photochemical morphology switch. *Europhys. Lett.*, 48(4):435–441, 1999.

[88] HT McMahon and JL Gallop. Membrane curvature and mechanisms of dynamic cell membrane remodelling. *Nature*, 438:590–596, 2005.

[89] A Veksler and NS Gov. Phase transitions of the coupled membrane-cytoskeleton modify cellular shape. *Biophys. J*, 93(11):3798–3810, 2007.

[90] KC Huang, R Mukhopadhyay, and NS Wingreen. A curvature-mediated mechanism for localization of lipids to bacterial poles. *PLoS Comput Biol*, 2(11):e151, 2006.

[91] H Grimm, A Verkhovsky, and A Mogilner. Analysis of actin dynamics at the leading edge of crawling cells: implications for the shape .... *Eur Biophys J*, 32:563–577, 2003.

[92] D Bottino, A Mogilner, T Roberts, and M Stewart. How nematode sperm crawl. *J Cell Sci*, 115:367–384, 2002.

[93] R. Dreyfus, J. Baudry, M. L. Roper, M. Fermigier, H. A. Stone, and J. Bibette. Microscopic artificial swimmers. *Nature*, 437:862–865, 2005.

[94] L. E. Becker, S. A. Koehler, and H. A. Stone. On self-propulsion of micromachines at low Reynolds number: Purcell's three-link swimmer. *J. Fluid Mech.*, 490:15–35, 2003.

[95] A. Najafi and R. Golestanian. Simple swimmer at low Reynolds number: Three linked spheres. *Phys. Rev. E*, 69:062901, 2004.

[96] I. M. Kulic, R. Thaokar, and H. Schiessel. Twirling DNA rings- Swimming nanomotors ready for a kickstart. *Europhys. Lett.*, 72(4):527–533, 2005.

[97] A.M. Leshansky, O. Kenneth, O. Gat, and J.E. Avron. A frictionless microswimmer. *New J. Phys.*, 9(5):145, 2007.

[98] M. Leoni, J. Kotar, B. Bassetti, P. Cicuta, and M. Cosentino Lagomarsino. A basic swimmer at low reynolds number. *Soft Matter*, 5:472 – 476, 2009.

[99] A. M. Leshansky and O. Kenneth. Surface tank treading: Propulsion of purcell's toroidal swimmer. *Phys. Fluids*, 20:063104, 2008.

[100] S. E. Spagnolie. Rehinging biflagellar locomotion in a viscous fluid. *Phys. Rev. E*, 80:046323, 2009.

[101] J. R. Howse, R. A. L. Jones, A. J. Ryan, T. Gough, R. Vafabakhsh, and R. Golestanian. Self-motile colloidal particles: From directed propulsion to random walk. *Phys. Rev. Lett.*, 99(4):048102, 2007.

[102] R. Golestanian, T. B. Liverpool, and A. Ajdari. Designing phoretic micro- and nano-swimmers. *New J. Phys.*, 9, 2007.

[103] Sriram Ramaswamy. The mechanics and statistics of active matter. *Ann Rev Cond Matt Phys*, 1(1):323–345, 2010.

[104] G. Karp. *Cell and Molecular Biology.* John Wiley and Sons, Inc., 1999.

[105] F Brochard and JF Lennon. Frequency spectrum of the flicker phenomenon in erythrocytes. *J. Phys.*, 36:1035–1047, 1975.

[106] J.-B. Manneville, P. Bassereau, S. Ramaswamy, and J. Prost. Active membrane fluctuations studied by micropipet aspiration. *Phys. Rev. E*, 64(2):021908, Jul 2001.

[107] G Taylor. Analysis of the swimming of microscopic organisms. *Proceedings of the Royal Society of London. Series A, Mathematical and Physical Sciences (1934-1990)*, 209(1099):447–461, 1951.

[108] E. Lauga. Propulsion in a viscoelastic fluid. *Phys Fluids*, 19(8):083104–+, August 2007.

[109] H.A. Stone and A.D.T. Samuel. Propulsion of microorganisms by surface distortions. *Phys. Rev. Lett.*, 77:4102, 1996.

[110] A.A. Evans, SE Spagnolie, and E Lauga. Stokesian jellyfish: viscous locomotion of bilayer vesicles. *Soft Matter*, 6:1737–1747, 2010.

[111] W Helfrich. Elastic properties of lipid bilayers: theory and possible experiments. *Z. Naturforsch.*, 28:693–703, 1973.

[112] TR Powers. Dynamics of filaments and membranes in a viscous fluid. *Rev. Mod. Phys.*, 82:1607–1631, 2010.

[113] Ling Miao, Udo Seifert, Michael Wortis, and Hans-Günther Döbereiner. Budding transitions of fluid-bilayer vesicles: The effect of area-difference elasticity. *Phys. Rev. E*, 49(6):5389–5407, Jun 1994.

[114] Martin Michael Müller, Markus Deserno, and Jemal Guven. Interface-mediated interactions between particles: A geometrical approach. *Phys. Rev. E*, 72(6):061407, Dec 2005.

[115] S Ramaswamy, J Toner, and J Prost. Nonequilibrium fluctuations, traveling waves, and instabilities in active membranes. *Phys. Rev. Lett.*, 84(15):3494–3497, 2000.

[116] J. Happel and H. Brenner. *Low Reynolds Number Hydrodynamics*. Prentice-Hall, 1965.

[117] R Reigada, J Buceta, and K Lindenberg. Generation of dynamic structures in nonequilibrium reactive bilayers. *Phys. Rev. E*, 72:051921, 2005.

[118] Joshua Zimmerberg and Michael M. Kozlov. How proteins produce cellular membrane curvature. *Nat. Rev. Mol. Cell Bio.*, 7:9–19, 2006.

[119] Jeffrey T. Finer, Robert M. Simmons, and James A. Spudich. Single myosin molecule mechanics: piconewton forces and nanometre steps. *Nature*, 368:113–119, 1994.

[120] Fangqiang Zhu, Emad Tajkhorshid, and Klaus Schulten. Theory and simulation of water permeation in aquaporin-1. *Biophys. J.*, 86(1):50 – 57, 2004.

[121] I. S. Davis, B. Shachar-Hill, M. R. Curry, K. S. Kim, T. J. Pedley, and A. E. Hill. Osmosis in semi-permeable pores: An examination of the basic flow equations based on an experimental and molecular dynamics study. *Proc. Roy. Soc. A*, 463(2079):pp. 881–896, 2007.

[122] Takaaki Miura, Hideaki Oosawa, Makoto Sakai, Yukitoshi Syundou, Takahiko Ban, and Akihisa Shioi. Autonomous motion of vesicle via ion exchange. *Langmuir*, 26(3):1610–1618, 2010.

[123] R Lipowsky. *Statistical Mechanics of Biocomplexity*. Springer Berlin/Heidelberg, 1999.

[124] F Brochard and J Lennon. Frequency spectrum of the flicker phenomenon in erythrocytes. *J. Phys. France*, 36:1035–1047, 1975.

[125] S Yu, T Azzam, I Rouiller, and A Eisenberg. "breathing" vesicles. *J. Am. Chem. Soc.*, 131:10557–10556, 2009.

[126] V Nikolov, R Lipowsky, and R Dimova. Behavior of giant vesicles with anchored dna molecules. *Biophys. J*, 92(12):4356–4368, 2007.

[127] F Campelo and A Hernandez-Machado. Shape instabilities in vesicles: A phase-field model. *Eur Phys J*, 143(1):101–108, 2007.

[128] U Seifert, K Berndl, and R Lipowsky. Shape transformations of vesicles: Phase diagram for spontaneous- curvature and bilayer-coupling models. *Phys. Rev. A*, 44(2):1182–1202, 1991.

[129] H Jiang, G Huber, RA Pelcovits, and TR Powers. Vesicle shape, molecular tilt, and the suppression of necks. *Phys. Rev. E*, 76(3), 2007.

[130] S. E. Spagnolie and E. Lauga. The optimal elastic flagellum. *Phys. Fluids (to appear)* , 2010.

[131] Knut Drescher, Raymond E. Goldstein, Nicolas Michel, Marco Polin, and Idan Tuval. Direct measurement of the flow field around swimming microorganisms. *Phys. Rev. Lett.*, 105(16):168101, Oct 2010.

[132] Luis Cisneros, Ricardo Cortez, Christopher Dombrowski, Raymond Goldstein, and John Kessler. Fluid dynamics of self-propelled microorganisms, from individuals to concentrated populations. *Experiments in Fluids*, 43:737–753, 2007.

[133] Ingmar H. Riedel, Karsten Kruse, and Jonathon Howard. A Self-Organized Vortex Array of Hydrodynamically Entrained Sperm Cells. *Science*, 309(5732):300–303, 2005.

[134] Ganesh Subramanian and Donald L. Koch. Critical bacterial concentration for the onset of collective swimming. *Journal of Fluid Mechanics*, 632(-1):359–400, 2009.

[135] Christel Hohenegger and Michael J. Shelley. Stability of active suspensions. *Phys. Rev. E*, 81(4):046311, Apr 2010.

[136] A Baskaran and MC Marchetti. Statistical mechanics and hydrodynamics of bacterial suspensions. *PNAS*, 106:15567–15572, 2009.

[137] John Toner and Yuhai Tu. Flocks, herds, and schools: A quantitative theory of flocking. *Phys. Rev. E*, 58(4):4828–4858, Oct 1998.

[138] S. Mishra, A. Baskaran, and M. C. Marchetti. Fluctuations and pattern formation in self-propelled particles. *Phys Rev E*, pages 061916–+.

[139] Takuji Ishikawa, M. P. Simmonds, and T. J. Pedley. Hydrodynamic interaction of two swimming model micro-organisms. *Journal of Fluid Mechanics*, 568(-1):119–160, 2006.

[140] M. J. Lighthill. On the squirming motion of nearly spherical deformable bodies through liquids at very small Reynolds numbers. *Commun. Pure Appl. Math.*, 5:109–118, 1952.

[141] J. R. Blake. A spherical envelope approach to ciliary propulsion. *J. Fluid Mech.*, 46:199–208, 1971.

[142] Ingo O. Götze and Gerhard Gompper. Mesoscale simulations of hydrodynamic squirmer interactions. *Phys Rev E*, 82(4):041921, 2010.

[143] Takuji Ishikawa, J. T. Locsei, and T. J. Pedley. Development of coherent structures in concentrated suspensions of swimming model micro-organisms. *Journal of Fluid Mechanics*, 615:401–431, 2008.

[144] Takuji Ishikawa and Masateru Hota. Interaction of two swimming paramecia. *J Exp Biol*, 209(22):4452–4463, 2006.

[145] P. N. Pusey and W. van Megen. Observation of a glass transition in suspensions of spherical colloidal particles. *Phys. Rev. Lett.*, 59(18):2083–2086, Nov 1987.

[146] W.B. Russel, D. A. Saville, and W. R. Schowalter. *Colloidal Dispersions*. Cambridge University Press, 1989.

[147] Valerie J. Anderson and Henk N. W. Lekkerkerker. Insights into phase transition kinetics from colloid science. *Nature*, 416(5453):811–815, 2002.

[148] C. Pozrikidis. *Boundary Integral and Singularity Methods*. Cambridge University Press, 1992.

[149] H. Power G. Miranda. Second kind integral equation formulation of stokes flows past a particle of arbitrary shape. *Singular Integrals in B.E. Methods, SIAM*, 47(4):689–698, 1987.

[150] Y. Saad and M. H. Schultz. GMRES: a generalized minimal residual algorithm for solving nonsymmetric linear systems. *SIAM J. Sci. Stat. Comp.*, 7:859–869, 1986.

[151] G. B. Jeffery. The motion of ellipsoidal particles immersed in a viscous fluid. *Proc. Roy. Soc. Lond. A*, 102:161–179, 1922.

[152] A. J. Goldman, R. G. Cox, and H. Brenner. The slow motion of two identical arbitrarily oriented spheres through a viscous fluid. *Chem. Eng. Sci.*, 21:1151–1170, 1966.

[153] M. Guiggiani. Formulation and numerical treatment of boundary integral equations with hypersingular kernels. *in: Singular Integrals in B. E. Methods, V. Sladek and J. Sladek (eds.)*, 1998.